Image processing & remote sensing: analyzing sequences of low and very high spatial resolution

Thomas Corpetti

HABILITATION À DIRIGER DES RECHERCHES

présentée devant

l'Université de RENNES 1
Mention : Traitement du Signal et Télécommunications

par
Thomas Corpetti

Image processing & remote sensing : analyzing sequences of low and very high spatial resolution

Soutenue le 20 juin 2011 à Telecom Paris Tech

Devant le jury composé de :

Patrick Bouthemy	-	Dir. de Recherche INRIA, Rennes (France)	
Lorenzo Bruzzone	-	Prof. RS Lab, Trento (Italie)	Rapporteur
Jocelyn Chanussot	-	Prof. GIPSA Lab, Grenoble (France)	Président du jury
Laurence Hubert-Moy	-	Prof. COSTEL/OSUR, Rennes (France)	
Henri Maitre	-	Prof., Telecom Paris Tech (France)	Rapporteur
Etienne Mémin	-	Dir. de Recherche INRIA, Rennes (France)	
Olivier Talagrand	-	Dir. de Recherche CNRS, LMD Paris (France)	Rapporteur

Remerciements

Il n'est pas facile d'écrire une page de remerciements tant les personnes rencontrées au cours de ces dix dernières années sont nombreuses et m'ont toutes apporté une aide ou un soutien précieux. Il est encore plus difficile d'organiser ces remerciements.

D'avance je préviens donc que l'ordre d'apparition n'est pas signe d'importance et je m'excuse pour celles ou ceux que j'aurais oubliés.

Je remercie les membres du jury pour avoir dégagé du temps (et ça n'est pas facile) afin de s'intéresser à mes travaux et pour certains, de les rapporter.

- Merci à Jocelyn Chanussot pour avoir accepté de présider ce jury et pour toutes ses remarques/conseils/commentaires qui m'ont été utiles ;
- Merci à Henri Maître pour avoir rapporté ce travail et pour le grand intérêt qu'il porte à ces recherches depuis de nombreuses années ;
- Merci à Olivier Talagrand pour avoir apporté son regard de physicien et de spécialiste d'assimilation de données à ce travail ;
- Un grazie speciale a Lorenzo Bruzzone per avermi rapporto nella redazione di questa tesi e per esser venuto da Trento ad onorarmi della sua presenza alla discussione della tesi ;
- Merci à Patrick Bouthemy pour son rôle dans le jury et plus globalement pour toutes les relations que l'on entretient depuis 10 ans. Merci de m'avoir toujours ouvert la porte et de m'avoir accepté à nouveau dans VISTA puis à l'INRIA entre 2007 et 2009. Cela m'a infiniment aidé ;
- Merci à Laurence Hubert-Moy pour les collaborations que nous entretenons depuis 2004 et pour ses nombreux encouragements à ne pas baisser les bras lorsque je me sentais un peu trop noyé dans la géographie ;
- Merci enfin à Etienne Mémin avec qui je travaille avec plaisir depuis plus de 10 ans. Travailler avec Etienne c'est s'assurer d'aborder des thèmes passionnants, ambitieux dans un contexte scientifique de qualité !

Merci aussi à Telecom ParisTech d'avoir accueilli la soutenance.

Je remercie plus globalement les personnes rencontrées au Cemagref de Rennes (en particulier Dominique Heitz, Johan Carlier et Georges Arroyo), à COSTEL (entre autres, merci à Jean-Pierre Marchand, Vincent Dubreuil ainsi que Hervé, Olivier, Samuel, et tous les autres) et à l'INRIA (Patrick Pérez, Charles Kervrann, Pierre Hellier, Ivan Laptev, Thierry, Sophie, ...) pour tous les bons moments, scientifiques et personnels, passés ensemble.

Un très grand merci aux étudiants que j'ai encadrés et qui ont une participation évidente aux travaux présentés dans ce document. En particulier, merci à :

- Antoine Lefebvre que j'ai eu le plaisir d'encadrer avec Laurence Hubert-Moy pendant sa thèse (soutenue en avril 2011) sur l'analyse d'images agricoles (deuxième partie de ce document) ;
- Pierre Allain, encadré avec Nicolas Courty, sur l'analyse de mouvements de foules. Merci aussi d'avoir fait l'effort de passer quelques mois à Pékin, je sais que c'était beaucoup te demander !
- Claire Thomas qui a travaillé en post-doctorat sur le suivi de cellules convectives ;
- Les étudiants de MASTER Gong Xing et Pascal Zille ayant travaillé sur la détection de changements et la multi-résolution.

Merci également à tous mes collaborateurs, en particulier Nicolas Papadakis, Ronan Fablet, Sileye Ba, Cyril Cassisa, Bertrand Chapron, Shao Liang, Guixiang Cui, Zhaoshun Zhang, Jiang Zhu, ...

Mention spéciale à Nicolas Courty qui, au delà des collaborations que nous avons, est également un ami avec qui je travaille avec grand plaisir ! Mention particulière également à

Patrick Héas pour tous les excellents moments passés ensemble, que ce soit dans le bureau, en conférence ou en famille.

Depuis 2009 je suis détaché en Chine au LIAMA et cette expérience est extraordinaire. Je suis très reconnaissant au CNRS de nous donner l'opportunité de réaliser de tels projets et je remercie toutes les personnes ayant joué un rôle dans ce détachement (Véronique Prinet, Véronique Donzeau-Gouge, Stéphane Grumbach, Philippe Baptiste, Michel Bidoit, Jean-Claude Thivolle, Jean-Pierre Jouannaud, Diane Brami, Laurence Hubert-Moy, Marc Robin, Franck Davoine).

Merci enfin à ma famille, mon épouse Catherine et mes 3 enfants Lucien, Rozenn et Antonina, pour tout ce qu'on vit ensemble depuis toutes ces années et aussi pour avoir accepté de vivre l'inconnu en s'exilant en Chine. Merci Catherine pour tout. Merci enfin à Paul Sablonnière pour avoir apporté son aide lors de la préparation de la soutenance et d'avoir rempli la salle lors de celle-ci.

Enfin, ci joint une liste, probablement non exhaustive, de toutes celles et tous ceux que j'aimerais remercier.

谢谢

Many Thanks	**Merci beaucoup**
Pierre Allain	Georges Arroyo
Sileye Ba	Adrien Bartoli
Sophie Blestel	Patrick Bouthemy
Cyril Cassisa	Bertrand Chapron
Samuel Corgne	Nicolas Courty
Guixiang Cui	Philippe De Reffye
Vincent Dubreuil	Nadia Dupont
Pauline Dusseux	Ronan Fablet
Stéphane Grumbach	Xing Gong
Patrick Héas	Dominique Heitz
Pierre Hellier	Bizhen Hong
Laurence Hubert-Moy	Stéphanie Jehan-Besson
Jean Pierre Jouannaud	Meng Zhen Kang
Charles Kervrann	Ivan Laptev
Rémi Lecerf	Antoine Lefebvre
Dongmin Ma	Jean-Pierre Marchand
Paul Marcombes	Etienne Mémin
Grégoire Mercier	Kristel Michel
Nicolas Papadakis	Thierry Pecot
Patrick Pérez	Olivier Planchon
Véronique Prinet	Hervé Quénol
Laurent Sarry	Liang Shao
Jean-Claude Thivolle	Christophe Tilmant
Claire Thomas	Zhaoshun Zhang
Jiang Zhu	Pascal Zille
...	...

Table des matières

General Introduction

General introduction

This habilitation thesis is devoted to the analysis of time series of remote sensing data. We in particular focus on two kind of imagery :

1. Low Spatial Resolution (LSR) remote sensing images ;
2. Very High Spatial Resolution (VHRS) remote sensing images.

Roughly, the associated spatial resolutions of these data are $\sim 3-5km$ for LSR and $< 2m$ for VHSR. Due to current physical limitations related to the behavior of satellites, the rate of acquisition of such images is inversely proportional to their spatial resolution. Therefore with LSR images, the cadence is very high (for instance one image every $15min$ with MSG –Meteosat Second Generation) and enables an analysis of the turbulent atmospheric flows observed through the motion of the clouds, the oceanic circulation, ... On the other hand, with VHSR images, the time between two data can be from several weeks to several months. The related studies are rather concerned with the definition of advanced change detection techniques to highlight the main structural changes between images. Some illustrations of such data are visible in the top of figure Fig. 1.

Applications are numerous. Many domains related to geosciences exploit remote sensing images in reason of the huge amount of spatial (and sometimes temporal) data that can considerably supplement the local probes. Remote sensing from satellites give invaluable information and knowledge on many topics related to environment as for instance :

- dynamics of the atmosphere ;
- dynamics of the ocean ;
- dynamics of landscapes ;
- analysis of soils ;
- ...

Informations that have to be extracted are related to the detection and tracking of extreme events such as storms or cyclones, the monitoring of the evolution of river plumes, the tracking of pollutants, the estimation of motions in ocean or atmosphere, the identification of changed areas from data acquired several years apart, the identification of agricultural parcels, of green areas in cities, ... The last decades remote sensing reached the operational level and led to the development of operational services for atmosphere monitoring (storing, managing and distributing multimodal satellite observation data) or agriculture management (identification of wetlands, of bare soils, of carbon, ...).

The potential of information extraction from remote sensing is however widely unexploited since the analysis of such data remain a difficult task for several reasons. Let us in particular note that :

- the complexity of the structures that appear in LSR data (deformable clouds submitted to sudden winds partially described by non linear equations of turbulence) and
- the complexity of the structures involved in VHSR data (high internal variability inside an object)

yield their recognition from images very difficult. This study is a contribution in the design of tools for manipulating such data.

Although the information embedded in LSR and VHSR images are related to different topics (atmosphere/ocean on the one hand, agriculture or urban monitoring on the other hand), most of the applications of these researches were connected to the COSTEL group (Climate and Land Cover with Remote Sensing) where the long term objectives concern

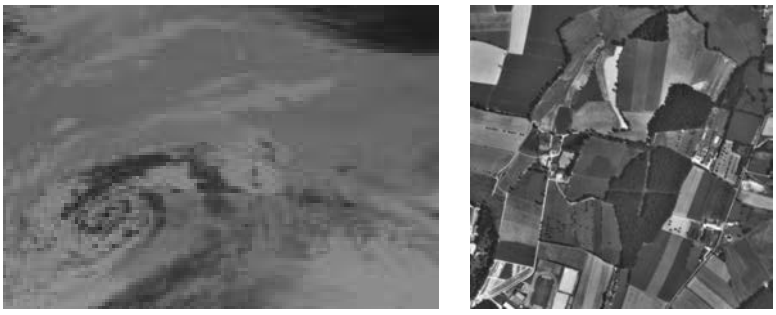

LSR data VHSR Data

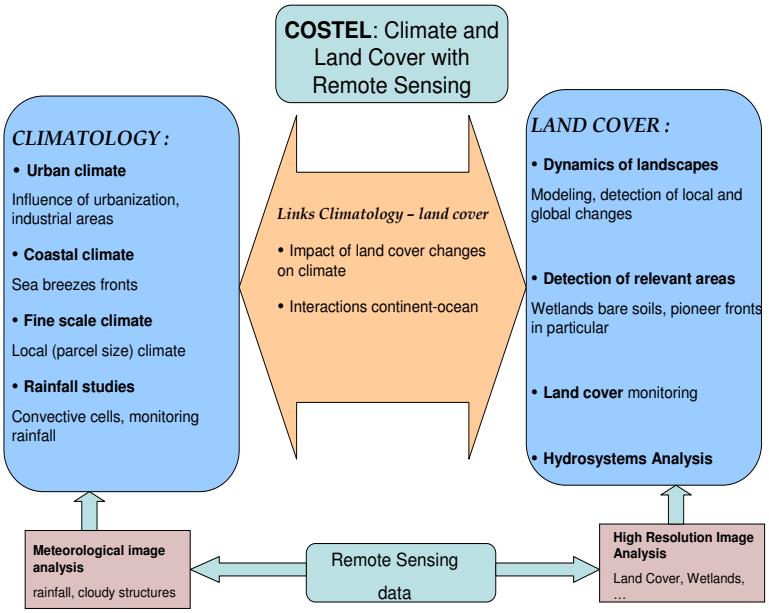

FIGURE 1 – **Examples of processed images and organization of the COSTEL group**

the analysis of relationships between climate and land cover using remote sensing data. Therefore outputs of the methods that are presented in this document provide a contribution in that direction. The organization of the COSTEL group is schematized in the second part of figure Fig. 1.

This document is structured into two parts related to the analysis of LSR and VHSR data respectively. In the first part, the challenges concern the design of tools for analyzing turbulent motions and structures from images. It is composed of 3 chapters :

- The **chapter 1** is concerned with the **motion estimation** problem from a **pair of images**. It presents the general context of motion estimation and proposes some techniques especially designed for fluid flows ;
- The **chapter 2** is concerned with the **motion estimation** problem from a **sequence of images**. In that context, the integration and the manipulation of dynamical laws coming from fluid mechanics is exploited. We have in particular worked on the variational assimilation framework to design efficient tools ;
- The **chapter 3** presents **other applications of data assimilation** for various computer vision problems (segmentation, data reconstruction, multi-resolution and also crowd analysis).

As for the second part, the topics refer to the analysis of objects observed in VHSR data and to the change detection problem. It is also composed of 3 chapters :

- The **chapter 4** presents a way to deal with the textured objects observed in VHSR data. We present **original descriptors** based on a wavelet decomposition and an original technique to compare them based on evidence theory ;
- The **chapter 5** uses these descriptors in **various remote sensing problem** (segmentation, classification, estimation of the orientation, front detection) ;
- Finally, the **chapter 6** is devoted to the **change detection** problem. We propose several solutions for binary and multi-label detection that are based on pre-segmented images (that can in practice be provided by external sources) or not. In this latter case we exploit patches of various size and model selection.

It should be pointed out that these works (and in particular the second part) have mainly been motivated by the research challenges of the COSTEL group. As a matter of fact not only the methodology was necessary but it was also required that possibly non-specialists researchers (from an image processing and computer science point of view) can easily apply the approaches to massive databases. This point has had an influence on some methodological choices.

Let us now turn to the first part of this document.

Première partie

Low resolution remote sensing images : flow analysis and tracking

Introduction

This first part concentrates on the analysis of Low Spatial Resolution (LSR) data. Related applications mainly concern the dynamics of the atmosphere and the ocean since the rate of acquisition of such images is high compared to the involved phenomena.

We first have worked on motion estimation techniques for such flows. We have distinguished the situations where only a pair of images (chapter 1) and where a complete sequence (chapter 2) is available. The involved methodological tools indeed differ in the sense that one can take benefit of some dynamical laws issued from fluid mechanics when a sequence is accessible. Finally, in chapter 3 we present other works using the data assimilation methodological framework presented in chapter 2 for various computer vision problems (segmentation, data reconstruction, multi-resolution analysis and crowd analysis).

Chapitre 1

Motion estimation from a pair of images

Sommaire

1.1 Overview

The estimation of motion from a pair of images, commonly named "optical flow", is the task that consists in extracting the apparent velocity field between two images. This is an open and intensively studied problem in computer vision since the seminal works of Horn & Schunck [Horn 1981] and Lucas & Kanade [Lucas 1981].

It is obvious that applications of optical-flow are unlimited. As non-exhaustive examples, one can cite works related to scene and action analysis [Yacoob 1996], video coding and compression [Belfiore 2005], video surveillance [Cohen 1999], segmentation [Mémin 1998], medicine [Cuzol 2007, Mikic 1998] or fluid and geophysical motion analysis [Corpetti 2002, Heitz 2009, Papadakis 2008, Ruhnau 2004, Sakaino 2008]. This last application is strongly connected to flows observed in Low Spatial Resolution images (LSR) and proposed techniques of this document belong to this family of approaches. The reader can refer to [Barron 1994, Galvin 1998, Mitiche 1996] for presentations and overviews of optical flow techniques and to [Baker 2007] for an introduction to the middleburry web-site [1] which is

1. http://vision.middlebury.edu/flow/data/

devoted to the analysis and comparison of advanced optical flow techniques by providing sequences and comparison tools.

To estimate the optical flow from a pair of images, one should start with a so-called *observation model* that links the image luminance to the velocity to estimate. As we will explain in the next section, a single observation model leads to ill-posed problems and we need to add some constraints. These latter are generally issued from a spatial prior on the distribution of the motion field and are either called *smoothing* or *regularization terms*.

The next section presents the general ideas of motion estimation techniques. In section 1.3 we discuss about optical flow estimation in physics and especially in applications related to fluid flows. In sections 1.4 and 1.5 we present some contributions for fluid motion estimation.

1.2 General principles

1.2.1 Notations

In this document, the velocity field is $\boldsymbol{v}(\boldsymbol{x}) = (u(\boldsymbol{x}), v(\boldsymbol{x}))^T$ and is defined at a position $\boldsymbol{x} \in \Omega$ between two images (generally $I_{t-1}(\boldsymbol{x}) = I(\boldsymbol{x}, t-1)$ at time $t-1$ and $I_t(\boldsymbol{x}) = I(\boldsymbol{x}, t)$ at time t). When they are not needed for the comprehension, we omit the spatial or temporal indexes.

1.2.2 Observation model

The most used and simple observation model proposed for optical-flow estimation is the brightness consistency assumption :

$$\frac{dI}{dt} = \frac{\partial I(\boldsymbol{x}, t)}{\partial t} + \boldsymbol{v}(\boldsymbol{x}, t) \cdot \nabla I(\boldsymbol{x}, t) \sim 0 \tag{1.1}$$

and assumes that the points $\boldsymbol{x}$ keep their intensity along their displacements, the luminance I being viewed as a continuous function and $\nabla = (\partial/\partial x, \partial/\partial y)^T$ being the gradient operator. Applied to a pair of images this relation reads :

$$I_t(\boldsymbol{x} + \Delta t \boldsymbol{v}(\boldsymbol{x})) - I_{t-1}(\boldsymbol{x}) = 0 \Rightarrow \frac{I_t(\boldsymbol{x}) - I_{t-1}(\boldsymbol{x})}{\Delta t} + \boldsymbol{v}(\boldsymbol{x}) \cdot \nabla I_t(\boldsymbol{x}) = 0 \tag{1.2}$$

where we have a first order Taylor development of the conservation constraint $I_t(\boldsymbol{x} + \Delta t \boldsymbol{v}(\boldsymbol{x})) - I_{t-1}(\boldsymbol{x}) = 0$ around $\Delta t \boldsymbol{v}(\boldsymbol{x})$ and Δt is the time between two images (by convention we assume $\Delta t = 1$). This creates a link between the displaced frame difference $I_t(\boldsymbol{x}) - I_{t-1}(\boldsymbol{x})$, the spatial gradients of the second image $\nabla I_t(\boldsymbol{x})$ and the velocity. The equations in (1.1-1.2) are commonly named the *optical-flow constraint equations* (OFCE) and are the basis of huge amount of studies [2]. At this step, it is easy to observe that :

1. in homogeneous areas, all terms vanish and there is an infinity of solutions ;
2. because of the projection $\boldsymbol{v} \cdot \nabla I$, only the normal component to the photometric gradients can be extracted with such a formulation. This problem is known as the "aperture problem".

Therefore, the relation in (1.1) is in itself not sufficient to extract the velocity field. We need to add some constraints on the velocity to estimate.

2. In the rest of the document, when we mention the OFCE, we refer to the continuous version (1.1).

1.2.3 Spatial constraints

All the existing constraints rely on a prior knowledge of the spatial distribution of the velocity field. Roughly, one can classify the main ones into three families :

1. correlation based techniques : $\boldsymbol{v}(\boldsymbol{x})$ is locally estimated as the one which maximizes a correlation criteria between a window centered in $\boldsymbol{x}$ in the first image and a displaced window centered in $\boldsymbol{x}+\boldsymbol{v}(\boldsymbol{x})$ in the second image. The size of the correlation window plays as a spatial prior knowledge on the velocity ;
2. Lucas & Kanade based techniques : $\boldsymbol{v}(\boldsymbol{x})$ is locally estimated by assuming that its value is homogeneous in a neighborhood of $\boldsymbol{x}$;
3. Horn & Schunck based techniques : the velocity $\boldsymbol{v}$ is globally estimated on the whole image plane Ω by minimizing a cost function composed of an observation and a smoothing term.

Correlation

As mentioned above, the general principle is to find at each point $\boldsymbol{x} \in \Omega$ the velocity that maximizes a correlation criteria $\mathcal{C}_{\mathcal{W}}$ in a local window $\mathcal{W}(\boldsymbol{x})$ centered in $\boldsymbol{x}$:

$$\boldsymbol{v} = \max_{\boldsymbol{v}=\{-U,\dots,U\}\times\{-V,\dots,V\}} \sum_{\boldsymbol{x}\in\mathcal{W}(\boldsymbol{x})} \mathcal{C}_{\mathcal{W}}\left(I(\boldsymbol{x}+\boldsymbol{v},t), I(\boldsymbol{x},t-1)\right). \tag{1.3}$$

The state space of possible solutions for $\boldsymbol{v}$ is discrete. Usually the correlation criterion $\mathcal{C}_{\mathcal{W}}$ assumes the OFCE and is either based on the displaced frame difference (first term of relation (1.2)), the cross-correlation :

$$\mathcal{C}_{\mathcal{W}}\left(I(\boldsymbol{x}+\boldsymbol{v},t), I(\boldsymbol{x},t-1)\right) = I(\boldsymbol{x}+\boldsymbol{v},t) I(\boldsymbol{x},t-1) \tag{1.4}$$

or the normalized cross-correlation :

$$\mathcal{C}_{\mathcal{W}}\left(I(\boldsymbol{x}+\boldsymbol{v},t), I(\boldsymbol{x},t-1)\right) = \frac{(I(\boldsymbol{x}+\boldsymbol{v},t) - \overline{I}(\boldsymbol{x}+\boldsymbol{v},t))(I(\boldsymbol{x},t-1) - \overline{I}(\boldsymbol{x},t-1))}{\sigma_{\mathcal{W},I(\boldsymbol{x}+\boldsymbol{v},t)}\sigma_{\mathcal{W},I(\boldsymbol{x},t-1)}} \tag{1.5}$$

where $\overline{I}(\bullet)$ and $\sigma_{\mathcal{W},I(\bullet,t)}$ are the empirical mean and standard deviation of $\overline{I}(\bullet)$ in a window $\mathcal{W}$. Note that taking benefit of interesting properties of the Fourier transform, in particular that a convolution product in the spatial domain becomes a simple product in the Fourier space, very efficient correlation techniques can be implemented [Foroosh 2002, Jahne 1998].

Lucas & Kanade

In the work of Lucas & Kanade [Lucas 1981], the authors have assumed for each location $\boldsymbol{x}$ that the velocity is locally constant. It is estimated as :

$$\boldsymbol{v} = \min_{\boldsymbol{v}=(u,v)^T} \int_{\Omega} g_\sigma * \left(\frac{\partial I(\boldsymbol{x},t)}{\partial t} + \boldsymbol{v}(\boldsymbol{x},t)\cdot\nabla I(\boldsymbol{x},t)\right)^2 d\boldsymbol{x}, \tag{1.6}$$

where g_σ is a Gaussian window of standard deviation σ in which the velocity $\boldsymbol{v}$ is assumed to be homogeneous. When we cancel the derivative of the previous relation with respect to $\boldsymbol{v}$, one gets :

$$\boldsymbol{v} = -\left(g_\sigma * \begin{bmatrix} I_x^2 & I_xI_y \\ I_xI_y & I_y^2 \end{bmatrix}\right)^{-1} g_\sigma * \begin{bmatrix} I_xI_t \\ I_yI_t \end{bmatrix}, \tag{1.7}$$

where $I_\bullet = \partial I/\partial\bullet$. To guarantee a good conditioning of the previous matrix to invert, the spatial gradients must not vanish. The gaussian smoothing aims in fact at alleviating

homogeneous areas by capturing the spatial information at a scale related to σ. Therefore the estimated velocity is intrinsically related to this scale σ. Its choice is then crucial : a too small value is likely to keep constant areas whereas large values will smooth out the fine scale structures. If one is able to fix it, the Lucas & Kanade estimator is very efficient and because of its simplicity, it is still largely used in many vision systems [Baker 2004].

Horn & Schunck

In the work of Horn & Schunck [Horn 1981], the authors have combined the brightness consistency term with the minimization of a first-order spatial regularizer that promotes solutions with a global consistency of the motion field. Therefore, the velocity is estimated by minimizing :

$$\boldsymbol{v} = \min_{\boldsymbol{v}=(u,v)^T} \int_\Omega \left(\frac{\partial I(\boldsymbol{x},t)}{\partial t} + \boldsymbol{v}(\boldsymbol{x},t) \cdot \nabla I(\boldsymbol{x},t) \right)^2 + \alpha \left(|\nabla u(\boldsymbol{x})|^2 + |\nabla v(\boldsymbol{x})|^2 \right) d\boldsymbol{x}, \tag{1.8}$$

where α is a parameter balancing the relative influence of the observation model and the smoothing term. This regularization aims at generating smooth velocity fields with low spatial gradients.

1.2.4 Related works

A substantial number of approaches has been proposed for various video applications based on the OFCE and some spatial constraints. Correlation techniques are for instance the basis of almost all video-compression methods [Girod 2005, Wiegand 2003]. As the Lucas & Kanade technique gives in a fast way a valuable motion information, it can efficiently be used as a dynamic information for a tracking system or for any process requiring a consistent (but not very precise) motion information. The reader can refer to [Baker 2004] for a presentation of applications related to Lucas & Kanade. The last three decades, huge number of methods have been proposed by the computer vision community on the basis of Horn and Schunck's seminal work. One of the key issue comes from the fact that the first order smoothing term in (1.8) can be viewed as the convergence of an isotropic diffusion with a constant parameter :

$$\begin{cases} \dfrac{\partial u}{\partial \tau} = \Delta u = \operatorname{div}(g \nabla u) \\ \dfrac{\partial v}{\partial \tau} = \Delta v = \operatorname{div}(g \nabla v), \end{cases} \tag{1.9}$$

where $g = 1$, τ is an artificial time, $\Delta = \partial^2/\partial x^2 + \partial^2/\partial y^2$ is the Laplacian operator and $\operatorname{div}\boldsymbol{v} = \partial u/\partial x + \partial v/\partial y$ is the divergence. This is easily demonstrated using the Euler-Lagrange equations associated to the functional in (1.8). The fact that $g = 1$ indicates an isotropic diffusion in any directions. Therefore, it removes noisy distributions but on the drawback, discontinuities are not well extracted. Many authors have then designed very efficient techniques for diffusing in a proper way around the discontinuities, in particular based on new regularization terms or advanced minimization and representation strategies [Black 1992, Brox 2004, Fitzpatrick 1988, Lempitsky 2008, Mémin 1998, Nagel 1990, Nesi 1993, Papenberg 2006, Schunck 1986, Sun 2010a, Sun 2010b, Tetriak 1984, Weber 1995, Wedel 2008, Weickert 2001a, Xu 2008]. Comparative performance evaluations of some of these techniques can be found in [Baker 2007, Barron 1994, Galvin 1998] and in the middleburry website.

Apart from the correlation techniques, the Lucas & Kanade and Horn & Schunck are based on the differential version of the OFCE and therefore only hold for small displacements. To accurately measure the large displacements likely to occur, many authors have

proposed a multi-resolution framework [Bergen 1992]. The general idea consists in successively estimating fine displacements that correspond to a specific range of the motion. A usual way to do it is to divide J times the size of the lines and rows of image by a factor 2 and to perform the estimation from the coarsest to the finest image (more details about multi-resolution are presented in section 3.4 of chapter 3).

Leu us now focus on the motion estimation problem for physical images and in particular fluid flows.

1.3 Application for fluid dynamics

Many domains related to physics exploit image sequences to observe a target event : meteorology, oceanography, biology, fluid mechanics, medicine, ... Depending on the acquisition process, the resulting images are often specific and need a dedicated processing to assess the cinematic information.

The **correlation techniques** are intensively used in meteorology and experimental fluid mechanics. In meteorology, operational centers estimate winds from the displacements of clouds observed on images using correlation-based approaches. Several strategies for fast implementations, velocity post-processing or temporal consistency have been proposed as for examples methods in [Fujita 1968, Leese 1971, Menzel 2001, Schmetz 1987, Smith 1971, Wu 1995, Wu 1997]. The reader will find in [Menzel 2001] references concerning correlation techniques for meteorology. In experimental fluid imagery, it is common to visualize and analyze flows with particles : the fluid flow is seeded with small particles and enlighten through a laser sheet. These techniques are usually referred as PIV (Particles Image Velocimetry) methods. On such PIV data, the most efficient available tools rely on advanced correlation techniques, as for instance using adaptive window search [Adrian 1991, Adrian 2005, Becker 2008, Raffel 2007, Tropea 2007]. Even if correlation techniques enable to extract only displacement vectors on the image lattice, many extended methods have been proposed to achieve "sub pixel" accuracy. All these correlation techniques share nevertheless some common limitations which prevent a comfortable use :

1. due to the finite size of the interrogation area (and particle drop out in PIV), a "*loss of pairing*" may alter the estimation. In this case, the maximum of correlation does not correspond to the actual motion. The definition of the size of the interrogation window is indeed very problematic to extract a relevant motion in accordance with the observed phenomenon ;
2. The existence of velocity and speeding gradient in the interrogation region introduces a bias towards the lower displacements and higher seeded sub-regions as a result of the more frequent pairings. For large interrogation windows, this is very problematic. It is nevertheless important to note that this can be (at least partially) overcome using variable size windows and deformable grids ;

Roughly, these techniques perform well for large scales but appear too limited for smaller scale structures.

Since one decade, **global approaches** using the minimization of a cost-function specifically designed to fluid flows have been proposed in order to cope with the difficulties associated to correlation. One can cite techniques embedding a more physically-based observation term issued from fluid mechanics laws [Arnaud 2006, Cassisa 2010, Corpetti 2002, Corpetti 2006, Fitzpatrick 1988, Haussecker 2001, Héas 2007, Liu 2008]. Such terms allow for instance to deal with the influence of small-scale structures or changes of density (and therefore of luminance if the image is linked to the density) submitted by a fluid along its displacement (dilatations, dissipation, ...). As for the spatial constraints, let us first note

that any velocity field $\boldsymbol{v}$ can be decomposed in an irrotational $\boldsymbol{v}_{irr}$, a solenoidal $\boldsymbol{v}_{sol}$ and a harmonic $\boldsymbol{v}_{har}$ component yielding the so-called Helmholtz decomposition. The irrotational term has no rotation (or curl) whereas the solenoidal part has no divergence. The harmonic component is div-curl free. For a $2D$ velocity field $\boldsymbol{v} = (u, v)^T$, the divergence and curl are defined as :

$$\begin{cases} \text{div}\boldsymbol{v} = \nabla \cdot \boldsymbol{v} = \dfrac{\partial u}{\partial x} + \dfrac{\partial v}{\partial y} \\ \text{curl}\boldsymbol{v} = \nabla \wedge \boldsymbol{v} = \dfrac{\partial v}{\partial x} - \dfrac{\partial u}{\partial y}. \end{cases} \tag{1.10}$$

The figure FIG. 1.1 illustrates this decomposition.

It can be shown that a first order smoothing term as the one in (1.8) tends to promote velocity fields with low vorticity and divergence (see [Corpetti 2002] for the demonstration). This is problematic since these quantities are often used as reliable descriptors of the flow. Therefore several authors have proposed motion estimation techniques able to recover more accurately these quantities. Related approaches either use a representation of the velocity on some basis dedicated to fluids (like div-curl splines [Suter 1994] or vortex particles [Chorin 1973], see [Amodei 1991, Cuzol 2005, Cuzol 2008, Isambert 2008, Suter 1994] for examples) or use an advanced smoothing terms based on a physical law or on the preservation of the divergence and the vorticity [Corpetti 2002, Corpetti 2006, Ruhnau 2007, Yuan 2007] (the next section presents the specific smoothing term we proposed in [Corpetti 2002]). Note that recently, Héas and coworkers have proposed a smoothing based on the spectrum of the vorticity [Héas 2009].

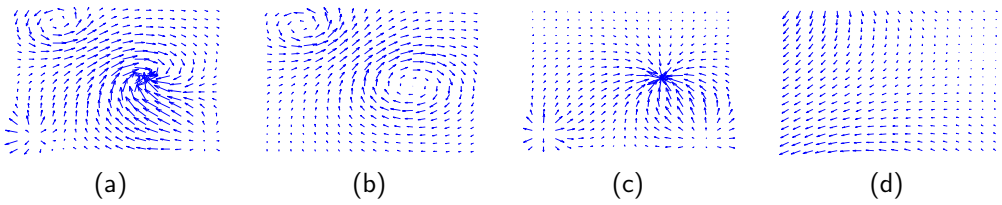

FIGURE 1.1 – **Helmholtz decomposition** (a) : a motion field ; (b) its solenoidal part ; (c) its irrotational part ; (d) its harmonic part

Finally, to take advantage of local approaches that estimate well the large scales and global approaches that deal in a proper way with the fineer scale structures, some authors have proposed **hybrid techniques** [Alvarez 2009, Bruhn 2005, Héas 2008, Héas 2007, Heitz 2008, Sugii 2000]. The reader can refer to [Heitz 2009] for a recent and very complete overview of motion estimation techniques for fluid flows. In the next section we introduce briefly the fluid dedicated estimator we proposed in [Corpetti 2002, Corpetti 2006].

1.4 A proposed fluid motion estimator

In 2002, we have proposed a technique for estimating dense fluid flows. We started from two observations :

1. the observation of compressible fluids or of integrated quantities along the vertical axis (as in meteorology) generate a 2D divergence in the image plane where a variation of density along the displacement is likely to appear. This generates a loss of intensity along the displacement which is in contradiction with the OFCE, as illustrated in figure 1.2 ;

2. it can easily be proved by writing the Euler-Lagrange equations that minimizing a first order smoothing term is equivalent to minimize the divergence and the vorticity of the flow. This is prejudicial for fluids since these quantities can reach high values.

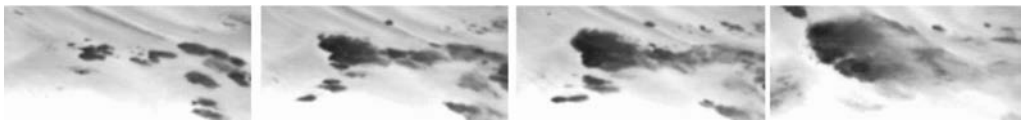

FIGURE 1.2 – **A convective cell phenomenon.** Because of the vertical motions, we have a 2D divergence that generates a loss on intensity along the displacement of each points.

To answer to these difficulties, we have proposed dedicated observation and smoothing terms.

1.4.1 Continuity equation based observation model

If the image irradiance is related to the density of a physical quantity (mass in transmittance imagery, dye, smoke, particle concentration in particle image velocimetry, heat in infrared imagery, the reader will find in [Corpetti 2002, Fitzpatrick 1988, Haussecker 2001] an analysis of this link depending on the visualization process) transported by the flow under a global conservation constraint, this density ρ obeys the continuity equation :

$$\frac{\partial \rho}{\partial t} + \mathrm{div}(\rho \boldsymbol{V}) = 0, \tag{1.11}$$

where $\boldsymbol{V}$ is the three-dimensional velocity field. This equation derives from the global conservation assumption by stating that the temporal variation of the quantity under consideration within an infinitesimal volume amounts exactly to the flux of this quantity through the boundary surface of the volume.

One can then assume by analogy that the two-dimensional image brightness I and the apparent velocity $\boldsymbol{v}$ satisfy :

$$\frac{\partial I}{\partial t} + \mathrm{div}(I\boldsymbol{v}) = 0. \tag{1.12}$$

For incompressible fluids such as water, the three-dimensional flow is divergence free. Assuming the resulting apparent bi-dimensional flow is divergence free as well, the bi-dimensional continuity equation above amounts exactly to the brightness constancy constraint (1.1), since $\mathrm{div}(I\boldsymbol{v}) = \boldsymbol{v} \cdot \nabla I + I\mathrm{div}\boldsymbol{v}$. In other cases, *i.e.* when flows are compressible such as in meteorological satellite imagery, the brightness constraint expressed by (1.12) differs from the standard one, (1.1), by the additional term $I\mathrm{div}\boldsymbol{v}$. This terms links the divergence to the loss of intensity in images.

It is then possible to apply this new observation term as an alternative to the OFCE in (1.1). In addition, by analogy to the integrated version of the OFCE in (1.2) that holds what ever the magnitude of the displacement is, it is possible to design an integrated version of the relation in (1.12). To this end we first rewrite (1.12) using the identity $\mathrm{div}(I\boldsymbol{v}) = I\mathrm{div}\boldsymbol{v} + \nabla I \cdot \boldsymbol{v}$ and the definition $\frac{dI}{dt} = \frac{\partial I}{\partial t} + \nabla I \cdot \boldsymbol{v}$ of the total derivative. We get :

$$\frac{dI}{dt} + I\mathrm{div}\boldsymbol{v} = 0. \tag{1.13}$$

Integrating this ordinary differential equation with initial condition $I(\boldsymbol{x}, t-1)$ yields :

$$I(\boldsymbol{x} + \Delta t \boldsymbol{v}(\boldsymbol{x}), t) = I(\boldsymbol{x}, t-1) \exp\left(-\Delta t \mathrm{div}\boldsymbol{v}(\boldsymbol{x})\right). \tag{1.14}$$

where $\Delta t\boldsymbol{v}(\boldsymbol{x})$ is the displacement between the images (usually by convention $\Delta t = 1$).

According to this constraint, the brightness is scaled by the factor $\exp\big(-\mathrm{div}\Delta t\boldsymbol{v}\big)$. It decreases (resp. increases) for motions with positive (resp. negative) divergence. When the divergence is zero, this constraint amounts exactly to the OFCE (1.2).

1.4.2 Div-Curl smoothing term

As already mentioned, the key information included in divergence and vorticity will be partly ignored with a first-order regularization. Furthermore, in the prospect of using an observation model which makes explicit use of the divergence like the one of the previous section, an under-estimation of the divergence field would be critical.

Hence, we have proposed to use a second-order regularization. Since the divergence and the vorticity of the flow are much more physically meaningful than the spatial gradient, the second-order div-curl regularizer introduced by Suter [Suter 1994]

$$\min_{\boldsymbol{v}} \int_{\Omega} |\nabla \mathrm{div}\boldsymbol{v}|^2 + |\nabla \mathrm{curl}\boldsymbol{v}|^2 \tag{1.15}$$

is particularly appealing. We have however modified it by introducing two auxiliary scalar fields, ζ and D, which will constitute direct estimates of the divergence and vorticity, respectively. The regularizer is then given by :

$$\min_{\boldsymbol{v},D,\zeta} \int_{\Omega} |\mathrm{div}\boldsymbol{v} - D|^2 + \lambda f_2(|\nabla D|) + \int_{\Omega} |\mathrm{curl}\boldsymbol{v} - \zeta|^2 + \lambda f_2(|\nabla \zeta|), \tag{1.16}$$

where f_2 is a quadratic or a more sophisticated penalization term that prevents from discontinuities [Delanay 1998, Geman 1992, Huber 1981]. The first part of each integral encourages the displacement to comply with the current divergence and vorticity estimates D and ζ, through a quadratic goodness-of-fit. The second part equips the divergence and the vorticity estimates with a robust first-order regularization favoring piece-wise smooth configurations. The benefit of this smoothing term, compared to the one in (1.15) is twofold. First, it prevents from dealing with fourth order partial differential equations (PDE) resulting from the associated Euler-Lagrange equations. Second, the two scalar fields D and ζ permits to introduce even more sophisticated priors on the divergence and the vorticity of the imaged flow, for instance coming from in situ measurements.

1.4.3 Some results

The figure FIG. 1.3 presents an example of motion estimation on LSR images issued from the water vapor channel of the Meteosat sensor. We used an estimator composed of the two energy terms of the last section, applied on successive pair of images. The sequence exhibits a rotating structure on the left part and an explosion of convective cells (characterized by strong divergence values) on the right part [3]. On FIG. 1.3(a,b) we have superimposed to the last image of the sequence the reconstructed trajectories obtained by integrating the successive instantaneous velocity fields using the proposed approach (FIG. 1.3(a)) and a Horn & Schunck based one (FIG. 1.3(b)). On these images, the luminance is poorly contrasted and the estimation in FIG. 1.3(b) is mainly influenced by the first-order smoothing term, yielding a quite smooth motion field without the rotating and diverging structures. At the opposite, the trajectories in FIG. 1.3(a) are more in accordance with the observed phenomenon. These observations are confirmed on the instantaneous velocity field

3. The complete sequence and other results can be seen at
http://www.irisa.fr/vista/Themes/Demos/MouvementFluide/fluide.html

illustrated in the second line of the figure. The last line presents the maps of divergence and vorticity corresponding to the velocity field in FIG. 1.3(c) where the different structures are clearly highlighted.

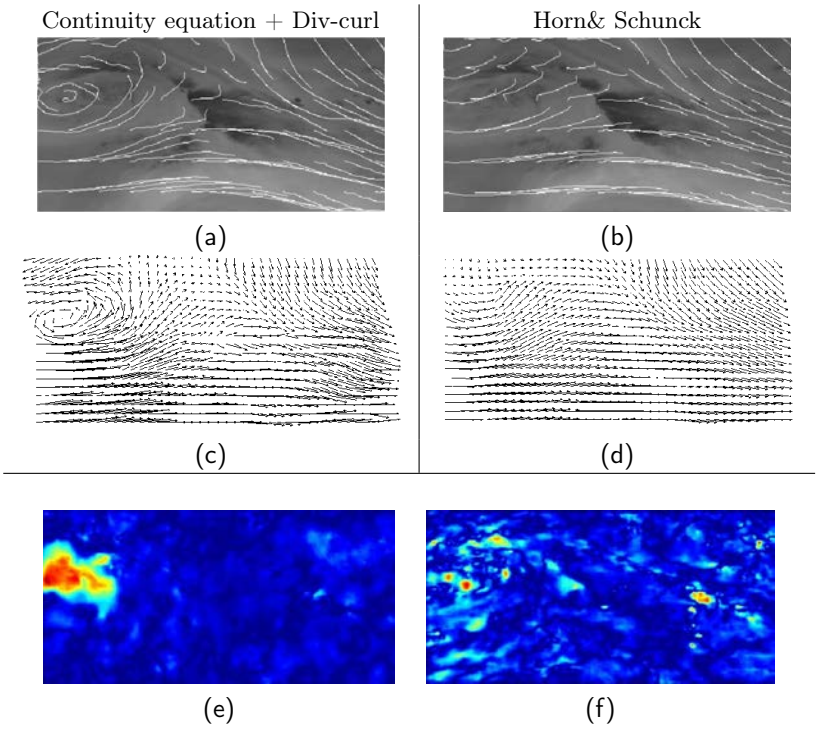

FIGURE 1.3 – **Motion estimation on LSR data issued from Meteosat.** (a,b) : reconstructed trajectories integrated from estimated motion fields and (c,d) an instantaneous velocity field of the sequence obtained with our proposed estimator and a Horn & Schunck [Horn 1981] based one. In (e,f) are presented the maps of estimated vorticity ζ and divergence D for the velocity field in (c)

More complete quantitative and qualitative results are in [Corpetti 2002, Corpetti 2006]. In order to assess the quality of the estimator with respect to fluid mechanics properties, we have analyzed several specific flows observed with PIV techniques with known properties. Here we focus on the study of an area located behind a cylinder submitted to a homogeneous flow, as illustrated in figure FIG. 1.4 (a). We have compared our motion estimation technique to the PIV software of LA VISION [4] based on correlation. In figure FIG. 1.4(b-c), we present two instantaneous velocity fields on which we can observe that they are in accordance each others. However, the one issued from our technique is dense (one vector per pixel) whereas the one issued from PIV has one vector out of 32 pixels, because of limitations due to the size of the interrogation window. On figure FIG. 1.4(d-e), we have depicted for a series of 3000 experiments the velocity profiles taken vertically just after the cylinder of the mean horizontal $\overline{u}$ and vertical $\overline{v}$ component. As one can observe, they are in accordance but the one we propose has the advantage to provide dense velocity fields.

This estimator performs then efficiently. The introduction of some physical knowledge in the observation and smoothing terms enables to recover more properly the different structures of the flow. However, let us note that the physical models are defined in a continuous formalism whereas the data are available only on some discrete grid points.

4. http://www.lavision.de/

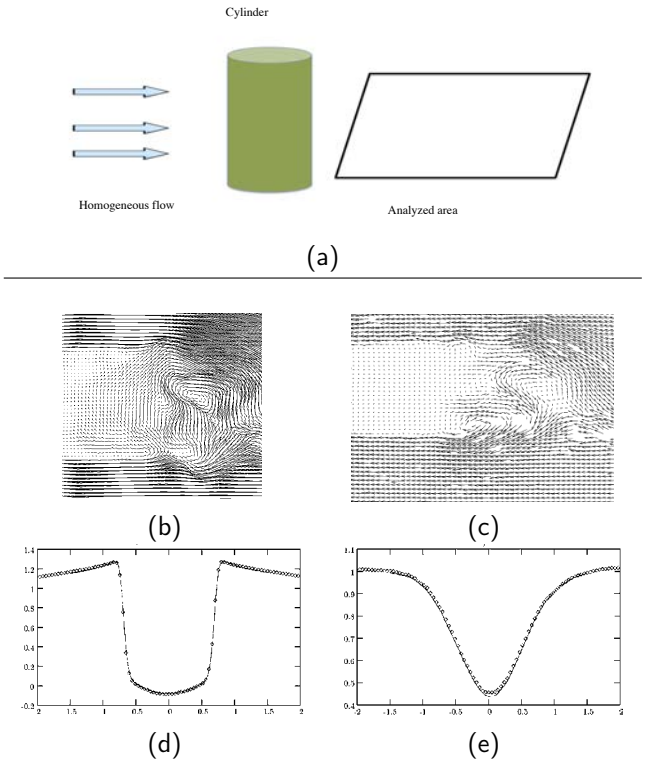

FIGURE 1.4 – **"Cylinder" experiment.** (a) : a scheme of the analyzed area ; (b) an instantaneous velocity field estimated with our technique (1 vector over 128 is depicted) ; (c) : an instantaneous velocity field estimated with LA VISION software (1 vector over 16 is depicted) ; (d-e) : mean vertical velocity profiles just after the cylinder of the $\overline{u}$ and $\overline{v}$ components (plain lines : our technique, circles : LA VISION)

Recently, we have proposed an extension of the formulation of the total derivative dI that takes into account the uncertainty between grid points (and more generally uncertainty due to homogeneous areas). This is realized using a stochastic formalism and is presented in the next section.

1.5 An alternative observation model based on stochastic uncertainties

As just mentioned, the conventional optical flow constraint relation (1.1) or alternative formulations as the one we proposed in (1.13) are defined on the basis of the differential dI of the luminance function known only on spatial and temporal discrete point positions (related to the image sequence spatio-temporal lattice). This is somewhat a strong constraint since in practice, the grid points on which is defined the luminance is transported by a flow itself known only up to the same discrete positions. It results from this discretization process an inherent uncertainty on the point locations that can reveal to be of important magnitude when are involved strong motions, large inter frames lapse rate or crude spatial discretization (associated for instance to large spatial scales measurements). The idea is therefore to encode such a location uncertainty as a random variable and to incorporate the

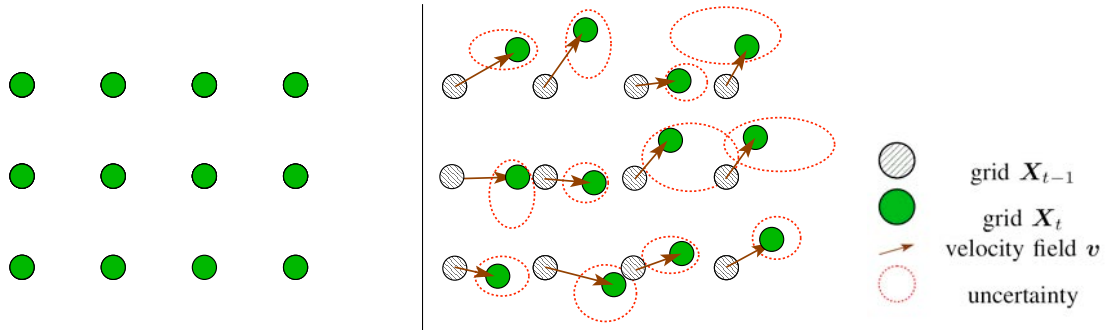

(a) : Grid at time $t-1$ (b) : Displaced grid at time t

FIGURE 1.5 – **Displacement of the grid of points.** The initial grid at time $t-1$ in (a) is transported by the velocity field $\boldsymbol{v}$ to reach the configuration at time t represented in (b), up to some uncertainties (dashed lines).

uncertainty transportation into the various observation terms (in this part we use only the OFCE to validate the principle). Stochastic calculus provides the differentiation rules needed to formalize such evolution law of uncertainty terms. To this end, we rewrite the evolution of the image luminance on an image grid where these uncertainties are integrated. This is the scope of the next section.

1.5.1 Stochastic luminance function

Representing as a vector $\boldsymbol{X} = (\boldsymbol{X}^1, \ldots, \boldsymbol{X}^m)^T$ a grid of $2D$ points ($\boldsymbol{X}^s \in \mathbb{R}^2$), the "pixel" grid $\boldsymbol{X}_{t-1}$ of the images is represented by the position of a grid $\boldsymbol{X}$ at the initial time, set to $t-1$ (see figure 1.5 (a)). This grid is driven by a velocity field $\boldsymbol{v}(\boldsymbol{X}_{t-1}, t-1)$ defined on the initial grid $\boldsymbol{X}_{t-1}$ to generate the new point positions $\boldsymbol{X}_t$ at time t (see figure 1.5 (b)). We then rewrite the image luminance as the function of a stochastic process related to the position of image points. As the velocity $\boldsymbol{v}$ to estimate transports the grid from $\boldsymbol{X}_{t-1}$ to $\boldsymbol{X}_t$ up to a Brownian motion, we can write :

$$d\boldsymbol{X}_t = \boldsymbol{v}(\boldsymbol{X}_{t-1}, t-1)dt + \boldsymbol{\Sigma}(t, \boldsymbol{X}_t)d\mathbf{B}_t, \tag{1.17}$$

where $\mathbf{B}_t = (\mathbf{B}_t^1, ..., \mathbf{B}_t^m)^T$ is a multidimensional standard Brownian motion of $\mathbb{R}^{2m}$, $\boldsymbol{\Sigma}$ a $(2m \times 2m)$ covariance matrix and $d\boldsymbol{X}_t = \boldsymbol{X}_t - \boldsymbol{X}_{t-1}$ represents the difference between the grid positions. The luminance function I usually defined on spatial points $\boldsymbol{x} = (x, y)$ (as in the previous section) at time t is here defined on the grid as a map from $\mathbb{R}^+ \times \mathbb{R}^{2m}$ into $\mathbb{R}^m$ and is assumed to be $C^{1,2}(\mathbb{R}^+, \mathbb{R}^{2m})$. Its differential is obtained following the differentiation rules of stochastic calculus (the so called Îto formulae) that gives the expression of the differential of any continuous function of an Îto diffusion of the form (1.17) (see [Oksendal 1998] for an introduction to stochastic calculus) :

$$\begin{aligned} dI(\boldsymbol{X}_t, t) = & \frac{\partial I}{\partial t}dt + \sum_{i=(1,2)} \frac{\partial I(\boldsymbol{X}_t, t)}{\partial x_i} dX_t^i + \\ & \frac{1}{2} \sum_{(i,j)=(1,2)\times(1,2)} \frac{\partial^2 I(\boldsymbol{X}_t, t)}{\partial x_i \partial x_j} d < X_t^i, X_t^j > . \end{aligned} \tag{1.18}$$

The term $< X_t^i, X_t^j >$ denotes the joint quadratic variations of X^i and X^j and can be computed according to the following rules :

$$\begin{aligned} &< dB^i, dB^j >= \delta_{ij} t \\ &< h(t), h(t) >=< h(t), dB^i >=< B^j, h(t) >= 0, \end{aligned} \tag{1.19}$$

where $\delta_{ij} = 1$ if $i = j$, $\delta_{ij} = 0$ otherwise and $h(t)$ is a deterministic function. Compared to classical differential calculus, new terms related to the Brownian random motions have been introduced in this stochastic formulation. A possible way to represent the stochastic part of (1.17) is to use an isotropic uncertainty variance map $\sigma(X_t, t) : \mathbb{R}^+ \times \mathbb{R}^{2m} \to \mathbb{R}^m$

$$\boldsymbol{\Sigma}(\boldsymbol{X}_t, t) d\mathbf{B}_t = \mathrm{diag}(\sigma(\boldsymbol{X}_t, t)) \otimes \mathbb{I}_2 d\mathbf{B}_t, \tag{1.20}$$

where $\mathbb{I}_2$ is the (2×2) identity matrix and $\otimes$ denotes the Kronecker product. Alternatively, one can use anisotropic intensity-based uncertainties along the normal (with a variance σ_η) and the tangent (with a variance σ_τ) of the photometric contour following :

$$\boldsymbol{\Sigma}(\boldsymbol{X}_t, t) d\mathbf{B}_t = \mathrm{diag}(\sigma_\eta(\boldsymbol{X}_t, t)) \otimes \boldsymbol{\eta} dB_t^\eta + \mathrm{diag}(\sigma_\tau(\boldsymbol{X}_t, t)) \otimes \boldsymbol{\tau} dB_t^\tau . \tag{1.21}$$

The vectors

$$\boldsymbol{\eta} = \frac{1}{|\boldsymbol{\nabla} I|} \begin{pmatrix} I_x \\ I_y \end{pmatrix}, \boldsymbol{\tau} = \frac{1}{|\boldsymbol{\nabla} I|} \begin{pmatrix} -I_y \\ I_x \end{pmatrix},$$

represent respectively the normal and tangent of the photometric isolines, B^η and B^τ are two scalar independant multidimensional Brownian noises of $\mathbb{R}^m$ and $I_\bullet = \partial I(X_t, t)/\partial \bullet$ for $\bullet = (x, y)$. Let us now express the luminance variations $dI(X_t, t)$ under such isotropic or anisotropic uncertainties.

Isotropic uncertainties

Applying Îto formula (1.18) to the isotropic uncertainty model yields a luminance variation defined as :

$$dI(\boldsymbol{X}_t, t) = \left(\frac{\partial I}{\partial t} + \boldsymbol{\nabla} I \cdot \boldsymbol{v} + \frac{1}{2} \sigma^2 \Delta I \right) dt + \sigma \boldsymbol{\nabla} I \cdot d\boldsymbol{B}_t. \tag{1.22}$$

Anisotropic uncertainties

Considering the anisotropic uncertainty model (1.21), the corresponding quadratic variations read :

$$d < \boldsymbol{X}_t^1, \boldsymbol{X}_t^1 > = \frac{1}{|\boldsymbol{\nabla} I|^2} (\sigma_\eta^2 I_x^2 + \sigma_\tau^2 I_y^2) dt, \tag{1.23}$$

$$d < \boldsymbol{X}_t^2, \boldsymbol{X}_t^2 > = \frac{1}{|\boldsymbol{\nabla} I|^2} (\sigma_\eta^2 I_y^2 + \sigma_\tau^2 I_x^2) dt, \tag{1.24}$$

$$d < \boldsymbol{X}_t^1, \boldsymbol{X}_t^2 > = \frac{1}{|\boldsymbol{\nabla} I|^2} (I_x I_y)(\sigma_\eta^2 - \sigma_\tau^2) dt, \tag{1.25}$$

and the variation of luminance, dI, reads now :

$$\begin{aligned} dI(\boldsymbol{X}_t, t) = \Bigg(&\frac{\partial I}{\partial t} + \boldsymbol{\nabla} I \cdot \boldsymbol{v} + \frac{\boldsymbol{\nabla} I^T \boldsymbol{\nabla}^2 I \boldsymbol{\nabla} I}{2 |\boldsymbol{\nabla} I|^2} (\sigma_\eta^2 - \sigma_\tau^2) \\ &+ \frac{\sigma_\tau^2 \Delta I}{2} \Bigg) dt + \sigma_\eta \|\boldsymbol{\nabla} f\| dB_t^\eta + \underbrace{\sigma_\tau \boldsymbol{\nabla} I^T \boldsymbol{\tau} dB_t^\tau}_{=0}. \end{aligned} \tag{1.26}$$

In this brightness variation model the stochastic term related to the uncertainty along the tangent vanishes (since the projection of the gradient along the level lines is null).

It is straightforward to remark that the standard brightness consistency assumption is obtained from (1.22) or (1.26) using zero uncertainties ($\sigma = \sigma_\eta = \sigma_\tau = 0$). The proposed stochastic formulation enables thus to use a softer constraint. From this formulation, let us now derive generic models for the evolution of the image luminance transported by a velocity field with local uncertainties.

1.5.2 Uncertainty models for luminance conservation

Starting from a known grid $\boldsymbol{X}_{t-1}$ and its corresponding velocity, the conservation of the image luminance can be quite naturally defined as the conditional expectation $E\left(d\boldsymbol{I}(\boldsymbol{X}_t, t)|\boldsymbol{X}_{t-1}\right)$ between $t-1$ and t. To compute this term, we exploit the fact (as shown in [Corpetti 2011]) that the expectation of any function $\Psi(\boldsymbol{X}_t, t)$ of a stochastic process $d\boldsymbol{X}_t$ (as in (1.17)) knowing the grid $\boldsymbol{X}_{t-1}$ reads :

$$E(\Psi(\boldsymbol{X}_t, t)|\boldsymbol{X}_{t-1}) = \Psi(\boldsymbol{X}_{t-1} + \boldsymbol{v}, t) * \mathcal{N}(0, \boldsymbol{\Sigma}), \tag{1.27}$$

where $\mathcal{N}(0, \boldsymbol{\Sigma})$ is a multidimensional centered Gaussian. This latter relation indicates that the expectation of a function $\Psi(\boldsymbol{X}_t, t)$ knowing the location $\boldsymbol{X}_{t-1}$ under a Brownian uncertainty of variance $\boldsymbol{\Sigma}$ is obtained by a convolution of $\Psi(\boldsymbol{X}_{t-1}+\boldsymbol{v}, t)$ with a centered Gaussian kernel of variance $\boldsymbol{\Sigma}$.

Assuming $\boldsymbol{\Sigma}$ known, our new conservation model $\mathcal{H}(I, \boldsymbol{v})$ for the luminance evolution is hence defined as :

$$\begin{aligned} \mathcal{H}(I, \boldsymbol{v}) &= g_{\boldsymbol{\Sigma}} * (d\boldsymbol{I}(\boldsymbol{X}_{t-1} + \boldsymbol{v}, t)) \\ &= g_{\boldsymbol{\Sigma}} * \left(\boldsymbol{\nabla} I \cdot \boldsymbol{v} + \frac{\partial I}{\partial t} + \mathcal{F}(I) \right), \end{aligned} \tag{1.28}$$

where the operator $\mathcal{F}(I)$ depends on the uncertainty model. For an isotropic diffusion, this latter relation reads

$$\mathcal{H}(I, \boldsymbol{v}) = g_\sigma * \left(\boldsymbol{\nabla} I \cdot \boldsymbol{v} + \frac{\partial I}{\partial t} + \underbrace{\frac{1}{2}\sigma^2 \Delta I}_{\mathcal{F}(I)} \right), \tag{1.29}$$

whereas for the anisotropic version it is :

$$\mathcal{H}(I, \boldsymbol{v}) = g_{\boldsymbol{\Sigma}} * \left(\boldsymbol{\nabla} I \cdot \boldsymbol{v} + \frac{\partial I}{\partial t} + \underbrace{\frac{\boldsymbol{\nabla} I^T \boldsymbol{\nabla}^2 I \boldsymbol{\nabla} I}{2|\boldsymbol{\nabla} I|^2}(\sigma_\eta^2 - \sigma_\tau^2) + \frac{\sigma_\tau^2 \Delta I}{2}}_{\mathcal{F}(I)} \right). \tag{1.30}$$

Comments

If the brightness conservation constraint strictly holds, one obtains $\sigma = \sigma_\eta = \sigma_\tau = 0$; the Gaussian kernels turn to Dirac distributions and relations (1.28), (1.29) and (1.30) correspond to the OFCE in (1.1). The proposed model provides thus a natural extension of the usual brightness consistency data model.

In addition, it is very interesting to observe that the model in (1.29) is closed to turbulence-based models of the form

$$\frac{\partial I}{\partial t} + \boldsymbol{\nabla} I \cdot \boldsymbol{v} + \tau \Delta I = 0, \tag{1.31}$$

where τ is a dissipation coefficient and depends among others on the influence of the finer (unobserved) scales. Its value is the object of numerous studies related to turbulence and Large Eddy Simulation (LES).

In the next section we propose a way to estimate the uncertainties σ_η and σ_τ.

1.5.3 Uncertainty estimation

Assuming an observed motion field $\boldsymbol{v_{obs}}$ that transports the luminance is available (we describe in [Corpetti 2011] a local technique for this estimation), it is possible to estimate the uncertainties $\sigma_\eta(\boldsymbol{x},t)$ and $\sigma_\tau(\boldsymbol{x},t)$ for each location $\boldsymbol{x}$ at time t.

Estimation of σ_η

Computing the quadratic variation of the luminance function dI between $t-1$ and t using the properties in (1.19) yields, for the isotropic or anisotropic version :

$$d\langle I(\boldsymbol{X}_t,t), I(\boldsymbol{X}_t,t)\rangle = \sigma_\eta^2(\boldsymbol{X}_t,t)\|\boldsymbol{\nabla} I(\boldsymbol{X}_t,t))\|^2, \tag{1.32}$$

where $\sigma = \sigma_\eta$ in the isotropic formulation. This quadratic variation can also be approximated from the luminance I by :

$$d\langle I(\boldsymbol{X}_t,t),I(\boldsymbol{X}_t,t)\rangle \approx \left(I(\boldsymbol{X}_t,t) - I(\boldsymbol{X}_{t-1},t-1)\right)^2. \tag{1.33}$$

Considering now that the conditional expectation of both previous terms should be identical, one can estimate the variance by :

$$\sigma_\eta(\boldsymbol{X}_t) = \sqrt{\frac{E\left(I(\boldsymbol{X}_t,t) - I(\boldsymbol{X}_{t-1},t-1)\right)^2}{E\left(\|\boldsymbol{\nabla} I(\boldsymbol{X}_t,t))\|^2\right)}}. \tag{1.34}$$

The expectation in the numerator and denominator are then computed at the displaced point $X_{t-1} + \boldsymbol{v_{obs}}(\boldsymbol{X}_{t-1})$ through the convolution of variance $\boldsymbol{\Sigma}(\boldsymbol{X}_{t-1},t-1)$. A recursive estimation process is thus emerging from equation (1.34). In the case of an anisotropic noise model the uncertainty along the tangent is also needed.

Estimation of σ_τ

It is not possible to estimate uncertainty along the tangent of the photometric contours in a similar way since, as shown in (1.26), this quantity does not appear in the noise associated to the luminance variation and therefore is not involved in the corresponding quadratic variations. Writing the Îto diffusion associated to the velocity projected along the tangent yields

$$\boldsymbol{v}_{\boldsymbol{obs}}^T\boldsymbol{\tau} = \boldsymbol{v}(\boldsymbol{X}_{t-1},t-1)^T\boldsymbol{\tau}dt + \sigma_\tau(t,\boldsymbol{X}_t)dB_t^\tau. \tag{1.35}$$

This scalar product constitutes a scalar Gaussian random field of mean $\mu = \boldsymbol{v}(\boldsymbol{X}_{t-1},t-1)^T\boldsymbol{\tau}$ (assuming $\boldsymbol{v}(\boldsymbol{x},t)$ is a deterministic function) and covariance $(\mathrm{diag}(\sigma_\tau))$. We assume that the scalar product $\boldsymbol{v}^T\boldsymbol{\tau}$ and the tangent uncertainty $\sigma_\tau(t,\boldsymbol{x})$ are sufficiently smooth in space and can be respectively well approximated by the local empirical mean and variance over a local spatial neighborhood $N(\boldsymbol{x})$ of point $\boldsymbol{x}$. Therrfore we estimate σ_τ using :

$$\mu = \frac{1}{|N(\boldsymbol{x})|}\sum_{\boldsymbol{x}_i\in N(\boldsymbol{x})}(\boldsymbol{v_{obs}}(\boldsymbol{x}_i,t-1)^T\boldsymbol{\tau}), \tag{1.36}$$

$$\sigma_\tau^2 = \sqrt{\frac{1}{|N(\boldsymbol{x})|-1}\sum_{\boldsymbol{x}_i\in N(\boldsymbol{x})}(\boldsymbol{v_{obs}}(\boldsymbol{x}_i,t-1)^T\boldsymbol{\tau}-\mu)^2}. \tag{1.37}$$

Summary

The relations (1.29) and (1.30) provide new models for the variation of the image luminance under isotropic or anisotropic uncertainties. In section 1.5.3 we have presented a technique to estimate such uncertainties from an available velocity field. A complete local technique based on Lucas & Kanade and these new observation terms is presented in [Corpetti 2011]. In consists in a multi-resolution and incremental framework using these observation terms. The multi-resolution is also interpreted as a stochastic process (this is introduced in section 3.4.1 of chapter 3), yielding a natural framework to deal with large displacements. The next section focuses on the application of those extended brightness consistency models for motion estimation.

1.5.4 Some results

PIV synthetic data

To validate quantitatively our new observation terms that take into account the discrete nature of the images, we have developed an incremental local motion estimation technique based on Lucas & Kanade that embeds our proposed observation models and estimates the uncertainties (see [Corpetti 2011]). We have used a synthetic pair issued from Direct Numerical Simulation of Navier-Stokes equations representing a 2D turbulent flow to test the technique. The sequence simulates PIV data and one image is visible in figure Fig. 1.6 (a). Numerical values of average angular error (AAE) [Barron 1994] and of the Root Mean Square Error (RMSE) are used as criteria to compare our estimators (isotropic and anisotropic) with some of the state-of-the-art approaches and are depicted in table 1.1. The techniques to which the proposed estimators are compared are :

- a Horn & Schunck estimator (HS) [Horn 1981]
- a commercial software based on correlation (DaVis 7.2 from La Vision GmbH)
- a pyramidal incremental implementation of the Lucas-Kanade estimator – LK – [Lucas 1981]
- a proposed framework completely described in [Corpetti 2011] with the OFCE as an observation model – OFCE – (*i.e* with a zero uncertainty)
- two fluid-dedicated dense motion estimators based on a Div-Curl smoothing with different minimization strategies (DC1–DC2, [Corpetti 2002, Yuan 2007]).
- a fluid-dedicated dense motion estimator based on a turbulence subgrid model in the data-term (TUR, [Cassisa 2010]).

The pyramidal Lucas and Kanade corresponds to our estimator with zero uncertainty and a specific scale parameter (see [Corpetti 2011] for details).

In figure Fig. 1.6, we present an image of the sequence, the estimated flow with the proposed method (anisotropic version) and the error flow field. We have also plotted in figure 1.7 the velocity spectra of the different techniques and compared them with the ground truth. These spectra are represented in a log-log coordinate (figure Fig. 1.7(a)) and a standard-log coordinate system (figure Fig. 1.7(b)) in order to highlight small and large scales respectively.

On table 1.1, one can immediately observe that compared to the other local approaches, our method provides very good results since the global accuracy is highly superior than the Lucas-Kanade (LK) and the commercial software (COM). Compared to dense techniques (HS, TUR, DC1 and DC2), our numerical results are in the same order of magnitude which is a very relevant point. They are competitive with some dense estimation techniques dedicated to fluid flows analysis (TUR–DC1–DC2, [Cassisa 2010, Corpetti 2002, Yuan 2007]). The comparison between the results OFCE, ISO and ANI is very interesting since it highlights

	LK	COM	HS	DC 1	DC 2	TUR	OFCE	ISO	ANISO
AAE	6.07^o	4.58^o	4.27^o	4.35^o	3.04^o	4.49^o	4.53^o	3.59^o	3.12^o
RMSE	0.1699	0.1520	0.1385	0.1340	0.09602	0.1490	0.1243	0.1072	0.0961

TABLE 1.1 – **Quantitative comparisons on the DNS sequence** with a Pyramidal Lucas-Kanade (LK, [Lucas 1981]), a commercial technique based on correlation (COM, LA VISION SYSTEM), Horn & Schunck (HS, [Horn 1981]), two fluid dedicated motion estimators with div-curl smoothing terms (DC 1 : [Corpetti 2002] ; DC2 : [Yuan 2007]), a fluid dedicated motion estimator with turbulence sub-grid models in the data term (TUR, [Cassisa 2010]), our approach using the classic Optical-Flow Constraint Equation (OFCE), our approach in isotropic (ISO) and anisotropic (ANISO).

the benefit of the stochastic formulation of the image luminance. These three results have indeed been estimated with the same incremental estimation framework of [Corpetti 2011] but using an observation model respectively based on the usual OFCE, an isotropic uncertainty (equation (1.29), technique ISO) and an anisotropic uncertainty (equation (1.30), technique ANI). From the corresponding quantitative errors it is obvious that the uncertainty modeling greatly improves the results, especially in the anisotropic approach.

If now one observes the spectra of the velocity shown in figure FIG. 1.7, we see that the small scales (right part of the graph) are much better recovered with the proposed estimators than with the dense ones. The fine scales are generally difficult to estimate and are often smoothed out with the spatial regularizers introduced in the dense techniques. Even if the Lucas-Kanade method seems to exhibit better results on small scales, when observing the figure FIG. 1.7(b), it is obvious to note that large scales are badly estimated with this approach and this yields a very poor overall accuracy (see table 1.1). As for the large scales the results are comparable with the best dense dedicated techniques. We believe hence that our estimator constitutes an appealing alternative observation model adapted to PIV data.

Let us now analyze a result of the anisotropic version on a pair of LSR images issued from radar.

Radar data

We have tested the technique on a pair of radar data given by Meteo France, the french institute for research and operational meteorology. An image is shown in figure FIG. 1.8 (a). As one can observe, the available data do not cover the whole image. Therefore global methods are tricky to use on such images since the conservation assumptions are corrupted in many locations (note that it is however possible to use non-quadratic penalizations to remove outliers [Huber 1981, Delanay 1998, Geman 1992]). The velocity field obtained with the local technique of [Corpetti 2011] using anisotropic uncertainties is shown on FIG. 1.8 **(b)** (one vector out of 20 is shown) and the associated uncertainty on FIG. 1.8 (c). On figure FIG. 1.8 (d) we have plotted the results obtained by the operational tool of Meteo France based on correlation (all vectors are represented). From these images we observe that both velocity fields are similar which indicates that the proposed approach is as consistent as operational tools. In addition, we provide more data (1 vector per km with our technique compared to 1 vector every $32km$ with correlation-based techniques used in the operational tool) and our process also extracts the uncertainty map which reveals interesting properties on FIG. 1.8 (c) (in particular, the estimation is not confident at the border). This experiment proves that the technique performs efficiently on LSR data.

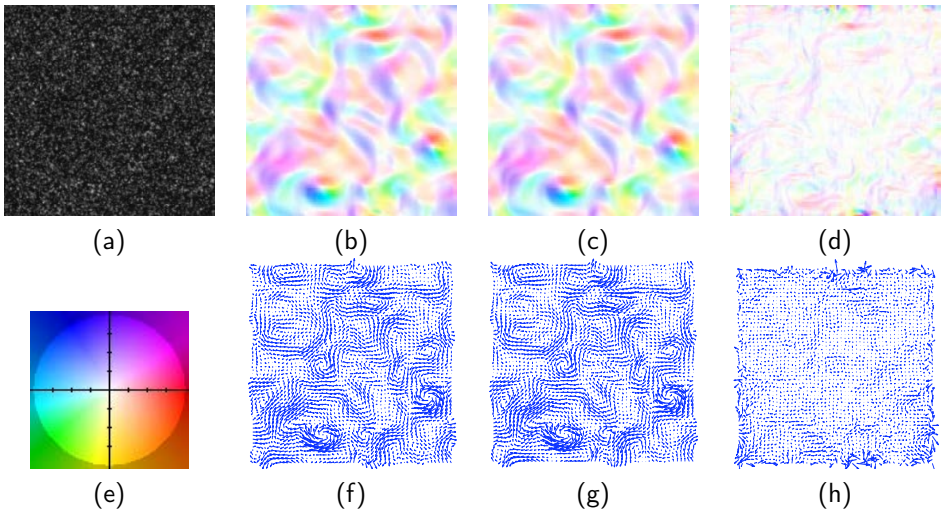

FIGURE 1.6 – **Results on the DNS sequence : Top** (a) : an image of the sequence ; (b) : the estimated flow ; (c) : the real flow ; (d) : the difference flow represented with the coding color in (i) ; **Bottom** (e) : the coding color vor vector flow representation ; (f-g-h) vector representation of the estimated motion field, the ground truth and the difference field ($\times 25$).

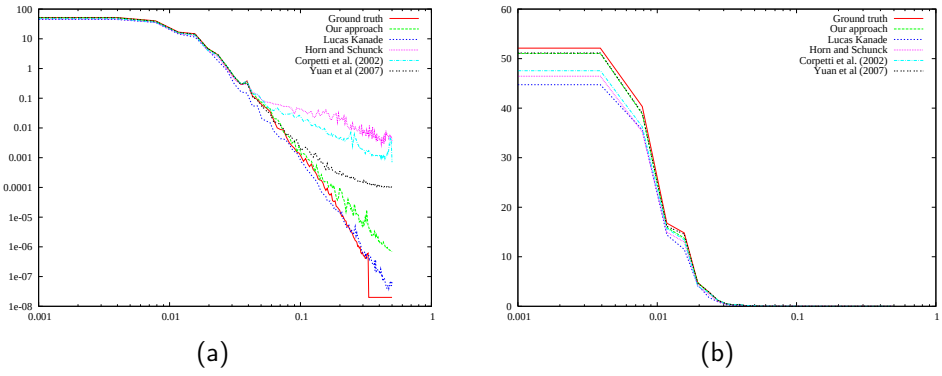

FIGURE 1.7 – **Spectra of the velocity compared with ground truth and several method** (a) : log-log representation (highlights small scales on the right part) and (b) : non log-log representation (highlights large scales on the left part). Color are : Red : ground truth ; Green : our approach (anisotropic version) ; Blue : Lucas-Kanade [Lucas 1981] ; Purple : Horn and Schunck [Horn 1981] ; Cyan : Div-Curl smoothing [Corpetti 2002] and Black : Div-Curl in mimetic discretization [Yuan 2007].

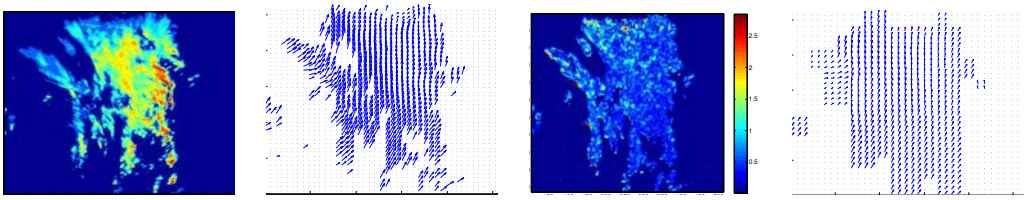

FIGURE 1.8 – **Results on a pair of radar images** (a) : a radar data (b) : our velocity field (one vector out of 20 is plotted) ; (c) : associated uncertainty and (d) : the velocity issued from the meteo france tool (all vectors are plotted).

As our observation terms hold not only for fluid and turbulence, we have applied it on usual images. The results can be seen in [Corpetti 2011].

1.6 Summary

In this chapter we have been focused on frame-to-frame motion estimation techniques. We have presented the main foundations and some contributions for fluid flows, both on observation and smoothing terms. Even if fluid based spatial priors are more adapted, they still rely on *assumptions* but do not on *physical laws*. When a sequence is available, it is then of prime importance to exploit the available dynamical models. This is the scope of the next chapter.

Chapitre 2

Motion estimation from a sequence of images : introduction of dynamical laws

Sommaire

2.1 Overiew

In the previous chapter we have addressed the problem of motion estimation from a pair of images. In this chapter we are interested in image sequences. The computation of the optical flow over a complete sequence remains a difficult problem if one wishes explicitly to maintain a relevant global spatio-temporal coherence. Even if some spatio-temporal estimators have been proposed in previous studies [Black 1991, Brox 2004, Nagel 1990, Weickert 2001b], none of them introduce an explicit dynamic law as a temporal consistency, except the two frames Stockes regularization of [Ruhnau 2007]. As a matter of fact, spatio-temporal regularizers as introduced in [Black 1991, Weickert 2001b] only consider a crude stationary local prior. Moreover, strong artifacts are managed with difficulty. Such approach can not be used to enforce on the whole sequence a solution minimizing an image based discrepancy measure and in the same time that follows a given dynamical model. This kind of tracking process, usually managed using stochastic techniques, is very difficult to design in such application as the variable's state space is of huge dimension (theoretically

infinite) and can not be efficiently handled with usual recursive Bayesian filters such as the particle filter.

In this chapter, we rely on a variational technique which allows us to estimate a sequence of dense motion fields guided by a given dynamical law. To that end, we suggest to exploit recipes related to optimal control theory [Lions 1971, Le Dimet 1986, Talagrand 1997] and variational data assimilation [Le Dimet 1986, Talagrand 1997]. In the same way as Bayesian smoothing, such techniques give a mean to estimate on the basis of noisy and possibly incomplete observations a feature trajectory (a sequence of dense motion fields in our application) respecting a specified evolution law. The associated minimization process is efficiently expressed considering an *adjoint formulation*. The adjoint variable introduced enables to compute the gradient of the cost-function from a forward-backward integration of two coupled evolution models. This efficient procedure authorizes coping with state space of very large dimensions.

The next section briefly introduces the variational assimilation whereas sections 2.3, 2.4 and 2.5 use this framework for several situations (atmospheric flows, pressure data and general video sequences).

2.2 Data assimilation

In this section we present the main principles of variational data assimilation for an imperfect dynamic model. We refer the reader to [Bennett 1992, Le Dimet 1986, Lions 1971, Papadakis 2007a, Talagrand 1987, Talagrand 1997, Vidard 2000] for complete methodological aspects of data assimilation and applications concerning geophysical flows.

Our problem consists in recovering, from an initial condition, a system's state X partially observed and driven by approximately known dynamics. This can be formalized as finding $X(\boldsymbol{x},t)$, for any location $\boldsymbol{x}$ at time $t \in [t_0, t_f]$, that satisfies the system :

$$\frac{\partial X}{\partial t}(\boldsymbol{x},t) + \mathbb{M}(X(\boldsymbol{x},t)) = \nu_m(\boldsymbol{x}), \tag{2.1}$$

$$X(\boldsymbol{x},t_0) = X_0(\boldsymbol{x}) + \nu_n(\boldsymbol{x}), \tag{2.2}$$

$$\boldsymbol{\mathcal{Y}}(\boldsymbol{x},t) = \mathbb{H}(X(\boldsymbol{x},t)) + \nu_o(\boldsymbol{x},t), \tag{2.3}$$

where $\mathbb{M}$ is the non-linear operator relative to the dynamics, X_0 is the initial vector at time t_0 and (ν_n, ν_m) are (unknown) additive control variables relative to noise on the dynamics and the initial condition respectively. In addition, noisy measurements $\boldsymbol{\mathcal{Y}}$ of the unknown state are available through the non-linear operator $\mathbb{H}$ up to ν_o. To estimate the system's state, a common methodology relies on the minimization of the cost function $\mathcal{J}$:

$$\begin{aligned}\mathcal{J}(X) =& \frac{1}{2}\int_{t_0}^{t_f} \|\boldsymbol{\mathcal{Y}} - \mathbb{H}(X(\nu_m,\nu_n))\|^2_{R^{-1}} dt \\ &+ \frac{1}{2}\|X(\boldsymbol{x},t_0) - X_0(\boldsymbol{x})\|^2_{B^{-1}} \\ &+ \frac{1}{2}\int_{t_0}^{t_f} \|\frac{\partial X}{\partial t}(\boldsymbol{x},t) + \mathbb{M}(X(\boldsymbol{x},t))\|^2_{Q^{-1}} dt,\end{aligned} \tag{2.4}$$

where we have introduced the information matrices R, B, Q relative to the covariance of the errors (ν_m, ν_n, ν_o). The Mahalanobis distance that has been used reads, for an information matrix A : $\|X\|_{A^{-1}} = X^T A^{-1} X$. The evaluation of X can be done by canceling the gradient $\delta\mathcal{J}_X(\theta) = \lim_{\beta\to 0} \frac{J(X+\beta\theta)-J(X)}{\beta}$ of (2.4). Unfortunately, the estimation of such gradient is in practice unfeasible for a large system's state since it would be necessary to integrate the dynamical model along all possible perturbations of the components of X. This is

computationally impossible with actual hardwares when one deals with a complete sequence of images. One way to cope with this difficulty is to write *an adjoint formulation* of the problem. To that end, the *adjoint variables* $\boldsymbol{\lambda}$ that express the errors of the dynamic model are introduced as :

$$\boldsymbol{\lambda} = Q^{-1}\left(\frac{\partial X}{\partial t} + \mathbb{M}(X)\right). \tag{2.5}$$

Denoting

- $\left(\frac{\partial \mathbb{M}}{\partial \widetilde{X}}\right)$ and $\left(\frac{\partial \mathbb{H}}{\partial \widetilde{X}}\right)$ the *linear tangent operators* of $\mathbb{M}$ and $\mathbb{H}$ respectively. The linear tangent of an operator $\mathbb{A}$ is the directional derivative of the operator (the Gâteaux derivative) :

$$\left(\frac{\partial \mathbb{A}}{\partial \widetilde{X}}\right)(dX) = \lim_{\beta \to 0} \frac{\mathbb{A}(\widetilde{X} + \beta dX) - \mathbb{A}(\widetilde{X})}{\beta}, \tag{2.6}$$

- $(\partial_X \mathbb{M})^*$ and $(\partial_X \mathbb{H})^*$ their *adjoint operators*. The adjoint $\mathbb{A}^*$ of a linear operator $\mathbb{A}$ on a space $\mathcal{D}$ is such as :

$$\forall x_1, x_2 \in \mathcal{D}, < \mathbb{A}x_1, x_2 > = < x_1, \mathbb{A}^* x_2 > . \tag{2.7}$$

It can be shown that canceling the gradient $\delta \mathcal{J}_X(\theta)$ with respect to the adjoint variables $\boldsymbol{\lambda}$ leads to a retrograde integration of an adjoint evolution model that takes into account the observations. Once the adjoint variables $\boldsymbol{\lambda}$ are estimated, one can recover the system state X using relation (2.5). Finally, when dealing with non-linear models, recovering X leads to the following incremental algorithm [Bennett 1992] :

1. Starting from $\tilde{X}(\boldsymbol{x}, t_0) = X_0(\boldsymbol{x})$, perform a *forward* integration : $\frac{\partial \tilde{X}}{\partial t} + \mathbb{M}(\tilde{X}) = 0$
2. $\tilde{X}(\boldsymbol{x}, t)$ being available, **compute the adjoint variables** $\boldsymbol{\lambda}(\boldsymbol{x}, t)$ with the *backward* equation :

$$\begin{aligned} &\boldsymbol{\lambda}(t_f) = 0 \ ; \\ &-\frac{\partial \boldsymbol{\lambda}}{\partial t}(t) + (\partial_X \mathbb{M})^* \, \boldsymbol{\lambda}(t) = (\partial_X \mathbb{H})^* \, R^{-1}(\boldsymbol{\mathcal{Y}} - \mathbb{H}(\tilde{X}))(t) \end{aligned} \tag{2.8}$$

3. **Update the initial condition** : $dX(t_0) = B\boldsymbol{\lambda}(t_0)$;
4. $\boldsymbol{\lambda}$ being available, **compute the state space** $dX(t)$ from $dX(t_0)$ with the *forward* integration

$$\frac{\partial dX}{\partial t}(t) + \left(\frac{\partial \mathbb{M}}{\partial \tilde{X}}\right) dX(t) = Q\boldsymbol{\lambda}(t) \tag{2.9}$$

5. **Update** : $\tilde{X} = \tilde{X} + dX$
6. **Loop** to step (2) until convergence

Intuitively, the adjoint variables $\boldsymbol{\lambda}$ contain information about the discrepancy between the observations and the dynamic model. They are computed from a current solution $\tilde{X}$ with the backward integration (2.8) that encompasses both the observations and the dynamic operators. This deviation indicator between the observations and the model is then used to refine the initial condition (step (3)) and to recover the system state through an imperfect dynamic model where errors are $Q\boldsymbol{\lambda}$ (step (4)). It should be noted that if the dynamic is perfect, the associated error covariance Q is zero and the algorithm only refines the initial condition. However from an image analysis point of view, a perfect modeling is difficult to obtain since the different models on which we rely are usually inaccurate due, for instance, to 3D-2D projections, varying lighting conditions, completely unknown boundary conditions at the image boarders, *etc.*

This framework is then an appealing solution for large system states, as the ones we have for the extraction of a complete sequence of dense motion fields. To design an assimilation process, we need to define :

1. The system state ;
2. The dynamical model (and its adjoint) ;
3. The observation operator (and its adjoint) ;
4. The error covariance matrices.

Usually, in geosciences applications like meteorology, the quantity of interest is directly observed and the dynamical models are perfect. However when one deals with images, because of the reasons mentioned above, adapted operators (observation and dynamic) as well as error covariance matrices have to be set up. In the next two sections we present two motion estimators for fluid flows based on the variational assimilation framework.

2.3 Motion estimation for atmospheric flows

2.3.1 System state

Following the Helmholtz decomposition (see figure FIG. 1.1), any motion can be represented with its vorticity ζ, its divergence D and its harmonic component $\boldsymbol{v}_{har}$. This latter component is in practice estimated once using a Horn & Schunck estimator with a strong balance of the smoothing term in order to extract only the div-curl free part of the flow. Therefore only (ζ, D) are needed and the system state is $X = [\zeta, D]^T$. The knowledge of X enables to recover the motion field through Biot-Savart law :

$$\boldsymbol{v} = \nabla^{\perp} G * \zeta + \nabla G * D = \mathbb{H}_G(X), \tag{2.10}$$

where we have introduced the operator $\mathbb{H}_G : [\zeta, D]^T \rightarrow \boldsymbol{v} = [u, v]^T$ such as $\mathbb{H}_G(X) = \nabla^{\perp} G * \zeta + \nabla G * D$, $\nabla^{\perp} = (\partial/\partial y, -\partial/\partial x)^T$ and G denotes the Green kernel ($G = \frac{1}{2\pi} \ln(|x|)$) associated to the Laplacian operator. This computation can be very efficiently done in the Fourier domain [Corpetti 2003].

2.3.2 Dynamical model

Vorticity model

Following a mean incompressibility assumption (divergence is weak and the motion is mainly influenced by horizontal scales), we rely on the vorticity velocity formulation of the Navier-Stokes equation. This model reads :

$$\frac{\partial \zeta}{\partial t} + \boldsymbol{v} \cdot \nabla \zeta - \nu \Delta \zeta = 0 \tag{2.11}$$

where ν is a dissipation coefficient. For vorticity based large eddy simulation formulations, we may either rely on

1. the Smagorinsky model : $\nu = (C\delta_x)^2 \sqrt{2(u_x^2 + v_y^2 + (u_y + v_x)^2)}$ where C is the Smagorinsky coefficient (which is usually fixed to 0.17) and δ_x the grid size ;
2. enstrophy-based sub-grid models [Mansour 1978]. This sub-grid dissipation model is based on Taylor's vorticity transfer and dissipation by small scales theory [Taylor 1932] and reads $\nu = (C\delta_x)^2 |\zeta|$.

In practice we use the second formula.

Divergence model

Since at large scales, the divergence can be considered weak almost everywhere, we will rely on an approximate evolution law. We assume that the divergence is advected by the flow and a noise variable that encodes the uncertainty on the model. More precisely we assume that the divergence map is a function of a stochastic process representing a particle position and is driven by the following stochastic differential equation :

$$d\boldsymbol{X}_t = \boldsymbol{v}(\boldsymbol{X}_t)dt + \sqrt{2\nu}d\mathbf{B}_t. \tag{2.12}$$

This equation states that the particle position is known only up to an uncertainty that grows linearly with time. As in the previous chapter, $\mathbf{B}_t$ denotes a standard Brownian motion of $\mathbb{R}^2$. The process $\boldsymbol{X}_t$ starts at point $\boldsymbol{X}_0$. It can be shown through the Îto formula and Kolmogorov's forward equation, that the expectation $\xi(t, \boldsymbol{X}) = \mathbb{E}[\mathrm{div}\boldsymbol{v}(\boldsymbol{X}_t)]$ at time t of such divergence follows an advection diffusion equation [Oksendal 1998] :

$$\begin{aligned} &\xi_t + \boldsymbol{v}\cdot\nabla\xi + \xi\mathrm{div}(\boldsymbol{v}) - \nu\Delta\xi = 0, \\ &\xi(0, \boldsymbol{X}_0) = \mathrm{div}\boldsymbol{v}(\boldsymbol{X}_0). \end{aligned} \tag{2.13}$$

Assuming that for large scales the divergence of the flow is given by its expectation ($D \approx \xi$), one writes the simplified divergence model as :

$$\frac{\partial D}{\partial t} + \boldsymbol{v}\cdot\nabla D + D^2 = \nu\Delta D \tag{2.14}$$

In this model we assume that D is weak and is similar to the divergence expectation. Following the relation (2.14), the expectation of the divergence value is advected by the flow and dissipates due to a subgrid isotropic uncertainty. This hypothesis is quite natural in large scale modeling.

Total model

Following equations (2.11-2.14), the dynamic system reads, with $X = [\zeta, D]^T$:

$$\frac{\partial}{\partial t}\begin{bmatrix} \zeta \\ D \end{bmatrix} + \underbrace{\begin{bmatrix} \boldsymbol{v}\cdot\nabla\zeta - \nu\Delta\zeta \\ \boldsymbol{v}\cdot\nabla D + D^2 - \nu\Delta D \end{bmatrix}}_{\mathbb{M}(X)} = \nu_m \tag{2.15}$$

Tangent-linear, adjoint evolution model & implementation

This model is non-linear and its linear-tangent operator is, with $X = \widetilde{X} + dX$ is :

$$\begin{aligned} \left(\frac{\partial\mathbb{M}}{\partial\widetilde{X}}\right)(dX) &= \begin{bmatrix} \mathbb{H}_G(\widetilde{X})\cdot\nabla d\zeta + \mathbb{H}_G(dX)\cdot\nabla\widetilde{\zeta} - \nu\Delta d\zeta \\ \mathbb{H}_G(\widetilde{X})\cdot\nabla dD + \mathbb{H}_G(dX)\cdot\nabla\widetilde{D} + 2\widetilde{D}dD - \nu\Delta dD \end{bmatrix} \\ &= \begin{bmatrix} \mathbb{H}_G(\widetilde{X})\cdot\nabla + \nabla\widetilde{\zeta}\cdot\mathbb{H}_G - \nu\Delta \\ \mathbb{H}_G(\widetilde{X})\cdot\nabla + \nabla\widetilde{D}\cdot\mathbb{H}_G + 2\widetilde{D} - \nu\Delta \end{bmatrix} dX \end{aligned} \tag{2.16}$$

The discretization of this model ought to be cautiously done. The advective terms of the form $\boldsymbol{w}\cdot\nabla dX$ (where $\boldsymbol{w}$ is a vector) must be in particular treated specifically since they are likely to introduce many numerical errors. In order to achieve an accurate and stable discretization of the advection terms one must use conservative numerical schemes. Such schemes are designed to exactly respect the conservation law within the cell by integrating the flux value at cell boundaries. Total Variation Diminishing (TVD) schemes (which are

monotonicity preserving flux) prevent from an increase of oscillations over time and enable to transport shocks. In this work, we used semidiscrete central schemes [Kurganov 2000a, Kurganov 2000b] associated to a second order accurate methods [Levy 1997] based on a *min-mod limiter* for the vorticity reconstruction. The time integration is realized with a third-order Runge Kutta scheme, which also respect the TVD property [Giles 2000].

The relation (2.8) requires the adjoint operator $(\partial_X \mathbb{M})^*$ of the linear tangent $\left(\frac{\partial \mathbb{M}}{\partial \widetilde{X}}\right)$ defined in (2.16). Its expression is not trivial as this operator is expressed through a convolution product. It can be demonstrated in the Fourier space (see [Papadakis 2008] for details) that the adjoint of $\mathbb{H}_G$ is $-\mathbb{H}_G$. As for other terms, once the direct operators (advection, diffusion) have been discretized, the corresponding adjoint is simply obtained using the transpose of the direct models. More details about the construction of adjoint models can be found in [Talagrand 1987].

2.3.3 Observation operator

For atmospheric flows we can either start from the OFCE (if the divergence is weak) or from the mass conservation law :

$$\frac{\partial I}{\partial t} + \nabla I \cdot \boldsymbol{v} + I \mathrm{div} \boldsymbol{v} = 0. \tag{2.17}$$

The OFCE corresponds to the previous relation without the term $I\mathrm{div}\boldsymbol{v}$. Noting that $\boldsymbol{v} = \mathbb{H}_G(X)$ and $\mathrm{div}\boldsymbol{v} = D$, the observation system $\boldsymbol{\mathcal{Y}} = \mathbb{H}(X)$ is constructed from the available images with :

$$\boldsymbol{\mathcal{Y}} = \frac{\partial I}{\partial t} \text{ and } \mathbb{H}(X) = \left(-\nabla I^T \mathbb{H}_G - [0, I]\right) X \tag{2.18}$$

The adjoint $(\partial_X \mathbb{H})^*$ of $\mathbb{H}$ is

$$(\partial_X \mathbb{H})^* = \mathbb{H}_G \nabla I - [0, I]^T \tag{2.19}$$

It should be noted that this observation operator is submitted to the aperture problem. Difficult situations, in particular in homogeneous areas, are then not exploitable and have to be addressed in the error covariance matrix R. If such situations are likely to be numerous, it is also possible to assume, like the Lucas & Kanade technique, that the unknown velocity at location $\boldsymbol{x}$ is constant within some local neighborhood and to convolve relations (2.18) and (2.19) with a Gaussian kernel.

2.3.4 Error covariance matrices and initialization issues

Observations

We have proposed two different solutions for the error covariance matrix R related to the observations. The first one relies on the magnitude of the gradient :

$$R(\boldsymbol{x}) = R_{min} + (R_{max} - R_{min}) \exp - \frac{\|\nabla I(\boldsymbol{x})\|^2}{\sigma_{obs}^2} \tag{2.20}$$

where R_{min}, R_{min} and σ_{obs} are fixed and depend on the data. The uncertainty on the observation operator, related to the value of $R(\boldsymbol{x})$, is then maximal (resp. minimal) when $\|\nabla I(\mathbf{x})\|$ is low (resp. high), which is consistent with observations of the previous chapter stating that the quality of the estimation of the motion is strongly related to the importance of $\|\nabla I(\boldsymbol{x})\|$.

The second solution can be applied if one uses external motion fields or advance motion estimation techniques. In this case the estimation is less related to the magnitude of the gradient and one can define R^{-1} as :

$$R^{-1}(\boldsymbol{x}) = R_{max} \exp - \frac{[\boldsymbol{\mathcal{Y}} - \mathbb{H}(X)]^2}{\sigma^2_{obs}} \tag{2.21}$$

As shown in [Corpetti 2009], this penalization amounts to considering a robust norm on the first term of the cost-function in (2.4). Such a robust function allows the discarding of points having large "residual" values of the observation error $[\boldsymbol{\mathcal{Y}} - \mathbb{H}(X)]$ (called *outliers* in the Robust Statistics literature [Huber 1981, Geman 1992, Delanay 1998]). In our application, it enables to properly deal with corrupted areas that do not fit our data model exactly.

Initial conditions

We have chosen to represent the covariance matrix B of the initial condition as $B = Id - \exp\left\{-|\boldsymbol{\mathcal{Y}}(t_0) - \boldsymbol{\mathcal{Y}}(X_0)|/\sigma^2_B\right\}$ where σ_B is a parameter to fix. Here again, it is related to the adequacy of the current state at time t_0 and the initial condition.

Dynamic model

The covariance matrix Q has been fixed to a constant diagonal matrix as we have no prior on the spatio-temporal adequacy of the dynamical model.

2.3.5 Some results on meteorological sequences

We applied this technique on two infra-red meteorological sequences showing several cyclones. The first sequence (top of figure FIG. 2.1) was acquired on October, 9^{th} 2005 and corresponds to the "Vince" cyclone. We present the estimated motion fields superimposed to their corresponding image for three frames of the sequence (first line). The second line presents the corresponding vorticity and the third line the vorticity obtained with the dedicated fluid motion estimator we proposed in [Corpetti 2002]. As many location of the image plane are disturbed by non-valid data, it can be observed that the dedicated estimator presents some temporal inconsistencies and discontinuities in terms of vorticity. These noisy values are completely removed by the technique presented which provides smooth and coherent vorticity maps. More consistent evaluations with quantitative experiments can be found in [Papadakis 2007b]. The second sequence at the bottom of figure FIG. 2.1 was acquired in 1998 and represents a depression in the south of Europe. We have blurred several input data, as shown in FIG. 2.1 (j–m). The images in FIG. 2.1 (n–q) represent the motions obtained with the presented assimilation technique whereas the last line (FIG. 2.1 (r–u)) exhibits the corresponding motion fields without any temporal consistency (estimator in [Corpetti 2002]). One can observe that our technique significantly improves the consistency of the results. Let us now turn to experiments on pressure image data.

2.4 Pressure image assimilation for various atmospheric layers

We have addressed the problem of estimating motion fields from pressure data at various atmospheric depths for a whole image sequence. Such data correspond to pressure differences $h^k(\boldsymbol{x}) = p^k(\boldsymbol{x}) - \overline{p^k}$ of a given pressure $p^k(\boldsymbol{x})$ and its mean value $\overline{p^k}$ over a layer k of the

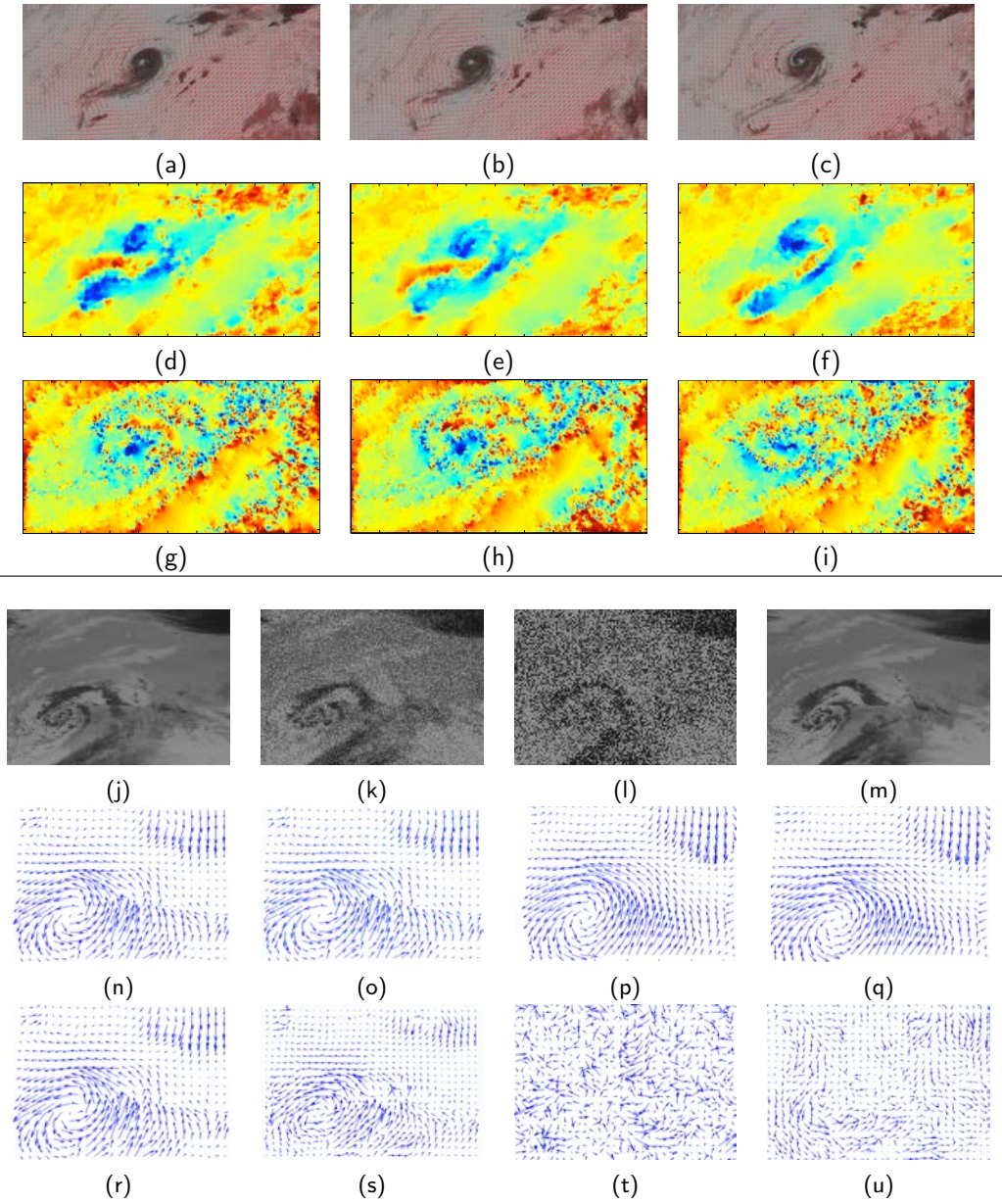

FIGURE 2.1 – **Experimental results on real Meteosat data** TOP : Vince sequence : (a–c) : three images and the corresponding motion field ; (d–f) : the estimated vorticity ; (g–i) : the vorticity obtained with a fluid dedicated estimator without any temporal consistency. BOTTOM : a depression sequence : (j–m) 4 images of the sequence where some of them are blurred ; (n–q) motion fields with the assimilation process ; (r–u) motion fields without any temporal consistency

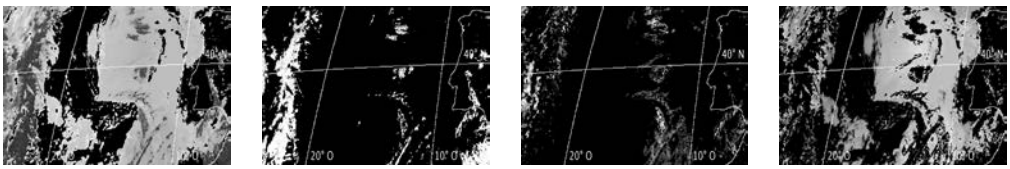

(a) (b) (c) (d)

FIGURE 2.2 – **Pressure image observations** issued from METEOSAT (Northern Atlantic Ocean on June 2004 from 13h30 until 15H45 UTC). (a) : cloud top pressure image ; (b) : pressure difference of the higher layer ; (c) : pressure difference of the intermediate layer ; (d) : pressure difference of the lower layer. Black regions correspond to missing observations and white lines represent coastal contours, meridians and parallels (every 10^o).

atmosphere. They are routinely provided by the EUMETSAT consortium [1] and the figure FIG. 2.2 gives an illustration. As one can observe, most layers exhibit important areas of missing data and it is obvious that a frame-to-frame motion estimator would lead to inconsistent values.

Based on a vertical decomposition of the atmosphere, we have proposed two dynamically consistent atmospheric motion estimators relying on slightly different multi-layer dynamic models :

1. The first one assimilates the data h^k and the velocity $\boldsymbol{v}^k$ at large scales under a perfect dynamical model where only h^k is observed. Therefore, the velocity is extracted uniquely on the basis of pressure difference observations and no motion estimation equation is needed. As we will see, this technique works efficiently but requires a perfect modeling and extracts only the large scale structures ;
2. The second one relaxes the perfect dynamical model assumption and estimates the vorticity and the divergence of the different flows under a simplified shallow-water vorticity-divergence system.

These estimators are roughly presented in the two next sections and more details can be found in [Corpetti 2008a, Corpetti 2008b, Corpetti 2009]. They are based on the shallow-water approximation (horizontal motion much greater than vertical motion under the assumption of incompressibility) [Saint-Venant (De) 1871] where the filtered horizontal momentum equations for atmospheric motion read :

$$\left\{ \begin{array}{rcl} \frac{d\tilde{u}}{dt} + \frac{\tilde{p}_x}{\rho_0} - \tilde{v} f^\phi & = & \nu_\mathcal{T} \Delta \tilde{u} \\ \frac{d\tilde{v}}{dt} + \frac{\tilde{p}_y}{\rho_0} + \tilde{u} f^\phi & = & \nu_\mathcal{T} \Delta \tilde{v} \end{array} \right. \tag{2.22}$$

where

- K_{δ_x} is a gaussian kernel of standard deviation δ_x ;
- $\tilde{p} = K_{\delta_x} * p$ is the filtered pressure p at scale δ_x ;
- $\tilde{\mathbf{v}} = (\tilde{u}, \tilde{v})^T = K_{\delta_x} * (u, v)^T$ is the filtered velocity field at scale δ_x

with

- ρ_0 : local mean density
- f^ϕ : Coriolis factor depending on latitude ϕ
- $\nu_\mathcal{T}$: turbulent viscosity produced at sub-grid scales [Frisch 1995]. In practice we use the same as the previous section.

Let us now describe how we proposed two assimilation systems based on the model in (2.22).

1. http://www.eumetsat.int/, consortium in charge of the management of Meteosat data

2.4.1 Perfect dynamical model

The model in (2.22) is valid for the upper range of mesoscale analysis in a layered atmosphere. Considering horizontal scales of order of 100 km, combined with layer depths of order of 1 km, makes the shallow-water approximation relevant. Therefore, in order to obtain a valid dynamical model on a pixel grid of resolution δ_p in kilometers, we can filter the dynamical equations with a Gaussian kernel function K_{δ_x} of standard deviation equal to $\delta_x = 100\delta_p^{-1}$, where δ_p denote the image pixel resolution in kilometers.

After several manipulations that consist in :

- expanding total derivatives in isobaric coordinates ;
- using the fact that we have incompressible flows ;
- performing a vertical integration of the shallow-water equations and using the continuity equation ;

one obtain independent shallow-water equation systems for atmospheric layers $k \in [1, K]$ that read :

$$\left\{ \begin{array}{l} \frac{\partial \tilde{h}^k}{\partial t} + \mathrm{div}(\tilde{\mathbf{q}}^k) = 0 \\ \frac{\partial (\tilde{\mathbf{q}}^k)}{\partial t} + \mathrm{div}(\frac{1}{\tilde{h}^k}\tilde{\mathbf{q}}^k \otimes \tilde{\mathbf{q}}^k) + \frac{1}{2\overline{\rho}^k}\nabla_{xy}(\tilde{h}^k)^2 + \begin{bmatrix} 0 & -1 \\ 1 & 0 \end{bmatrix} f^\phi \tilde{\mathbf{q}}^k = \nu_{\mathcal{T}}^k \Delta(\tilde{\mathbf{q}}^k), \end{array} \right. \tag{2.23}$$

with :

- $\tilde{\mathbf{q}}^k = \tilde{h}^k \tilde{\mathbf{v}}^k$ and
- $\mathrm{div}(\frac{1}{\tilde{h}^k}\tilde{\mathbf{q}}^k \otimes \tilde{\mathbf{q}}^k) = \begin{bmatrix} \frac{\partial(\tilde{h}^k(\tilde{u}^k)^2)}{\partial x} + \frac{\partial(\tilde{h}^k \tilde{u}^k \tilde{v}^k)}{\partial y} \\ \frac{\partial(\tilde{h}^k \tilde{u}^k \tilde{v}^k)}{\partial x} + \frac{\partial(\tilde{h}^k(\tilde{v}^k)^2)}{\partial y} \end{bmatrix}$

The first relation of (2.23) is simply the mass conservation law whereas the second one is an advection-diffusion process where vertical interactions and Coriolis effects are taken into account. The k index expresses a quantity related to the k^{th} layer.

On the basis of this system, we have developed an assimilation process where the system state is $X = [\tilde{h}^k, \tilde{\mathbf{q}}^k]^T$ and the observation are simply provided by the data of pressure differences $\tilde{h}^k_{obs}$:

$$\left\{ \begin{array}{ll} \mathcal{Y} & = \tilde{h}^k_{obs} = K_{\delta_x} * h^k_{obs} \\ \mathbb{H} & = [I_d, 0] \end{array} \right. . \tag{2.24}$$

As one can see, no motion observation equation is introduced. The overall system (associated linear tangent operator, adjoints, covariances, ...) is described in details in [Corpetti 2008a, Corpetti 2009]. The figure Fig. 2.3 illustrates some results for the lowest layer of the atmosphere available in our data. As one can observe, results are interesting since we recovered consistent large scale data related to $\tilde{h}^k_{obs}$. In addition, let us outline that the velocity fields have been estimated without any motion observation equation but they only rely on corrections with respect to the dynamical model. This is, to our opinion, a very relevant way to recover motion fields. Qualitative and quantitative results can be found in [Corpetti 2008a, Corpetti 2009]. Despite a good accuracy, only the large scales structures can be extracted since we assumed a perfect dynamical model that only manage large scales. The overall equations that include fine scales without any simplifications yield indeed a too complex system with several unknown quantities that can not be used for the assimilation. In order to relax the layering assumption, we describe in the next section the evolution of the filtered state variables using a simplified version of the previously introduced shallow-water equations and perform assimilation using an imperfect modeling scheme. As will be illustrated, this authorizes the extraction of finer structures.

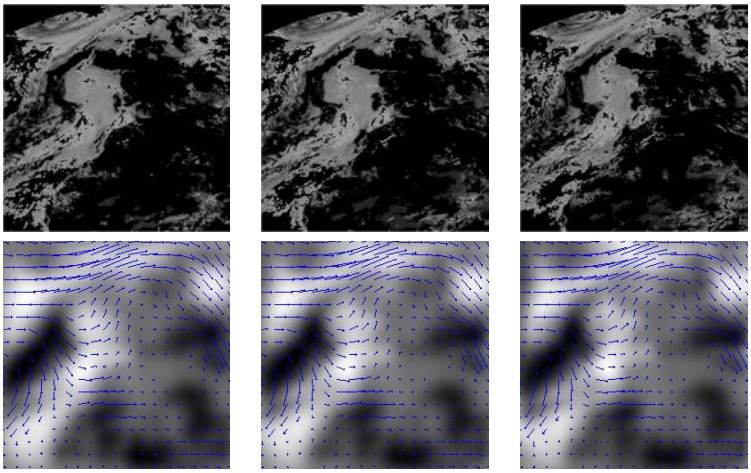

FIGURE 2.3 – **Horizontal wind fields and large scales pressure data recovered by assimilation with a perfect model.** First line : input pressure data for the lowest layer available ; second line : recovered large scales pressure and associated wind fields.

2.4.2 Imperfect dynamical model

In order to overcome the limitations mentioned above, we have described the evolution of the filtered state variables from a simplified version of the previously introduced shallow-water equations and performed assimilation using an imperfect modeling scheme. After several manipulations that consist in :

- rewriting the system in (2.23) in terms of vorticity ζ^k (this has the advantage to provide an independency from pressure) ;
- assuming that the divergence model in (2.14), quite natural for large scale modeling, holds for the divergence D^k at each layer k,

one gets the system :

$$\left\{ \begin{array}{l} \frac{\partial \zeta^k}{\partial t} + \mathbf{v}^k \cdot \boldsymbol{\nabla} \zeta^k + (\zeta^k + f^\phi) D^k - \nu_{\mathcal{T}} \Delta \zeta^k \approx 0 \\ \frac{\partial D^k}{\partial t} + \underbrace{\mathbf{v}^k \cdot \boldsymbol{\nabla} D^k + (D^k)^2 - \nu_{\mathcal{T}} \Delta D^k}_{\text{dynamic model} \quad \mathbb{M}(\zeta^k, D^k)} \approx 0 \end{array} \right. . \tag{2.25}$$

for any velocity field $X^k = [\zeta^k, D^k]$ at each layer k of the atmosphere. Concerning the vorticity equation, this model is an advection-diffusion influenced by the Coriolis force and the vertical motions (term $(\zeta^k + f^\phi)D^k$). The observation model used here is the same than the one proposed in (2.18) and is based on the mass conservation law that is valid for pressure data. The overall system (associated linear tangent operator, adjoints, covariances matrices and implementation issues) is described in details in [Corpetti 2008a, Corpetti 2009]. The figure FIG. 2.4 illustrates some results for the images of the first line of figure FIG. 2.3 (lowest layer of the atmosphere). The motion fields as well as their associated vorticity and divergence are depicted and compared with the ones extracted by a frame-to-frame motion estimator adapted to layers and described in [Héas 2007]. From these results, it should de noted that the motion of some small cloud structures have been well characterized by this assimilation scheme. This is due to the fact that the shallow-water assumption is not assumed to be strictly respected everywhere. Thus, small scale information from the

image observations may locally generate a motion field which significantly departs from the shallow-water solution. This constitutes a benefit of our approach since our preliminary experiments of the previous section and described in details in [Corpetti 2008a] have shown that the motions of small structures can not be extracted from an assimilation scheme combining a primitive shallow-water model (2.23) and pressure image measurements. It can be observed, from a visual comparison between the vorticity-divergence components estimated by [Héas 2007] and by the proposed assimilation system, that both fields are similar. Time-persistent large structures of the flow are accurately estimated by both methods while noise and time-inconsistent structures have been removed only with the assimilation approach.

Let us now briefly describe a more generic time consistent estimator for general images.

2.5 Other application : rigid motion estimation

Although the main application concerns the analysis of flows in remote sensing data, such variational assimilation framework can also be applied for generic images. This is the scope of this section where we present a time consistent motion estimation technique for usual video data.

2.5.1 System state and dynamic model

As there is no reason to be based on the divergence and the vorticity for usual videos involving rigid objects, the system state reads $X = \boldsymbol{v} = [u, v]^T$. As for the evolution model, no universal physical law can be stated for general videos showing moving objects of different nature. It is therefore difficult to propose a generic formulation that describes accurately the evolution of the velocity. However, one can rationally assume over a short range of time that the velocity is transported by itself up to a Gaussian discretization error. Using stochastic rules introduced in the previous chapter, it can be shown that this yields the following dynamical model :

$$\frac{d\boldsymbol{v}}{dt} = \frac{\partial \boldsymbol{v}}{\partial t} + \boldsymbol{\nabla v} \cdot \boldsymbol{v} = \nu \Delta \boldsymbol{v} \tag{2.26}$$

where ν is to be fixed (but could be considered as a model's parameter to assimilate). The operator $\mathbb{M}$ is then :

$$\mathbb{M}(X) = X \cdot \boldsymbol{\nabla} X - \nu \Delta X. \tag{2.27}$$

2.5.2 Observation system

As the relation in (2.27) is rather a prior knowledge than a pure dynamic model, we prefer to apply a more suitable observation operator based on the optical flow constraint equation accompanied with a first order robust smoothing. The motion field $\boldsymbol{v}$ to extract may be formulated as :

$$\begin{aligned} \boldsymbol{v}(\boldsymbol{x}, t) \approx \min_{\boldsymbol{v}(\boldsymbol{x},t)} & \int_\Omega f_1\Big(\left[\boldsymbol{\nabla} I(\boldsymbol{x}, t) \cdot \boldsymbol{v}(\boldsymbol{x}, t) + I_t(\boldsymbol{x}, t)\right]^2 \Big) \\ & + \alpha \int_\Omega f_2(|\boldsymbol{\nabla} u|^2) + f_2(|\boldsymbol{\nabla} v|^2), \end{aligned} \tag{2.28}$$

where Ω is the image plane, α is a smoothing positive parameter and f_1 and f_2 are two robust penalty functions such that $f(\sqrt{y^2})$ is concave. A weighted quadratic formulation

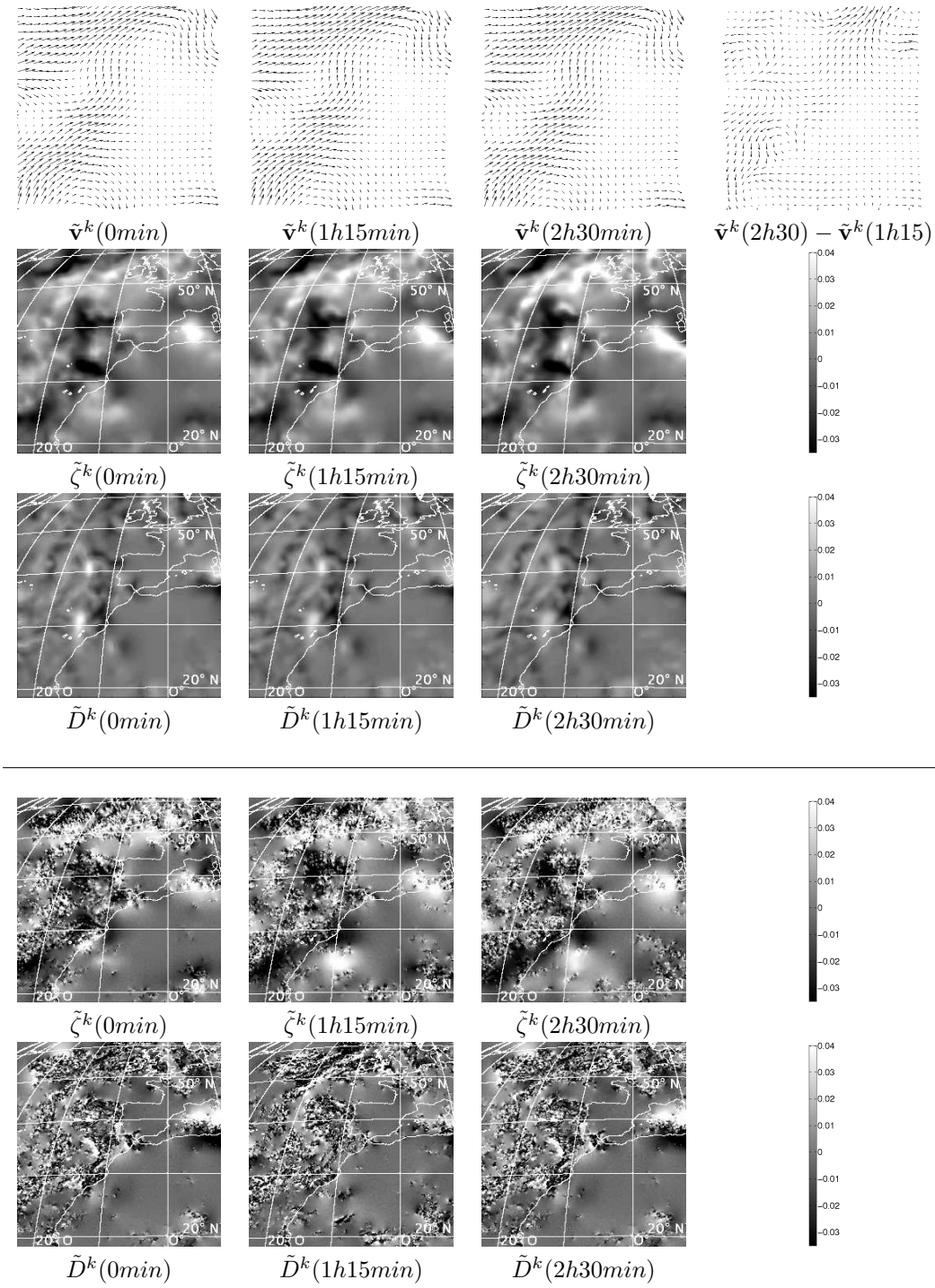

FIGURE 2.4 – **Comparison of results from assimilation (top) and a frame-to-frame technique (bottom)** for the lower layer at $t = 0min$, $t = 1h15min$ and $t = 2h30min$ respectively. First line : three assimilated motion fields and the difference $\tilde{\mathbf{v}}^k(2h30) - \tilde{\mathbf{v}}^k(1h15)$ that illustrates the temporal changes ; second and third lines : corresponding vorticity and divergence ; fourth and fifth lines : corresponding vorticity and divergence estimated with [Héas 2007]. One can conclude that both estimations are in accordance but the one from the assimilation has a better temporal consistency.

of these cost functions can then be obtained [Huber 1981, Delanay 1998, Geman 1992] and one gets the following system :

$$\begin{aligned}\boldsymbol{v}(\boldsymbol{x},t) \approx \min_{\boldsymbol{v},\delta_o,\delta_u,\delta_v} \int_\Omega \delta_o \left[\boldsymbol{\nabla} I(\boldsymbol{x},t)\cdot \boldsymbol{v}(\boldsymbol{x},t) + I_t(\boldsymbol{x},t)\right]^2 \\ + \phi(\delta_o) + \alpha \int_\Omega \delta_u(|\boldsymbol{\nabla} u|)^2 + \delta_v(|\boldsymbol{\nabla} v|)^2 + \phi(\delta_u) + \phi(\delta_v),\end{aligned} \tag{2.29}$$

where the minimization w.r.t the additional *outliers* variables ($\delta_\bullet$) is given explicitly through the derivative of function f : $\hat{\delta}_\bullet(y) = f'_\bullet(\sqrt{y^2})$ (see [Holland 1977] for more details). The Euler-Lagrange equations of the previous functional may be written as the following system of coupled equations :

$$\begin{aligned}&\delta_o \boldsymbol{\nabla} I(\boldsymbol{x},t)\left(\boldsymbol{\nabla} I(\boldsymbol{x},t)^T \boldsymbol{v}(\boldsymbol{x},t) + I_t(\boldsymbol{x},t)\right) - \alpha\delta_u \Delta\boldsymbol{\nabla} u - \alpha\delta_v \Delta\boldsymbol{\nabla} v = 0 \text{ and} \\ &\delta_\bullet(x) = f'_\bullet(\sqrt{x^2}).\end{aligned} \tag{2.30}$$

The observation system for our tracking problem is thus defined as (with $\delta_\bullet(x) = f'_\bullet(\sqrt{x^2})$) :

$$\begin{aligned}\mathbb{H}(X(t),t) &= \left[\delta_o \boldsymbol{\nabla} I(\boldsymbol{x},t)\boldsymbol{\nabla} I(\boldsymbol{x},t)^T - \alpha \begin{pmatrix}\delta_u\Delta & 0\\ 0 & \delta_v\Delta\end{pmatrix}\right] X(t) \\ \boldsymbol{\mathcal{Y}} &= -\delta_o \boldsymbol{\nabla} I(\boldsymbol{x},t) I_t(\boldsymbol{x},t)\end{aligned}$$

Given the weights values (which are obtained explicitly for a value of the velocity and the corresponding robust function argument) the operator $\mathbb{H}$ is linear w.r.t. the state function $\boldsymbol{v}$. All implementation details of this estimator can be found in [Papadakis 2007b].

2.5.3 Some results

To assess the benefit of the temporal model, we have blurred 3 images a sequence representing the motion of a car as depicted in figure FIG. 2.5(b–d). This kind of artifacts may appear when one wants to restore old videos for instance. The figures in FIG. 2.5 (e–h) represent 4 motion fields obtained with our approach whereas figures 2.5 (i–l) show the corresponding motion fields obtained with a robust motion estimator [Mémin 1998]. Thanks to the optimal control process, the motion fields recovered are not affected by the strong artifacts introduced. This kind of results might be interesting for applications in the field of video coding and/or restoration. As for the computation time, this process was two-times faster than the successive estimations of dense motion fields with the same observation operator. Such an approach could be used also to estimate motion of temporarily occluded objects in video, and as a consequence constitutes an important basic ingredient for video object removing in video post-processing. To assess quantitatively the benefit of such approach, we have processed the Yosemite sequence with our technique. One image and three estimated motion fields can be seen in FIG. 2.6. In the table 2.1 we have depicted the average angular errors obtained with the same observation operator without and with a temporal consistency. From these values it is obvious that the assimilation improves the quality of the results.

2.6 Summary

In this chapter a framework allowing to estimate and track dense motion fields with a temporal consistency has been introduced. The approach is related to optimal control theory. It authorizes through noisy and incomplete observations to estimate a sequence of

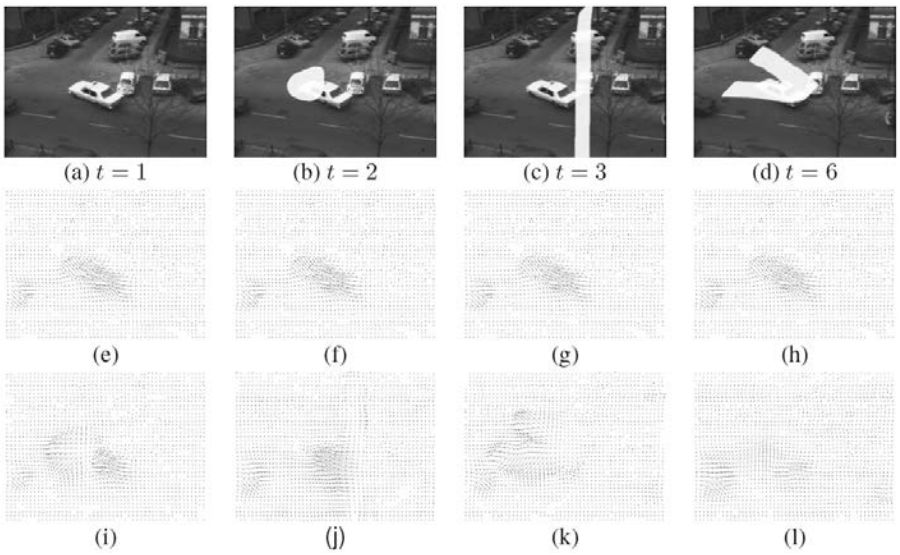

FIGURE 2.5 – **Result on a classic video sequence :** (a) : initial image ; (b–d) : the three blurred images of the sequence ; (e–h) measured motion fields between times $(t = 1, t = 2)$, $(t = 2, t = 3)$, $(t = 5, t = 6)$ and $(t = 6, t = 7)$ with our approach ; (i–l) the corresponding motion fields obtained without a temporal consistency.

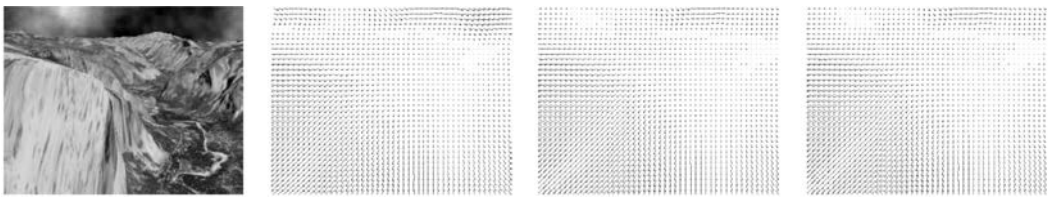

FIGURE 2.6 – **Yosemite sequence :** an image and three estimated motion fields

	err. #1	err. #2	err. #3
No assimilation	$3.69° \pm 2.20°$	$3.26° \pm 2.13°$	$3.77° \pm 2.49°$
Assimilation	$1.60° \pm 1.06°$	$1.80° \pm 1.05°$	$1.63° \pm 1.11°$

TABLE 2.1 – **Yosemite sequence :** average angular errors without and with assimilation using the same observation operator

motion fields guided by a dynamical model . To correctly deal with the huge state space we are facing, the minimization is handled using an adjoint formulation. The resulting process consists in alternating a forward integration of the state variable and a backward integration of the introduced adjoint variables.

This technique has been successfully applied in different situations : atmospheric motions, pressure data and classic video sequences involving rigid objects. In the next chapter we present other applications of the variational assimilation framework not directly related to motion estimation in image sequences.

Chapitre 3

Others applications of data assimilation

Sommaire

3.1 Overview

In the previous chapter we have introduced the variational assimilation framework to recover time consistent motion fields from image sequences. This framework has been able to deal efficiently with the large system states composed by the velocity fields we were focused on. Of course, the assimilation framework is not only devoted to the estimation of motion fields but various parameters can be recovered.

In this chapter we present four other applications related to computer vision. The first one, in section 3.2, concerns curve tracking where we aim at monitoring two curves corresponding to the heart and the active areas of some convective systems. The second application is devoted to Sea Surface Temperature (SST) data reconstruction (section 3.3). The third one in section 3.4 uses the framework of variational data assimilation to perform efficient multi-resolution techniques (with applications to optical-flow computation), the time being related to the different scales of the flow. Lastly, based on some studies that create a link between very dense crowds and fluid flows, we use in section 3.5 techniques issued from variational data assimilation to manage crowds with videos (estimation of the velocities and other parameters, animation of crowded scenes).

3.2 Convective cell tracking

Convective cells are atmospheric events that are known to be associated with hazardous consequences, such as strong wind drafts, lightnings, heavy rainfalls, hails or even tornadoes. Over tropical areas such as central Africa, convective cells produce most of the rain during the monsoon period. They are also indirectly linked to droughts and floods, which might afflict this area. Their analysis and forecasting are thus of the utmost interest for meteorologists and forecasters. They can be characterized by two distinct regions : the *heart* (also named *core*, *center* or *active part*) where the strongest rains appear and the *influence area*. An example of a convective cell phenomenon is illustrated in figure FIG. 1.2.

The measurement of the convective cells parameters can be done either by the use of conventional probes or through satellite data. However, over remote areas (like the Amazonian forest for instance), conventional sensors such as radiosonde, rain gauges, radars or lightning detectors have a limited coverage. Satellite information constitutes therefore an appealing alternative for the study of convective atmospheric activity over these particular regions. In practice, such phenomena are analyzed using the temperature computed from different channels of meteorological data. Our image observations I are then related to the temperature.

In computer vision, a primal strategy to delineate the contours of complex objects relies on the implementation of partial differential equations encoding the evolution of parametric or non parametric curves toward the minimizers of an energy functional [Caselles 1997, Chan 2001, Kass 1988]. The corresponding functionals include generally a data term representative of a photometric distribution characterizing the object of interest and some regularity constraints on the curves. These non linear deterministic minimization strategies are in practice very sensitive to the initial curve location and topology. Among the different extensions of those methods, the Eulerian "level-set" approach [Osher 1988, Sethian 1999] has been specifically proposed to alleviate such shortcomings. In this framework, the contour's shape is represented as the zero level-set of an implicit higher-dimensional scalar function. The evolution of this implicit surface describes the contour's evolution and naturally enables the handling of topology changes. Such techniques have been already proposed in a meteorological context [Cohen 1998, Papin 2000, Yahia 1998]. However they generally remain on static detection/segmentation approaches applied quasi-independently on the images of the sequence with no temporal consistency guaranty on the recovered shape sequences.

We have proposed to exploit the variational assimilation framework to simultaneously track the two regions of interest of convective cells. This is briefly introduced in the next sections.

3.2.1 System state and dynamical model

Within level sets, a curve at time t, $\mathcal{C}_t(p) = \mathcal{C}(p,t) : [a,b] \times \mathbb{R}+ \rightarrow \mathbb{R}^2$, is implicitly described by the zero level set of a scalar function $\phi(x,t) : \Omega \times \mathbb{R}+ \rightarrow \mathbb{R}$:

$$\mathcal{C}_t(.) = \mathcal{C}(.,t) = \{x \in \Omega \mid \phi(x,t) = 0\}, \tag{3.1}$$

where Ω stands for the image spatial domain. The surface is driven by the contours dynamics and is chosen so as to have for instance positive values inside the curve and negative values outside. A common choice for the implicit function is the signed distance but any other surfaces whose level sets fits the curves of interest is possible. In order to encode the description of a convective cloud system encapsulating a set of convective cells, the system state $\boldsymbol{X}$ we used is then composed of two implicit surfaces :

- The first one, ϕ^e, is devoted to the description of the external delimitations (i.e. influence area) of the convective cells, $\mathcal{C}^e(t)$. These curves will be associated to a first level of brightness temperature threshold T_e.
- The second one, ϕ^c represents the cold core region of each cells, $\mathcal{C}^c(t)$. It is related to a colder threshold value T_c of the brightness temperature.

The first level set is defined on the whole image domain Ω : $\phi^e(x,t) : \Omega \times \mathbb{R}+ \rightarrow \mathbb{R}$ whereas the second one is defined inside the domain encapsulated by the convective cells contours, $\mathcal{I} = \{x \mid \phi^e(x,t) > 0\}$ (*i.e.* the domain delineated by the zero level set of ϕ^e) : $\phi^c(x,t) : \mathcal{I} \times \mathbb{R}+ \rightarrow \mathbb{R}$. Assuming that each curve is :

1. submitted to a motion field along its normal ;
2. propagated by this motion field ;
3. up to an uncertainty along its normal ;
4. up to an uncertainty along its tangent,

we can formalize, for any of the two curves :

$$d\mathcal{C}_t^i = (w^i \cdot n^i)n^i dt + \sigma_n n^i d\boldsymbol{B}_t^n + \sigma_\tau n^{i\perp} d\boldsymbol{B}_t^\tau . \tag{3.2}$$

Here $n^i d\boldsymbol{B}^n$ and $n^{i\perp} d\boldsymbol{B}^\tau$ are two independent Brownian motions directed along and perpendicularly to the curves normals and σ_n, σ_τ are the associated uncertainties. In this model, the curve is transported by a deterministic drift associated to the velocity field (first term of relation (3.2)) that is mitigated with isotropic Gaussian incertitudes –along the normal and tangent– whose covariances grow linearly in time (second and third terms of (3.2)). As mentioned previously, the curve location is defined from the evolution of an implicit surface $\phi^i(x,t)$. Therefore this surface depends on the stochastic process $\mathcal{C}_t$ and its differential must be defined using stochastic calculus differentiation rules and in particular the so called Îto formula [Oksendal 1998], already introduced in chapter 1. We get the following stochastic partial differential equation (in the following, for sake of clarity, we will drop the curve's index $i = \{e, c\}$ unless explicitly needed) :

$$\left(\partial_t \phi + w \cdot \nabla \phi + \frac{1}{2} \sum_{\{x_i, x_j\} = \{x,y\}} \frac{\partial^2 \phi}{\partial x_i \partial x_j} d\langle \mathcal{C}_t^{x_i}, \mathcal{C}_t^{x_j} \rangle \right) dt + \sigma_n |\nabla \phi| d\widehat{\boldsymbol{B}}_t^n = 0, \tag{3.3}$$

where $\mathcal{C}_t^x$ and $\mathcal{C}_t^y$ correspond to the coordinates of the curve-points in the Euclidian plan at time t. As previously, we have introduced velocity drifts $w(x)$ and Brownian motions $\hat{\boldsymbol{B}}_t^n(x)$ which are extensions on the whole plane of the curves drift and noise. For the drifts, we considered a unique smooth velocity field defined on the whole plane for both curves. This velocity field is in practice obtained by the estimator proposed in section 1.4 of chapter 1. Developing the quadratic variations of the form $\langle \mathcal{C}_t^{x_i}, \mathcal{C}_t^{x_j} \rangle$ yields :

$$\underbrace{\left(\frac{\partial \phi}{\partial t} + \mathbb{M}(\phi) \right)}_{\text{dynamic model}} dt + \sigma_n |\nabla \phi| d\hat{B} = 0, \tag{3.4}$$

with

$$\mathbb{M}(\phi) = w \cdot \nabla \phi + \frac{\sigma_\tau^2}{2} \kappa |\nabla \phi| + \frac{\sigma_n^2}{2|\nabla \phi|^2} \nabla \phi^T \nabla^2 \phi \, \nabla \phi, \tag{3.5}$$

where $\nabla^2 \phi$ denotes the Hessian matrix and κ is the mean curvature : $\kappa = \text{curv}(\phi) = \frac{1}{\|\nabla \phi\|}(\Delta \phi - \nabla \phi^T \nabla^2 \phi \, \nabla \phi)$. The temporal expectation of relation (3.4) is its deterministic part and gives our evolution models for curves ϕ^i, $i = \{e, c\}$. All details regarding this dynamical model, the way we estimate the uncertainties (σ_n, σ_τ), the formulations of adjoints and the implementations can be found in [Thomas 2009, Thomas 2010].

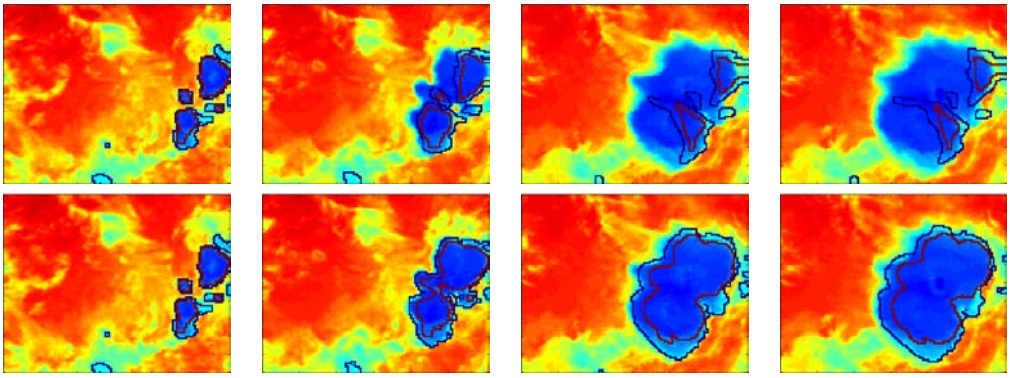

FIGURE 3.1 – **Convective cell tracking : sequence#1**. 4 images of the sequence. The first line corresponds to the contours obtained after the propagation of the initial contour with the proposed level set's dynamics ; the second line shows the final results after the assimilation process. Influence area are in blue and active part in red.

3.2.2 Observation operator

It is not possible to construct an observation term that relies on a reference temperature histogram since the spatial organization of the temperature inside a convective cell evolves along time. Assuming, as it is commonly done in convective cells detection issues, that the core's activity (resp. its external area) lies in temperatures under a given threshold T_c (resp. above T_e), the function ϕ, whose zero-level corresponds to the border to extract, should be such as :

$$H(I(x) - T_\bullet)(1 - H(\phi^\bullet(\mathbf{x}))) + H(T_\bullet - I(x))H(\phi^\bullet(\mathbf{x})) = \varepsilon, \tag{3.6}$$

where $\bullet = \{e, c\}$ and H is the Heaviside function ($H(x) = 0$ if $x < 0$ and $H(x) = 1$ elsewhere). This relation is zero if $I(x) > T_\bullet$ and $\phi(\mathbf{x}) > 0$ or if $I(x) < T_\bullet$ and $\phi(\mathbf{x}) < 0$. This measurement model favors thus the curve interior to be above of a given threshold and the exterior to be lower of the same threshold. Otherwise this function is always positive. Hence, this relation enables to define the observation system $\boldsymbol{\mathcal{Y}} = \mathbb{H}(\phi)$ as :

$$\begin{cases} \boldsymbol{\mathcal{Y}} = 0 \\ \mathbb{H}(\phi) = H(I(x) - T_\bullet)(1 - H(\phi(\mathbf{x}))) + H(T_\bullet - I(x))H(\phi(\mathbf{x})) \end{cases} \tag{3.7}$$

The operator $\mathbb{H}$ is non-linear with respect to ϕ. Its associated tangent linear operator, adjoint operator, associated error covariance matrices and implementations issues can be found in [Thomas 2009, Thomas 2010].

3.2.3 Some results

We have first tested the method on a sequence of images that exhibits the evolution of an important convective cell. The assimilation results are shown in figure FIG. 3.1. The first line represents four images of the sequence where the propagation of the initial contours through the dynamical model are superimposed (the contour in blue represents the cell and the one in red is related to the core). The second line exhibits the results after the assimilation. On the first row of this figure, one can observe that the development of the dynamical model provides already a coarse approximation of the final contour location for the whole convective cell (larger contour). In this particular example, the cell development is progressive and almost linear. The level set dynamical model has been able to predict quite

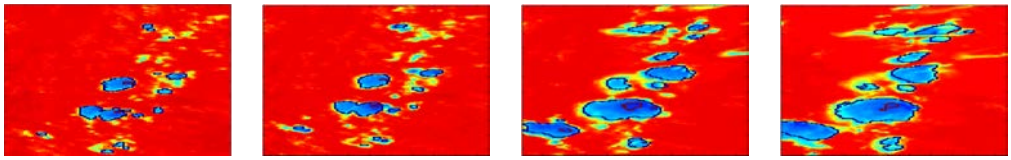

FIGURE 3.2 – **Convective cell tracking : sequence#2** : 4 images of the sequence where the influence area of the cell (blue) and its heart (red) obtained after the assimilation process are superimposed.

accurately the successive locations of the cell contours. At the opposite, the cell core is slowly dissipating along the sequence and undergoes a far more chaotic behavior. The benefit of the assimilation process clearly appears on the second line of the figure 3.1 since the estimated curves related to the contour and the core of the cell are well in line with the visualized sequence. The second experiment represents a more complex scene since it contains several cells at different degrees of evolution. In addition, as no convective phenomena are initiated in the first image, no curves were used for the initial condition. The very first forecast of the initial flat temperature surface corresponding to this initial condition obviously failed in predicting the first series of contours where new cells develop. Despite this, we can observed on figure FIG. 3.2 that the assimilation process enables to estimate accurately the contours of the convective cells and their hearts. These two experiments demonstrate the ability of the proposed assimilation process to recover reliable curves related to the contour and the heart of the convective cells.

Let us now turn to the reconstruction of sea surface temperature images.

3.3 Sea Surface Temperature reconstruction

Because of the cloud coverage, sea surface temperature (SST) images produced from satellite recordings contain missing data, as illustrated in the first line of figure FIG. 3.3. Usually, a preliminary step before any processing on the SST images is the missing data interpolation. Many algorithms have already been proposed for missing data interpolation. Up to now, most of the existing methods are based on Kalman Filtering or smoothing frameworks [Belyaev 2001]. The main drawback of the Kalman filtering methods is that, because of the large dimensionality of SST images, estimating the covariance matrix of the states tends to be computationally expensive, as it requires the inversion of very large matrices. We have proposed a method based on the variational data assimilation framework to assimilate missing data in SST images.

To perform the assimilation, the system state X corresponds to the SST (also noted θ) and the observation operator is the identity. Its dynamics follows the heat equation :

$$\frac{\partial X}{\partial t} = \nu \Delta X \tag{3.8}$$

where ν is a diffusion coefficient. Adapting the observation error covariance matrix R (cf relation (2.4)) to the presence/absence of data allows to recover the SST information at each location of the ocean, as illustrated in the second line of figure FIG. 3.3. This temporal regularity constraint has enabled to improve the interpolated SST data compared with usual interpolation techniques. To carry on with the quality of the reconstruction, it should be noted that at some locations, chlorophyll observations are available. This scalar quantity evolves following an advection-diffusion process and has fronts at the same location than SST ones. It is therefore possible to exploit this property by assimilating both SST and

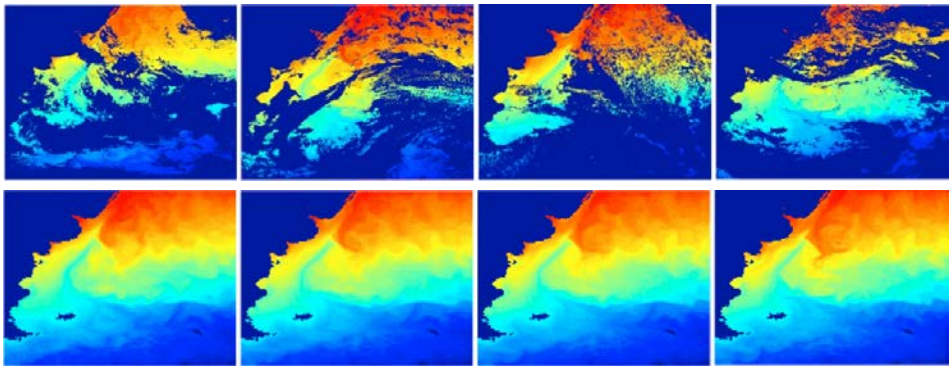

FIGURE 3.3 – **Assimilation of Sea Surface Temperature (SST) images**. First line : input data corrupted with cloud coverage ; Second line : assimilated SST.

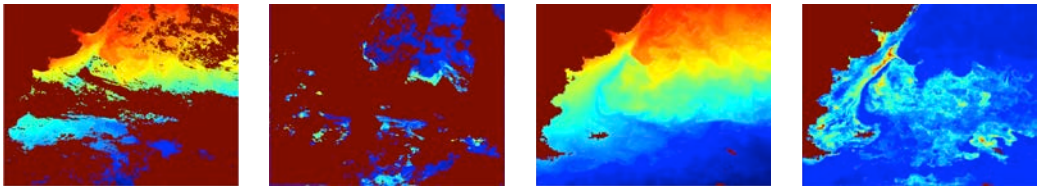

FIGURE 3.4 – **Joint assimilation of SST and chlorophyll images**. (a-b) : input SST and chlorophyll images ; (c-d) : corresponding assimilated results.

chlorophyll. The system state reads then $X = [\theta, \chi]^T$ where χ stands for the chlorophyll concentration values. Therefore one rewrites the cost function of the variational assimilation framework in (2.4) by adding a penalization term yielding :

$$\mathcal{J}(X) = \frac{1}{2}\int_{t_0}^{t_f} \|\theta_{obs} - \theta\|^2_{R_\theta^{-1}} dt + \frac{1}{2}\int_{t_0}^{t_f} \|\chi obs - \chi\|^2_{R_\chi^{-1}} dt + \frac{1}{2}\|X(\boldsymbol{x}, t_0) - X_0(\boldsymbol{x})\|^2_{B^{-1}}$$
$$+ \frac{1}{2}\int_{t_0}^{t_f} \|\frac{\partial X}{\partial t}(\boldsymbol{x}, t) + \mathbb{M}(X(\boldsymbol{x}, t))\|^2_{Q^{-1}} dt - \frac{1}{2}\int_{t_0}^{t_f} g_\beta(|\nabla\theta|) \left\langle \frac{\nabla\theta}{|\nabla\theta|}, \frac{\nabla\chi^\perp}{|\nabla\chi|} \right\rangle dt, \tag{3.9}$$

where the evolution model is composed of the heat equation for θ and advection-diffusion for χ. It reads :

$$\mathbb{M}(X) = \begin{pmatrix} -\Delta & 0 \\ 0 & \boldsymbol{v}\cdot\nabla - \nu\Delta \end{pmatrix} \begin{pmatrix} \theta \\ \chi \end{pmatrix} \tag{3.10}$$

where $\boldsymbol{v}$ is an external velocity field (provided by meteorological centers or estimated from the data). The additional term of the cost-function (last part of relation (3.9)) aims at imposing SST and chlorophyll fronts at the same locations. It is composed of an edge detector : $g_\beta(x) = 2/(1+\beta x) - 1$ that highlights SST fronts and the scalar product enforces a same direction of the gradients $\nabla\theta$ and $\nabla\chi$. The figure FIG. 3.4 illustrates some results. It can be observed that fronts appear more clearly for both data and their locations are consistent.

Despite an overall rating very efficient compared to existing approaches, it nevertheless appeared during the validation step that most of the errors were concentrated on the fine

scale structures of the flow. Our current work is then concentrating on the use of more adapted models for a better recovery of the fine scale structures. In particular we focus on Surface Quasi-Geostrophic equations dynamical models [Lapeyre 2006]. They are based on an advection-diffusion principle where the diffusion is "softer" than the usual Laplacian. It corresponds to a diffusion of a scalar θ of the type $\sqrt{\Delta}\theta$ instead of $\Delta\theta$. It is proved in [Lapeyre 2006] that such models are more adapted to the fine scales. To solve mathematically the problem, we are rewriting the assimilation system in a spectral domain in order to simplify the computational aspects related to this new diffusion.

Let us now introduce the way we used the variational assimilation framework for multi-resolution analysis.

3.4 Data assimilation for multi-resolution

In this section we briefly introduce the principle of the multi-resolution process (next paragraph), then we highlight some difficulties (in section 3.4.2) and in section 3.4.3, we propose an original way based on variational assimilation to perform the multi-resolution. This work is under process and preliminary results are exhibited here.

3.4.1 General principle of multi-resolution

Many computer vision techniques (related to motion estimation, segmentation, characterization, ...) can be seen as finding a variable X by solving an equation $\mathcal{H}(X, I, \boldsymbol{X}^0)$ that depends on the image luminance I and the pixel grid $\boldsymbol{X}^0$.

Because most of the assumptions used often only hold in a linear case (as the optical flow constraint equation of relation (1.1) which is valid only for small displacements), it is common to embed the resolution of $\mathcal{H}(X, I, \boldsymbol{X}^0)$ in a so-called "multi-resolution" scheme. The main principle consists in redefining the images on smaller grids $\boldsymbol{X}^N$ that correspond to the initial grid $\boldsymbol{X}^0$ divided by a factor N. On such "coarse" images, we assume that de resolution of $\mathcal{H}(X, I, \boldsymbol{X}^N)$ can be done under linear constraints and this provide a coarse approximation X^N of the final solution X. In a step forward, this approximation X^N is used as an initial condition for a new problem where the goal is to extract a refinement dX (with $X = X^N + dX$) that can be estimated from X^N using linear constraints. Such process is commonly repeated for several levels of resolutions yielding a succession of linear problems.

To get such "coarse" data on which the problem is solved, a usual strategy consists in using a pyramidal decomposition of the images, for instance with wavelet decompositions or gaussian filtering followed by decimations, as illustrated in Fig. 3.5(a) for a factor $N = 2$. The estimation is then performed first from the smallest images (under linear constraints) and the solution is reprojected to the following level. Another possibility that we have proposed in [Corpetti 2011] consists in obtaining X^ℓ (related to the solution of a problem $\mathcal{H}(X, I, \boldsymbol{X}^\ell)$ at a resolution ℓ) by performing a convolution of $\mathcal{H}(X, I, \boldsymbol{X}^0)$ by a gaussian kernel of standard deviation ℓ. Indeed, a multi-resolution scheme consists in redefining the problem on a grid $\boldsymbol{X}^\ell$ which can be viewed as a coarse representation of the initial grid $\boldsymbol{X}^0 = \boldsymbol{X}$ with a Brownian isotropic uncertainty of constant variance ℓ (see the illustration in figure 3.5(b)) :

$$\boldsymbol{X}^\ell = \boldsymbol{X}^0 + \ell\, \mathbb{I}_2 d\boldsymbol{B}. \tag{3.11}$$

where $\boldsymbol{B}$ is a standard Brownian motion and $\mathbb{I}$ the 2D identity matrix. Any solution X^ℓ of a problem $\mathcal{H}(X, I, \boldsymbol{X}^\ell)$ defined on a grid $\boldsymbol{X}^\ell$ should satisfy the expectation $E(\mathcal{H}(X, I, \boldsymbol{X}^\ell)|\boldsymbol{X}^0)$ which is equivalent (see [Corpetti 2011] for the demonstration) to

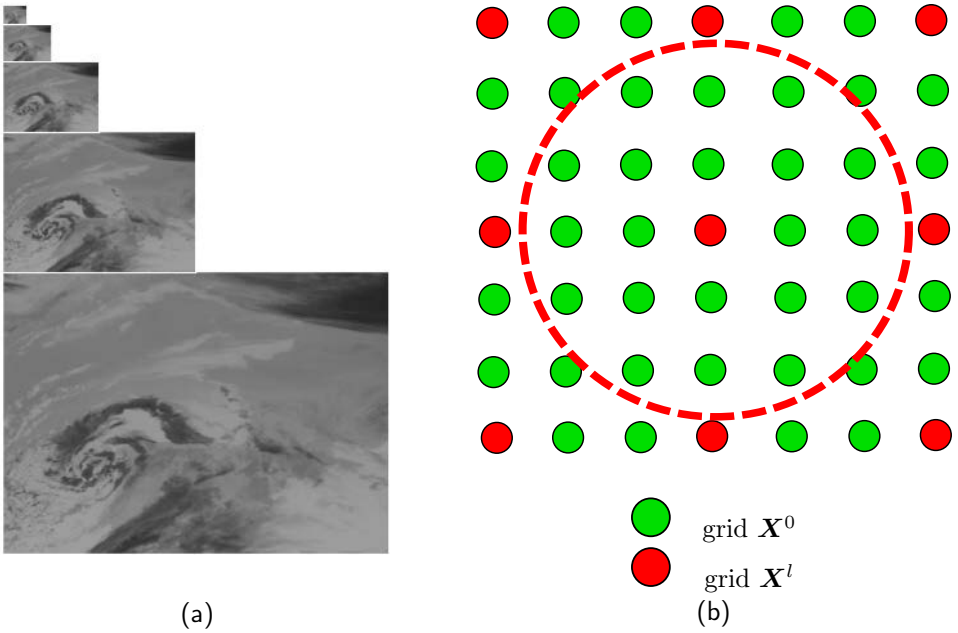

FIGURE 3.5 – **Different representations of the multiresolution**. (a) : a usual pyramidal decomposition ; (b) a stochastic process where green circles represent the original pixel grid and red circles represented the grid at a given resolution ℓ.

a convolution of $\mathcal{H}(X, I, \boldsymbol{X}^0)$ with the isotropic gaussian $\mathcal{N}(O, \ell)$. Therefore the multi-resolution can be performed by solving a family of problems $g_\ell * \mathcal{H}(X, I, \boldsymbol{X}^0)$ at the various resolutions ℓ. A main advantage of such a formulation of the multi-resolution setup is to naturally get rid of the use of a pyramidal image representation. Instead of dealing with successive decimations of factor 2 of the initial image to fix the different multiresolution levels, the evolutions of the levels ℓ are much flexible here.

3.4.2 Difficulties

Whatever the multi-resolution setup chosen, one of the main difficulty remains on the succession of *independent* problems : at a given resolution ℓ_n, the problem consists in finding dX^{ℓ_n} using $X^{\ell_{n+1}}$ as a coarse approximation : $X^{\ell_n} = X^{\ell_{n+1}} + dX^{\ell_n}$. Once X^{ℓ_n} estimated, its value is kept during the rest of the process. This is somewhat prejudicial since it is now recognized that small scales (related to finer resolutions) interact with larger scales. With such schemes, at a given resolution ℓ_n, the information related to smaller scales $\ell < \ell_n$ can not be taken into account. In addition, any error in the estimation of X^{ℓ_n} will also be kept and propagated across the resolutions without any possibilities of correction.

To deal with these difficulties, we propose in the following section a solution based on data assimilation.

3.4.3 Variational assimilation for multi-resolution

In this section we illustrate the way we exploit the variational assimilation framework for efficient multi-resolution schemes.

The usual temporal variable t is now connected to the different resolutions. We rather

prefer to represent its value with the parameter $\ell : \ell = 0$ corresponds to the "plain" resolution at the image grid and we assume that the system state X evolves across the resolutions following :

$$\frac{\partial X}{\partial \ell} = \frac{1}{2}\Delta X. \tag{3.12}$$

Indeed, it can easily be demonstrated that the solution of the previous relation is

$$X^\ell = X(\ell) = g_{\sqrt{\ell}} * X(0), \tag{3.13}$$

where $g_{\sqrt{\ell}}$ is a gaussian kernel of standard deviation ℓ. As shown in the previous paragraph, this relation enables to accede to the various scales of X. The model in (3.12) is then a perfect modeling for an exploration of X at different resolution levels.

The multi-resolution estimation procedure consists now to estimate $X(0)$ at the initial artificial time $\ell = 0$ (which corresponds to the image grid) under the perfect model of relation (3.12). The initial condition X_0 is set to zero and the observation system $\boldsymbol{\mathcal{Y}}(\boldsymbol{X}^0) = \mathbb{H}(\boldsymbol{X}^0, X^0)$ defined at the image grid $\boldsymbol{X}^0$ reads for any resolution $\ell \geqslant 0$:

$$\begin{cases} \boldsymbol{\mathcal{Y}}(\boldsymbol{X}^\ell) = g_{\sqrt{\ell}} * \boldsymbol{\mathcal{Y}}(\boldsymbol{X}^0) \\ \mathbb{H}(\boldsymbol{X}^\ell, X^\ell) = g_{\sqrt{\ell}} * \mathbb{H}(\boldsymbol{X}^0, X^0). \end{cases} \tag{3.14}$$

Following the algorithm described in section 2.2 of chapter 2, as the first integration of the dynamic model in (3.12) with null initial condition gives zeros, the process is expressed as (with B and R the error covariance matrices related to the uncertainty on the initial condition and the observations) :

1. $\tilde{X}(\ell) = 0 \ \forall \ell \in [0, \ell_f]$ compute the adjoint variables $\boldsymbol{\lambda}(\ell)$ with the **downscaling** equation :

$$\begin{aligned} &\boldsymbol{\lambda}(\ell_f) = 0 \ ; \\ &-\frac{\partial \boldsymbol{\lambda}}{\partial \ell}(\ell) - \frac{1}{2}\Delta\boldsymbol{\lambda}(\ell) = \left(\partial_X \mathbb{H}^\ell\right)^* R^{-1}(\boldsymbol{\mathcal{Y}}(\boldsymbol{X}^\ell) - \mathbb{H}(\boldsymbol{X}^\ell, \tilde{X}^\ell)) \end{aligned} \tag{3.15}$$

2. Update the **correction at the image grid** : $dX(0) = B\boldsymbol{\lambda}(0)$;
3. Assess to the correction at all the resolution levels $dX(\ell)$ from $dX(0)$ with the **upscaling** equation :

$$\frac{\partial dX}{\partial \ell} = \frac{1}{2}\Delta dX \tag{3.16}$$

4. **Update** : $\tilde{X} = \tilde{X} + dX, \ \forall \ell \in [0, \ell_f]$
5. **Loop** to step (1) until convergence

The first step corresponds to the usual downscaling approach : from coarse to fine resolutions, we compute and propagate the errors. This enables to refine the solution at the image grid (step 2). Unlike the classic multi-resolution, we then re-propagate this correction at the various resolutions (step 3) and the process is repeated until convergence. This framework enables to modify former solutions at given resolution $\ell = L$ by taking into account their influence on smaller scales $\ell < L$. This answers a difficulty mentioned in section 3.4.2 and authorizes a correction of the estimations at the resolution levels.

3.4.4 Some results

We have tested this framework for the motion estimation issue. The system state $X = \boldsymbol{v} = [u, v]^T$ represents the velocity field to estimate between images $I(\boldsymbol{X}^0, t-1)$ and $I(\boldsymbol{X}^0, t)$.

	COM	HS	DC 1	DC 2	ANISO	LK	OFCE	**AMR**
AAE	4.58^o	4.27^o	4.35^o	3.04^o	3.12^o	6.07^o	4.53^o	$\mathbf{3.74^o}$
RMSE	0.1520	0.1385	0.1340	0.09602	0.0961	0.1699	0.1243	**0.1057**

TABLE 3.1 – **Quantitative comparisons on the DNS sequence** with a commercial technique based on correlation (COM, LA VISION SYSTEM), Horn & Schunck (HS, [Horn 1981]), two fluid dedicated motion estimators with div-curl smoothing terms (DC 1 : [Corpetti 2002] ; DC2 : [Yuan 2007]), the stochastic approach presented in chapter 1 in anisotropic version (ANISO), a Pyramidal Lucas-Kanade (LK, [Lucas 1981]), a Lucas-Kanade term embed in a multi-resolution scheme with successive convolutions without any assimilation (as presented in section 3.4.1, OFCE) and the proposed multi-resolution using variational assimilation (AMR).

Using a Lucas-Kanade technique (presented in section 1.2.3 of chapter 1) at a resolution ℓ yields an observation system defined as :

$$\begin{cases} \boldsymbol{\mathcal{Y}}(\boldsymbol{X}^\ell) = g_{\sqrt{\ell}} * g_\sigma * \big(I(\boldsymbol{X}^0, t) - I(\boldsymbol{X}^0, t-1)\big) \\ \mathbb{H}(\boldsymbol{X}^\ell, X^\ell) = -g_{\sqrt{\ell}} * g_\sigma * \boldsymbol{\nabla} I^T(\boldsymbol{X}^0, t) \end{cases} \tag{3.17}$$

where the adjoint $\big(\partial_X \mathbb{H}(\boldsymbol{X}^\ell, X^\ell)\big)^*$ reads $-g_{\sqrt{\ell}} * g_\sigma * \boldsymbol{\nabla} I(\boldsymbol{X}^0, t)$ and g_σ is a convolution with a gaussian of standard deviation σ related to the Lucas & Kanade strategy. It should be outlined that this observation model is implemented for a testing issue but obviously, one of the main advantage of this framework is its possibility to naturally embed in the observation term some physical models accurately defined at a given resolution ℓ (sub-grid models in particular).

We have tested this technique on the synthetic particle images represented in the figure FIG. 1.6 of chapter 1. We also have re-depicted some of the numerical values of table 1.1 in table 3.1 where we have compared the proposed strategy with other techniques. It is very interesting to observe on this sequence that, for the same simple observation term related to the OFCE but embed in various multi-resolution strategies (LK : pyramidal, OFCE : access to the resolution levels but convolutions, AMR : the proposed technique), the presented one is the most efficient. We also outline from this table that the pyramidal technique usually exploited to obtain the various scales is less performing than a series of convolutions. Compared to more advanced techniques related to optical-flow or devoted to fluid images, the improvement obtained with this framework yields this technique very competitive.

More advanced evaluations are in progress. Let us now turn to the application of the assimilation framework for the analysis of crowds.

3.5 Application to other "flows" : crowd motion analysis

We also have used the variational assimilation framework for the analysis of crowds. Although the application is completely different, we have been based on some works (in particular [Hughes 2002, Hughes 2003]) that use fluid mechanics properties to model dense crowds. Analyzing crowd footages is of prime interest in a variety of problems : it can help to *i)* better understand crowd dynamics or the related behaviors [Helbing 2007], *ii)* develop surveillance or crowd control systems [Mehran 2009], *iii)* design and configure public spaces or as well *iv)* enrich computer animation models used in the context of video games or special effects [Courty 2007a, Courty 2007b, Lee 2007]. In the two last decades, two main strategies have been carried out to represent crowds :

1. representation at the *pedestrian* level : each individual is an entity/particle driven in a *Lagrangian* framework. The crowd representation results from the combination of a large number of entities.
2. the crowd is modeled in a *continuous* framework related to some scalar/vectorial characteristic quantities (density or displacement field for instance). The governing equations are represented in an *Eulerian* context and the individual notion is vanished.

The assimilation framework is adapted to this last representation. We have worked into three directions. First, we have proposed a simple crowd evolution model based on continuous laws. Roughly, this model states that the pedestrians aim at reaching their optimal direction (depending on their goal, position and obstacles) while preventing from dense areas. In a second step, this model has been exploited in a completely continuous way to recover the motion fields and the associated density of pedestrians. Lastly, a mixed continuous/discrete version of the model has been used to animate various crowd scenarios with specific properties fixed by the user. This is presented in the next sections.

3.5.1 Dynamic crowd model

We start from a scene with obstacles where all humans share the same goal. Reasonably assuming that each pedestrian aims at minimizing his travel time to his objective, the optimal direction $\boldsymbol{P}$ at a given location can be derived from the gradient of a potential function ϕ defined over the whole domain Ω. It can be shown that this potential is the solution of the classical Eikonal equation which has among others been widely used in the context of path planing [Kimmel 2001]. For a given scene, we then derive an optimal normalized direction field $\boldsymbol{P} = (U, V)^T = \nabla\phi/\|\nabla\phi\|$ of the pedestrians that corresponds to the theoretical normalized direction of a pedestrian without any constraints. If now the pedestrians evolve in a crowded environment, we assume that the deviations of their velocity from the optimal direction is due to the density that prevents from aiming the optimal direction. Therefore, we propose the following dynamical model :

$$\boldsymbol{v}(\boldsymbol{x},t) = \alpha(\rho)\Big(\underbrace{\boldsymbol{P}(\boldsymbol{x},t)}_{\text{wished direction}} - \underbrace{\beta(\rho)\nabla\rho(\boldsymbol{x},t)}_{\text{density repulsion}} \Big) \tag{3.18}$$

where α and β depend on the density ρ and need to be defined. The rule of α is to precise the global magnitude of the velocity of the pedestrians. As for parameter β, it aims at specifying the way the density influences the optimal direction. Their exact definition is presented in [Allain 2009], as well as strategies to avoid pedestrian collision. The output of the simulation model in (3.18) can be used as the input of a rendering processes in order to animate some flows using various conditions (lighting, shooting angle, ...). The figure FIG. 3.6 gives an example of some produced scenarios with various obstacles. This model has been validated from the point of *emergent situations* where we have demonstrated that some known emerging phenomena (depending on density/obstacles) are accurately reproduced.

3.5.2 Crowd analysis using variational assimilation

The aim is to extract the velocity and the density of the crowd. The estimation of the density is a tricky task in crowd analysis and the assimilation framework gives an appealing solution. The system's state X is composed of the two components of the velocity field $\boldsymbol{v} = (u, v)^T$ and of the density of the crowd ρ ($X = (u, v, \rho)^T = (\boldsymbol{v}, \rho)^T$). The dynamic model for the velocity is described in relation (3.18). As for the density we assume that

FIGURE 3.6 – **Crowd simulation model**. (a) : a real crowd picture ; (b–d) : some simulations provided by our model

this quantity is transported by the motion field and is diffused along time with a coefficient $\beta(\rho(\boldsymbol{x},t))$. It then obeys to a classical advection-diffusion relation and the overall dynamic model is (the spatio-temporal indexes $(\boldsymbol{x},t)$ being removed) :

$$\begin{bmatrix} \boldsymbol{v} \\ \frac{\partial \rho}{\partial t} \end{bmatrix} + \underbrace{\begin{bmatrix} 0 & \alpha(\rho)\beta(\rho)\boldsymbol{\nabla} \\ 0 & \boldsymbol{v}\cdot\boldsymbol{\nabla} - \beta(\rho)\Delta \end{bmatrix}}_{\mathbb{M}(X)} \begin{bmatrix} \boldsymbol{v} \\ \rho \end{bmatrix} = \begin{bmatrix} \alpha(\rho)\boldsymbol{P} \\ 0 \end{bmatrix} + \nu_{\mathbf{m}} \tag{3.19}$$

where $\nu_{\mathbf{m}}$ is an uncertainty.

The observation system $\boldsymbol{\mathcal{Y}} = \mathbb{H}(X) + \nu_o$ is defined on the basis of the OFCE (relation (1.1) which is valid for such rigid bodies) for the velocity field and no observations are available for the density. Therefore it reads

$$\boldsymbol{\mathcal{Y}} = \frac{\partial I(\boldsymbol{x},t)}{\partial t} \quad \text{and} \quad \mathbb{H} = \begin{bmatrix} -I_x(\boldsymbol{x},t), & -I_y(\boldsymbol{x},t), & 0 \end{bmatrix}. \tag{3.20}$$

This observation operator involves only the motion field. This means that the density correction will be achieved only from deviations of the dynamic model.

An illustration of the assimilation results on a real sequence representing a crowd entering a railway station in the city of Monaco is in FIG. 3.7. This example is interesting since a variety of phenomena are present : a continuous flow at the beginning followed by a compression of some peoples in the left part of the images. In addition, the limit of the door is a barrier that creates an opposite flux in the crowd flow. In this example, our method has detected (cf. images 3.7.(g-h)) two sensible areas where the density is growing larger : the end of the barrier and the wall on the right of the image. This kind of information associated to the density is very useful in many topics related to security, design, ... and is difficult to achieve with usual computer vision techniques. The reader can find more details in [Allain 2009].

3.5.3 Crowd animation using variational assimilation

In this section we aim at simulating some crowds with specific properties.

Simulating crowd of individuals has drawn a lot of attention over the past decades for the potential interests of computer graphics but also for safety engineering or robotics applications. Controlling a crowd to achieve a given effect is a rather difficult task, mostly because the only control parameters are those of the simulation model, which are generally not designed for it. We have proposed to solve this problem using data assimilation.

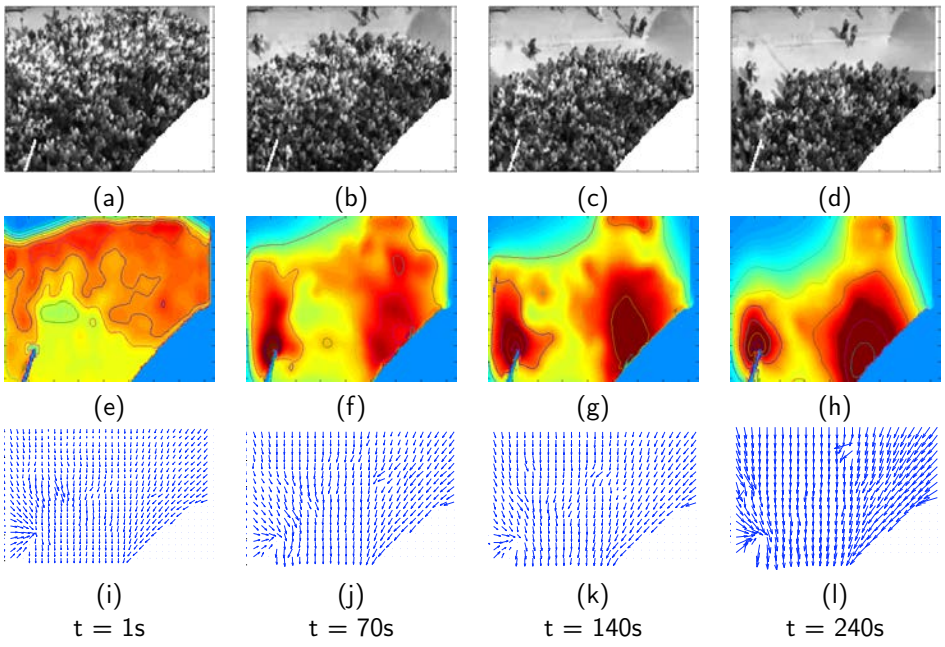

FIGURE 3.7 – **Results on a real crowd flow** representing the entrance of a subway. (a–d) : 4 images of the sequence ($t = 1s, 70s, 140s, 240s$) where the obstacles are superimposed (in white) ; (e–h) : estimated density and some level-lines ; (i–l) estimated motion fields for $t = 1s, 70s, 140s, 240s$.

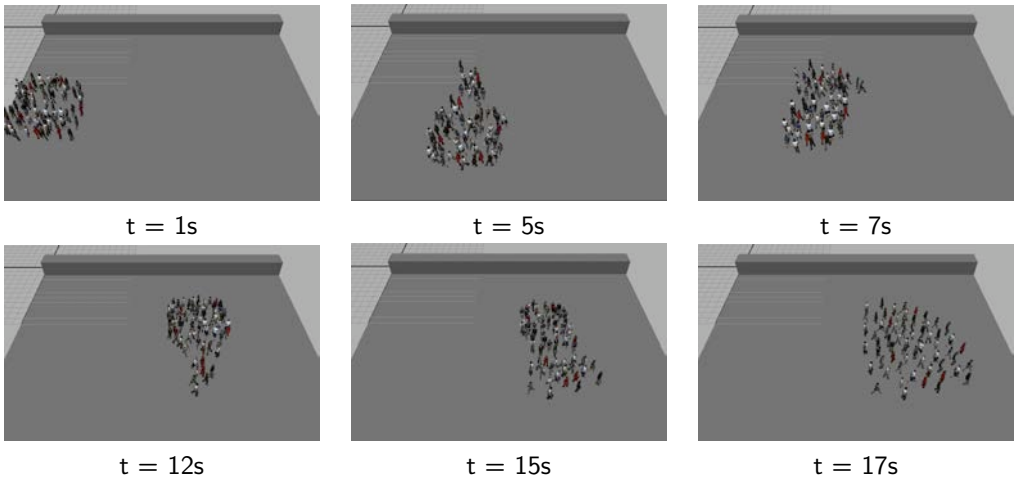

FIGURE 3.8 – **Crowd animation :** snapshots of a sequence obtained by imposing a constant vorticity of the motion field at time $t = 7s$ in the left part of the image and at time $t = 15s$ in the right part.

The crowd is composed of a set of N pedestrians and the system's state is of the form $X = [\boldsymbol{x}_1, \boldsymbol{v}_1, ..., \boldsymbol{x}_N, \boldsymbol{v}_N]^T$ where $i = \{1, ..., N\}$ and components $\boldsymbol{x}_i$ (resp. $\boldsymbol{v}_i$) are related to their positions and velocities. We have adapted the dynamical model in (3.19) to this new representation and we also included some constraints to avoid pedestrian collisions. The problem is now : how to find a complete sequence of states $X(t)$ submitted to a dynamical model where at some locations t_i we expect some components of the system state (position or velocity or both) to reach a given configuration fixed by the user. To answer this question, one can use the assimilation framework where the observation model $\boldsymbol{\mathcal{Y}}(t) = X(t)$ reads :

$$\boldsymbol{\mathcal{Y}}(t) = [\boldsymbol{x}_{obs}(t), \boldsymbol{v}_{obs}(t)]^T \tag{3.21}$$

where $\boldsymbol{x}_{obs}$ and $\boldsymbol{v}_{obs}$ are the wishes positions and velocities. The associated error covariance matrix $R^{-1}(t)$ is diagonal and of the form :

$$R^{-1}(t) = \begin{bmatrix} \mathbf{R_x^{-1}} & \mathbf{0} \\ \mathbf{0} & \mathbf{R_v^{-1}} \end{bmatrix} \tag{3.22}$$

where $\mathbf{0}$ is a null diagonal matrix of size $N \times N$. The matrices $\mathbf{R_x^{-1}}$ and $\mathbf{R_v^{-1}}$ are also diagonal of size $N \times N$. Their corresponding values are 0 when the user has no specific requirements and 1 otherwise.

Using the strategy of section 2.2 with these system state and observations models authorize the computation of the sequence $X(t)$ that corresponds to the positions and velocities of each pedestrians, under the constraints fixed by the user. For instance, in figure 3.8, we have plotted 8 images of an animated sequence of $20s$. Pedestrians aim at going on the right part of the image. We have imposed the vorticity of the global velocity field to reach constant homogeneous areas at time $t = 7s$ in the left part of the image and $t = 15s$ in the right part. The process has then builded a consistent set of trajectories for all the pedestrians, as we try to illustrate in figure 3.8. Note that if the observations are issued from real measurements (on image sequences) one gets a mean to produce a synthetic animation of an observed crowd.

3.6 Summary

In this section we have presented several computer vision tools based on assimilation techniques. We have in particular proposed approaches able to track curves, reconstruct missing data, perform multi-resolution and analyze crowd behaviors. For all these applications, the assimilation framework is an appealing solution for dealing in an efficient way with the large system state and the potentially lack of data. In addition, as shown in the crowd example, this tool is very promising for the estimation of unobserved parameters (like the density for crowds). We then believe that the data assimilation framework is very well adapted to the analysis of image sequences.

Conclusion of the first part

In this first part, we have been focused on the analysis of Low Spatial Resolution image sequences. On such data, atmospheric flows and oceanic circulations are visible and we have been focused on the definition of tools for motion estimation, curve tracking or data reconstruction for such specific motions.

To this end, we have first proposed original techniques for the motion estimation problem from a pair of images. The solutions include new observation terms either based on physical laws or on a stochastic interpretation of the luminance associated with adapted smoothing priors. When a sequence of image is available, we have been based on the variational assimilation framework which is an elegant way to efficiently deal with dynamical constraints, large system states and noising and/or missing observations. Several motion estimation techniques have been introduced, as well as tools for curve tracking and data reconstruction.

As the processing of such LSR data require some techniques issued from computer vision, we also have proposed more generic tools for time-consistent motion estimation and multiresolution analysis. In addition, we have presented an original way to manipulate crowds. In this latter situation, more than the application, an original technique to simulate and deal with discrete objects (pedestrians) submitted to continuous flows has been introduced.

In the second part of this document, we now focus on the analysis of Very High Spatial Resolution remote sensing images.

Deuxième partie

Very high resolution remote sensing images : pattern analysis and change detection

Introduction

As mentioned in the general introduction, the global context and long term objective of the researches that are developed concern the analysis of relationships between climate and land cover. Remote Sensing images are a privilege source of observation.

In that context, VHSR (Very High Spatial Resolution) data provide a valuable source of information for the analysis of land cover. However analyzing the patterns of VHSR images is more complex than with medium or low resolution data. As a matter of fact, VHSR images contain many relevant information but they also embed non-informative structures such as shadows, cars, animals, ... Many commercial tools exist for the manipulation of such data (such as IDRISI© [1], ENVI© [2] or eCognition© [3]) but they appear to be limited for advanced studies related to agriculture characterization or change detection. In this part, we are then focusing on the definition of techniques mainly (but not only) focused on the manipulation of agricultural data. It should be noted that these works have been done within the COSTEL group where not only the methodology was necessary but it was also required that possibly non-specialists researchers (from an image processing and computer science point of view) can easily apply the approaches to massive databases. This point has had an influence on some methodological choices.

This second part is structured as follows :

- The chapter 4 presents a general framework for the **characterization and comparison of agricultural parcels** and more generally textured patterns ;
- The chapter 5 gives some **applications of the previous descriptors** for the segmentation and the classification of agricultural parcels, the estimation of the orientation and the detection of textured fronts ;
- Finally the chapter 6 is devoted to the **change detection** problem where we propose several tools that either rely on the works of the previous chapters but we also introduce more generic approaches.

1. http://www.clarklabs.org/
2. http://www.ittvis.com/ProductServices/ENVI.aspx
3. http://www.ecognition.com/

Chapitre 4

Descriptors of agricultural parcels with wavelets and evidence theory

Sommaire

4.1 Overview

In this chapter we are focused on some specific patterns that appear in several remote sensing data. These patterns can either be related to :

- agricultural parcels : the different kind of cultures in crops, the different ways of diggings, ... make some specific textured patterns whose analysis is crucial in order to monitor the vegetation (see Fig. 4.1(a–c)) ;
- specific organization of clouds : for instance, the clouds generated at the so-called "sea breeze front" are natural markers of the limit of the penetration of the sea breeze inland, as illustrated in figure Fig. 4.1(d).

From these illustrations it is obvious that patterns are well discriminated by their orientation, scale, texture, ... Therefore a multi-scale analysis at different orientations appears to be a rational choice. In that context, wavelets consists in an appealing solution. In addition, as we will observe in the next chapter, we will have to compare some parcels whose size are different. The descriptors have then to be insensitive to the size of the patterns.

We then suggest to represent the different properties of the textured areas on the basis of the distribution of their wavelet coefficients. A general introduction and the underlying assumptions on which we rely are addressed in section 4.2. The section 4.3 presents our descriptors and section 4.4 introduces the way we compare two regions.

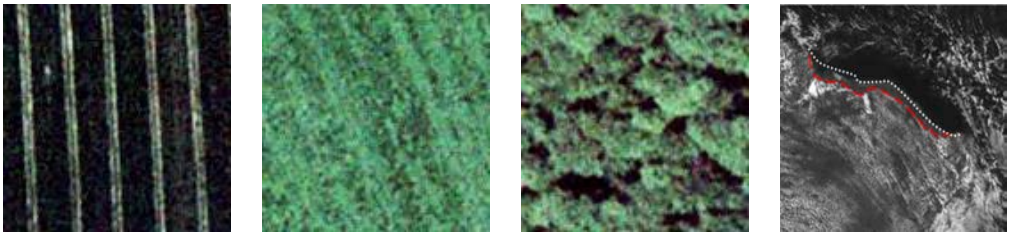

(a) (b) (c) (d)

FIGURE 4.1 – **Illustration of textured patterns** ;(a–c) : VHSR data representing cereals, sowed meadow and forest ; (d) : LSR data where the white line corresponds to the coast line whereas the red line corresponds to the sea breeze front, identify by the limit of a textured area composed of a line of cumuliform clouds.

4.2 Generalities about wavelet & assumptions

4.2.1 Wavelet decomposition of signals and images

Noting $f(x)$ a real signal (1-dimensional for the sake of clarity), its *continuous wavelet decomposition* $\mathcal{F}$ is :

$$\mathcal{F}(a,b) = \int_{-\infty}^{\infty} f(t) \frac{1}{\sqrt{a}} \overline{\psi}\left(\frac{t-b}{a}\right) dt \tag{4.1}$$

where ψ stands for the analyzing wavelet, $\overline{\psi}$ being the complex conjugate of ψ and a (resp. b) is a scaling (resp. position) parameter. Any combinations of scaling and position parameter are possible. For digital signals $I[n]$, a discrete transform can be defined as :

$$\mathcal{I}[j,k] = \sum_{n=-N/2}^{N/2} I[n] 2^{-\frac{j}{2}} \overline{\psi}\left[2^{-\frac{j}{2}}(n-k)\right] \tag{4.2}$$

for a position k and a scaling factor j. The support of the wavelet ψ is $[-N/2, N/2]$. It can be shown (see [Mallat 1989] for instance) that the family $\psi_{j,k} = \psi(2^{-\frac{j}{2}}(n-k))$ for $(j,k) \in \mathbb{Z}^2$ constitutes an orthonormal basis and any digital signal I can be represented as :

$$I[n] = \sum_k \mathcal{A}[k]\phi_{J,k}[n] + \sum_{j=-J}^{-1} \sum_k \mathcal{I}[j,k]\psi_{j,k}[n] \tag{4.3}$$

where ϕ is the scaling function. The coefficients $\mathcal{A}[k]$ correspond to an *approximation* (also named *continuous component*) of the initial signal I at resolution J and all $\mathcal{I}[j,k]$ are the *details* associated to the scale j. The total numbers coefficients $\mathcal{A}$ and $\mathcal{I}$ equals the number of elements of I. For 2D discrete signals like digital images, the extension of the orthonormal basis gives a wavelet decomposition that highlights an approximation band and three kinds details : horizontal, vertical and diagonals, as shown in figure 4.2(a-b).

4.2.2 Assumption related to wavelet coefficients

In a given sub-band of the wavelet decomposition, S.G. Mallat verified that the distribution of the wavelet coefficients related to details $\mathcal{I}[j,k]$ of any texture pattern follows a *Generalized Gaussian Density* (GGD) function [Mallat 1989]. The GGD reads :

$$p(x;\alpha,\beta) = \frac{\beta}{2\alpha\Gamma(1/\beta)} e^{-\left(\frac{|x|}{\alpha}\right)^{\beta}}, \tag{4.4}$$

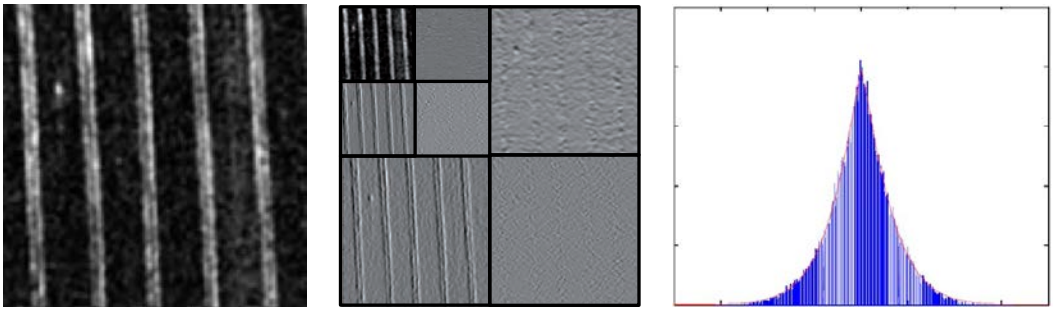

FIGURE 4.2 – **Example of a wavelet decomposition :** (a) : an input image ; (b) its decomposition on an orthonormal basis where the approximation band and the horizontal (resp. vertical, diagonal) are shown for 2 levels of decomposition. The vertical orientation of the pattern in (a) clearly appears in the vertical bands and does not affect other ones ; (c) : distribution and corresponding GGD for the vertical coefficients in the first level of the decomposition

and is characterized by two cœfficients : the *scale* parameter α and the *shape* parameter β [1]. The term $\Gamma(t) = \int_0^{+\infty} e^{-z} z^{t-1} dz$ is the mathematical Gamma function. Figure 4.2(c) illustrates the GGD distribution of the coefficients in a sub-band of a wavelet decomposition.

4.3 Characterization of agricultural parcels

Under the representation with GGD, any texture pattern can be characterized by a sequence :

$$\mathcal{T} = (\alpha_{j,Z}, \beta_{j,Z}) \tag{4.5}$$

where $J \leq j \leq -1$ is the scale analysis and $(\alpha_{j,Z}, \beta_{j,Z})$ are coefficients related to GGD in the $Z = \{H, V, D\}$ directions (corresponding to the horizontal, vertical or diagonal band). In practice, the estimation of parameters $(\alpha_{j,Z}, \beta_{j,Z})$ from a set of data is performed using a maximum-likelihood technique, as detailed in [Varanasi 1989]. The representation in (4.5) does not take into account the approximation of the original signal and is therefore only related to the texture components. In general the distribution of the approximation band does not a fit a GGD. If one desires to embed such continuous part in the representation, the descriptor is defined as :

$$\mathcal{T} = (\boldsymbol{p}, \alpha_{j,Z}, \beta_{j,Z}) \tag{4.6}$$

where $\boldsymbol{p}$ is a smooth histogram of the empirical distribution of the coefficients $\mathcal{A}[k]$. We prefer to rely on histograms in order to guarantee an independency with respect to the spatial location of the coefficients. The smoothing prevents from bad interpretations of the empirical distributions that are likely to be locally noisy. The technique used to smooth histograms is a kernel method [Bowman 1997].

The descriptors in (4.5-4.6) characterize our textured pattern issued from remote sensing data. As we use either a parametric representation of the distribution of coefficients (through GGD) or a smoothed histogram, some uncertainties $\boldsymbol{\Delta} = (\Delta_{\boldsymbol{p}}, \Delta_{j,Z})$ are introduced compared to the empirical distributions. They are computed from the root mean square

1. A gaussian distribution corresponds to $\beta = 2$

error of the estimation :

$$\Delta_\bullet = \sqrt{\frac{1}{x_2 - x_1}\int_{x_1}^{x_2} (p_\bullet(x) - \boldsymbol{p}_\bullet(x))^2 dx} \tag{4.7}$$

where $p_\bullet(x)$ (resp. $\boldsymbol{p}_\bullet$) $\in [x_1, x_2]$ is the empirical (resp. smoothed) distribution in the band $\bullet$. The next section proposes a way to compare two regions R_a and R_b characterized by $\mathcal{T}_a$ and $\mathcal{T}_b$ (relations (4.5) or (4.6)) and their associated uncertainties $\boldsymbol{\Delta}_a$ and $\boldsymbol{\Delta}_b$ (relation (4.7)).

4.4 Comparison of agricultural parcels with data fusion

To be more general, we assume that our descriptors include the approximation part (formulation in (4.6)). We aim at comparing two regions R_a and R_d described with $\mathcal{T}_a = (\boldsymbol{p}_a, \alpha_{a,j,Z}, \beta_{a,j,Z})$ and $T_b = (\boldsymbol{p}_b, \alpha_{b,j,Z}, \beta_{b,j,Z})$. We first define one similarity indicator $L(R_a, R_b)$ based on the luminance and several similarity indicators $T_{j,Z}(R_a, R_b)$ (j corresponding to the scale and Z to the horizontal, vertical or diagonal band of the wavelet decomposition) based on the texture. All the indicators are then fused in a step forward to define a unique similarity criterion.

4.4.1 Comparison of luminance

The luminance information is embedded in the approximation part. A criterion based on the Bhattacharyya formula is used :

$$L(R_a, R_b) = \left(1 - \int \sqrt{\boldsymbol{p}_a(x)\boldsymbol{p}_b(x)}dx\right). \tag{4.8}$$

This criterion L is null for two identical distributions and grows up to 1 when they differ. The associated incertitude is derived following uncertainty computations stating that any function $f(\boldsymbol{p}_a, \boldsymbol{p}_b)$ such that $\boldsymbol{p}_a(x) = p_a(x) \pm \Delta p_a$ and $\boldsymbol{p}_b(x) = p_b(x) \pm \Delta p_b$ is associated to an uncertainty $\Delta f(\boldsymbol{p}_a, \boldsymbol{p}_b)$ that reads :

$$\Delta f(\boldsymbol{p}_a, \boldsymbol{p}_b) = \left|\frac{\partial f}{\partial \boldsymbol{p}_a}(\boldsymbol{p}_a, \boldsymbol{p}_b)\right| \Delta p_a + \left|\frac{\partial f}{\partial \boldsymbol{p}_b}(\boldsymbol{p}_a, \boldsymbol{p}_b)\right| \Delta p_b. \tag{4.9}$$

This latter relation comes from the Taylor's theorem where all uncertainties have positive contributions. We then associate an uncertainty Δ_L to the criterion (4.8) which is :

$$\Delta_L(R_a, R_b) = \int \left(\left|\frac{\boldsymbol{p}_b}{2\sqrt{\boldsymbol{p}_a\boldsymbol{p}_b}}\right| \Delta p_a + \left|\frac{\boldsymbol{p}_a}{2\sqrt{\boldsymbol{p}_a\boldsymbol{p}_b}}\right| \Delta p_b\right), \tag{4.10}$$

4.4.2 Comparison of texture

We are based on the Kullback-Leibler criterion. This latter is defined between distributions $\boldsymbol{p}_a$ and $\boldsymbol{p}_b$ as :

$$KL(\boldsymbol{p}_a, \boldsymbol{p}_b) = \int_{-\infty}^{+\infty} \boldsymbol{p}_a(x) \log \frac{\boldsymbol{p}_a(x)}{\boldsymbol{p}_b(x)} dx \tag{4.11}$$

This criterion is non-symmetric. Depending on the application, it might be useful to use a symmetric version of the type $KLS(\boldsymbol{p}_a, \boldsymbol{p}_b) = (KL(\boldsymbol{p}_a, \boldsymbol{p}_b) + KL(\boldsymbol{p}_a, \boldsymbol{p}_b))/2$. For instance, if one wants to compare two regions, a symmetric version is useful. At the opposite, if we expect to highlight transitions between two parcels, a non-symmetric version is preferred.

For two GGD $\boldsymbol{p}_a$ and $\boldsymbol{p}_b$ defined with (α_a, β_a) and (α_b, β_b), this similarity measurement reads [Do 2002] :

$$KL(\alpha_a, \beta_a, \alpha_b, \beta_b) = \log\left(\frac{\beta_a \alpha_b \Gamma(1/\beta_b)}{\beta_b \alpha_a \Gamma(1/\beta_a)}\right) + \left(\frac{\alpha_a}{\alpha_b}\right)^{\beta_b} \frac{\Gamma((\beta_b+1)/\beta_a)}{\Gamma(1/\beta_a)} - \frac{1}{\beta_a}. \tag{4.12}$$

Its value is null for two identical distributions and progressively grows up when the distributions differ. To derive a criterion measurement in $[0,1]$ from the KL dissimilarity, we hence apply a function g of the type $g : [O, +\infty[\longrightarrow [0,1[$. The function g used is $g(x) = x^2/(\sigma^2 + x^2)$ and the critera $T_{j,Z}(R_a, R_b)$ for all pair $\{j, Z\}$ are finally defined by :

$$T_{j,Z}(R_a, R_b) = g(KL_\bullet(\boldsymbol{p}_a, \boldsymbol{p}_b)) \tag{4.13}$$

where $KL_\bullet$ is either the criterion in (4.11) or its symmetric version. The associated uncertainty reads (for $KL_\bullet = KL$) :

$$\begin{cases} \Delta_{T_{j,Z}}(R_a, R_b) = \dfrac{2\sigma^2 KL(\boldsymbol{p}_a, \boldsymbol{p}_b)}{(\sigma^2 + KL(\boldsymbol{p}_a, \boldsymbol{p}_b)^2)^2} \Delta KL(\boldsymbol{p}_a, \boldsymbol{p}_b) \quad \text{with} \\ \Delta KL(\boldsymbol{p}_a, \boldsymbol{p}_b) = \displaystyle\int_{-\infty}^{+\infty} \left| 1 - \frac{\boldsymbol{p}_b(x)}{\boldsymbol{p}_a(x)} + \log \frac{\boldsymbol{p}_a(x)}{\boldsymbol{p}_b(x)} \right| \Delta p_a dx \end{cases}. \tag{4.14}$$

It is important to outline that one could have use other similarity criteria, like the Bhattacharyya one, which has the advantage to directly be in the interval $[0,1]$. However, in our experiments, this latter was less discriminative than Kullback-Leibler [Lefebvre 2009]. Furthermore, to the best of our knowledge, the Kullback-Leibler criterion between two GGD is the only one that can be expressed in an analytic way, which simplifies many practical aspects.

A set of P indicators $\mathcal{C} = \{L(R_a, R_b), T_{j,Z}(R_a, R_b)\}$ $(J \leq j \leq -1, Z = \{H, V, D\})$ with associated incertitudes $\boldsymbol{\Delta}_\mathcal{C} = \{\Delta_L(R_a, R_b), \Delta_T(R_a, R_b)\}$ is then available to sense the similarity between regions R_a and R_b on the basis of their luminance and texture. From $\mathcal{C}$ and $\boldsymbol{\Delta}_\mathcal{C}$, the next section proposes a way to derive a unique similarity criterion.

4.4.3 Fusion of similarity criteria

For each criterion $\mathcal{C}(\ell)$, $\ell = 1...P$, we define three *mass functions* $m^A(\mathcal{C}(\ell))$, $m^B(\mathcal{C}(\ell))$ and $m^{A\cup B}(\mathcal{C}(\ell))$ related to the belief on three hypotheses :

1. Hypothesis A : regions R_a and R_b are similar following criterion $\mathcal{C}(\ell)$;
2. Hypothesis B : regions R_a and R_b are not similar following criterion $\mathcal{C}(\ell)$;
3. Hypothesis $A \cup B$: uncertainty about the similarity of the regions following criterion $\mathcal{C}(\ell)$;

where $m^A(\mathcal{C}(\ell)) + m^B(\mathcal{C}(\ell)) + m^{A\cup B}(\mathcal{C}(\ell)) = 1$. The way we get m from any criteria in $\mathcal{C}(\ell)$ is only a normalization step :

$$\mathcal{S} = 1 + \Delta_\mathcal{C}(\ell) \quad \text{and} \quad \begin{cases} m^A(\mathcal{C}(\ell)) = \Big(1 - \mathcal{C}(\ell)\Big)/\mathcal{S} \\ m^B(\mathcal{C}(\ell)) = \mathcal{C}(\ell)/\mathcal{S} \\ m^{A\cup B}(\mathcal{C}(\ell)) = \Delta\mathcal{C}(\ell)/\mathcal{S} \end{cases} \tag{4.15}$$

The values $m^A(\mathcal{C}(\ell))$, $m^B(\mathcal{C}(\ell))$ and $m^{A\cup B}(\mathcal{C}(\ell))$ constitute *mass functions* commonly used in evidence theory and can then be fused together. Among the available fusion approaches, we chose the Dempster's fusion rule issued from the well-known Dempster-Shafer theory

[Shafer 1976] that has proved to be very efficient in such context. This latter reads, for any hypothesis $\mathcal{H} \neq \emptyset$ and mass functions m_1 and m_2 to fuse :

$$m(\mathcal{H}) = [m_1 \oplus m_2](\mathcal{H}) = \frac{\sum\limits_{\mathcal{H}_1 \cap \mathcal{H}_2 = \mathcal{H}} m_1(\mathcal{H}_1) m_2(\mathcal{H}_2)}{1 - \sum\limits_{\mathcal{H}_1 \cap \mathcal{H}_2 = \emptyset} m_1(\mathcal{H}_1) m_2(\mathcal{H}_2)} \tag{4.16}$$

where $K = \sum\limits_{\mathcal{H}_1 \cap \mathcal{H}_2 = \emptyset} m_1(\mathcal{H}_1) m_2(\mathcal{H}_2)$ measures the conflict between sources m_1 and m_2. It should be noted that this fusion rule holds for independent sources of data. For that reason, we use wavelet packet decomposition since the related coefficients are less correlated together. In the future we will use Dempster-Shafer's based technique that take into account a dependency between sources of informations [Denoeux 2008]. As the Dempster's fusion rule is associative, one can apply the following algorithm to fuse all our criteria :

%Initialization at $\ell = 1$:
$P^A(R_a, R_b) := m^A(\mathcal{C}(1))$
$P^B(R_a, R_b) := m^B(\mathcal{C}(1))$
$P^{A\cup B}(R_a, R_b) := m^{A\cup B}(\mathcal{C}(1))$
%Fusion of all the criteria
for $\imath = 2$ **to** P

$$P^A(R_a, R_b) = \frac{m^A(\mathcal{C}(\imath))P^A(R_a, R_b) + P^A(R_a, R_b)m^{A\cup B}(\mathcal{C}(\imath)) + m^A(\mathcal{C}(\imath))P^{A\cup B}(R_a, R_b)}{1 - (P^A(R_a, R_b)m^B(\mathcal{C}(\imath)) + m^A(\mathcal{C}(\imath))P^B(R_a, R_b))}$$

$$P^B(R_a, R_b) = \frac{m^B(\mathcal{C}(\imath))P^B(R_a, R_b) + P^B(R_a, R_b)m^{A\cup B}(\mathcal{C}(\imath)) + m^B(\mathcal{C}(\imath))P^{A\cup B}(R_a, R_b)}{1 - (P^A(R_a, R_b)m^B(\mathcal{C}(\imath)) + m^A(\mathcal{C}(\imath))P^B(R_a, R_b))}$$

$$P^{A\cup B}(R_a, R_b) = \frac{m^{A\cup B}(\mathcal{C}(\imath))P^{A\cup B}(R_a, R_b)}{1 - (P^A(R_a, R_b)m^B(\mathcal{C}(\imath)) + m^A(\mathcal{C}(\imath))P^B(R_a, R_b))}$$

end

Finally, the similarity measurement between regions R_a and R_b retained is $\kappa(R_a, R_b) \pm \Delta\kappa(R_a, R_b) \in [0, 1]$ such as :

$$\begin{cases} \kappa(R_a, R_b) := P^A(R_a, R_b) \\ \Delta\kappa(R_a, R_b) = P^{A\cup B}(R_a, R_b) \end{cases}. \tag{4.17}$$

4.5 Summary

In this chapter we have proposed some descriptors for the characterization of texture patterns. They are based on a representation of the detail coefficients (and eventually on the approximation component) of a wavelet decomposition. As for the approximation part, it can be useful if one compares patterns in similar conditions (same image for instance) but this component is often not used when we deal with images of different sensors.

We have assumed that the distribution of the coefficients follows a generalized gaussian density and this distribution can therefore be characterized only with two parameters related to the scale and the shape.This drastically reduces the size of the descriptor. In addition, the associated uncertainties related to the fitting of each GGD are extracted.

We have introduced a way to compare regions identified by the proposed descriptors. This relies on similarity measurements (Kullback-Leibler) from which we define mass functions that are fused together. It results in a unique similarity criterion with an associated uncertainty.

In the next chapter we present applications using such descriptors.

Chapitre 5

Application to various remote sensing problems

Sommaire

5.1 Overview

In this chapter we apply the descriptors of the previous chapter to several open remote sensing problems : segmentation, classification, detection of fronts and estimation of the orientation of the digging for some agricultural parcels. It should be noted that the presented techniques can also be applied in other fields than remote sensing.

5.2 Segmentation of agricultural parcels

A very important panel of methods is available for segmenting an image [Pal 1993] and this task is a crucial step in many computer vision problems. As for the Very High Spatial Resolution (VHSR) remote sensing images, a large amount of approaches has already been proposed and the reader can refer to [Carleer 2005, Dey 2010] for an overview. Due to the complexity and the variety of the input data, each approach is often devoted to a specific kind of imagery. In many practical applications, researchers or engineers use commercial multi-resolution segmentation softwares to extract regions at different scales based on several consistency criteria learned on training samples. Despite the efficiency of such approaches, this requires some features selection and thresholds to tune the classifier

[Schiewe 2001]. As a consequence an expert knowledge is needed and this makes impossible the generalization of such a process for various types of data.

We have proposed an unsupervised segmentation adapted to gray-scale images which requires few input parameters and produces regions of different sizes and different shapes. It is devoted to gray-scale images in order to process any kind of optical image and to be as transposable as possible. The idea consists in performing in a first step an over-segmented map where the objects are merged in a second step, according to the criterion presented in chapter 4.

The preliminary segmentation step is based on the combination of a wavelet transform and a watershed segmentation algorithm. This method has been introduced by [Jung 2007, Kim 2003]. We have been based on such approach since it is simple to implement and it detects properly the regions edges. Nevertheless it remains over-segmented objects, especially when one is dealing with highly textured pattern, like those included in VHSR remote sensing images. It is then of prime importance in a second step to merge similar regions. This is presented in the two next paragraphs.

5.2.1 Previous step : wavelet watershed segmentation

Here we rely on a watershed associated to the detail cœfficients at a given resolution of the image [Jung 2007, Kim 2003]. The resolution level is chosen by the user. It is in practice related to the spatial resolution of the input data and corresponds to the limit of an "entity" that composes an object. For instance in the case of an agricultural parcel, we assume that this latter is composed of several textured patterns (i.e. entities) generated by the digging and the spatial organization of plants. The choice of the resolution level is such that a single pattern will appear as a more or less uniform object at the chosen resolution. As a consequence, the application of a watershed process makes sense.

As will be shown in the experimental part, such a process results in over-segmented regions that need to be merged. This is the scope of the next section.

5.2.2 Merging agricultural parcels

In order to organize the different regions issued from the watershed step , we use Region Adjacency Graph (RAG) [Sonka 1993]. This is an non-oriented graph where the nodes correspond to the regions centroids and the edges represent a common border between regions. For each nodes we evaluate the similarity between its connected regions. They are then fused if a similarity criterion is validated. When no regions can be fused, the process is stopped.

As already mentioned, for VHSR data, the texture is often a reliable descriptor. However for very small objects, like the ones often extracted with a watershed technique, the notion of texture is ambiguous since the spatial information is too poor. For these kind of patterns, we rather prefer to rely on their gray-level to evaluate their similarity :

$$d(R_a, R_b) = \sqrt{(M_a - M_b)^2}, \tag{5.1}$$

where M_a (resp. M_b) is the mean luminance of the region R_a (resp. R_b). The overall process consists then in performing a watershed segmentation, building a Region Adjacency Graph, merging small similar objets based on the criterion on (5.1) and merging large objects based on the criterion of the previous chapter. All details can be found in Antoine Lefebvre's PhD [Lefebvre 2011a]. This is summarized in figure Fig. 5.1. An example on a aerial photograph is displayed in figure 5.2. The subfigure (a) shows the output of our watershed segmentation, subfigure (b) corresponds to the merging of small elements whereas subfigure (c) depicts the

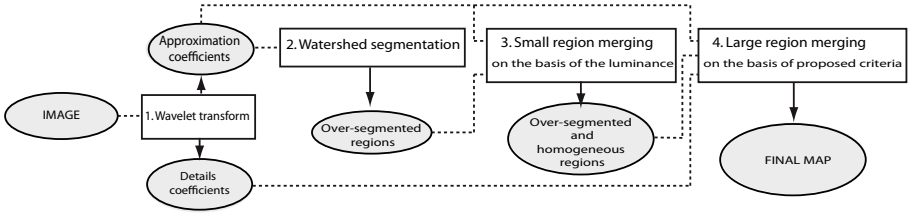

FIGURE 5.1 – **Unsupervised segmentation process** that consists in 2 merging step. Ellipses are data, rectangles are operations, arrows are outputs, dotted lines are input.

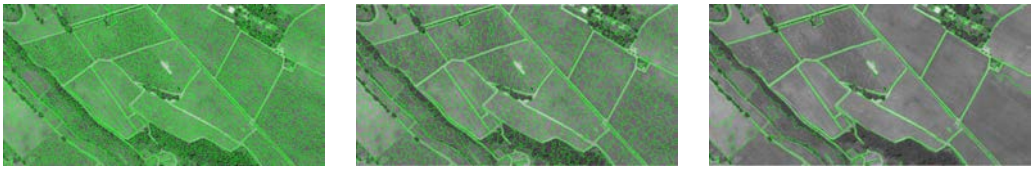

FIGURE 5.2 – **Segmentation of an aerial photograph.** (a) : results after the watershed segmentation (step 1) ; (b) : results after the merging of small entities ; (c) : results after the merging of similar objects

final segmentation where similar objects have been merged following the presented method. This example highlights its efficiency. We indeed observe that the watershed segmentation detects accurately the edges of each geographical entities but provides over-segmented objects. In a step forward, small similar objects from a luminance point of view are merged and the segmentation in (b) is generated. Lastly, the proposed merging step based on the criterion (4.17) of the previous chapter allows to separate the geographical entities according their texture and intensities. On this example, the ability to merge highly textured patterns of the different vineyards and roads is demonstrated : some large regions, fitting correctly with the edges of each vine plots, associated with long and thin regions representing roads, are extracted. More experiments can be seen in [Lefebvre 2010c, Lefebvre 2011a].

5.3 Estimation of the orientation of textured patterns

5.3.1 Problematic and related works

Here we are interested in the estimation of the dominant orientation of textured patterns that appear in a number of images. The applications are numerous (remote sensing but also biology or natural sciences for instance). In remote sensing, the main orientation of agricultural parcels often indicates relevant properties with regards to the topology and the underlying soil. Among the existing approaches related to orientation estimation, one can roughly classify them into gradient-based [Freeman 1991, Germain 2003, Le Pouliquen 2005, Michelet 2007] and spectral-based approaches [Jafari-Khouzani 2005, Josso 2005]. Techniques of the first family extract an orientation vector at each location of the image, which is not desired in our application since we rather prefer to extract a single vector representing the orientation of a whole object. Most of methods of the second family fail when multiple and sometimes non-rectangular objects occur in a single image. As a matter of fact, they are all based on the Fourier transform and the lack of space informa-

tion prevents from the localization of any structured pattern. We then propose to rely on wavelets to solve this problem.

5.3.2 Proposed solution

The strategy is based on the maximization of a criterion that deals with the coefficients enclosed in the different bands of a wavelet decomposition of the original image. More precisely, we search for the orientation that best concentrates the energy of the coefficients in a single direction (chosen as vertical here) :

$$\begin{cases} \widehat{\theta} = \max_{\theta} \left(\mathcal{E}(\boldsymbol{\mathcal{D}}, \{I_\theta\}) \right) = \left\{ \theta | \mathcal{E}(\boldsymbol{\mathcal{D}}, \{I_\theta\}) = \mathcal{E}_{max} \right\}, \text{ where} \\ \mathcal{E}(\boldsymbol{\mathcal{D}}, \{I_\theta\}) = \sum_{\jmath=0}^{J} \left(\boldsymbol{\mathcal{D}}(V_\theta^\jmath, H_\theta^\jmath) + \boldsymbol{\mathcal{D}}(V_\theta^\jmath, D_\theta^\jmath) \right). \end{cases} \tag{5.2}$$

where $H_\theta^\jmath$ (resp. $V_\theta^\jmath, D_\theta^\jmath$) represents the horizontal (resp. vertical and diagonal) band along the $\jmath^{th}$ level of the wavelet decomposition of an original pattern I rotated by an angle θ. Here, $\boldsymbol{\mathcal{D}}(\bullet_1, \bullet_2)$ is a symmetric similarity measurement between the distribution of the coefficients in the bands $\bullet_1$ and $\bullet_2$ based on the representation of the previous chapter. The relation (5.2) reaches its maximum for the angle θ that corresponds to the rotation required to align the main orientation of the analyzed pattern to the vertical axis.

The way we optimize the function in (5.2) is detailed in [Lefebvre 2010b, Lefebvre 2011a]. It should be noted that the proposed technique is able to evaluate whether a given texture is oriented or not. This is done using the different values reached by $\mathcal{E}$ during the optimization process (that are connected to an isotropy degree).

5.3.3 Some results

The articles in [Lefebvre 2010a, Lefebvre 2010b, Lefebvre 2011a] contain complete qualitative and quantitative evaluations of the technique and comparison with other ones. Here we present a snapshot of result. We have estimated the orientation angle on a set of 150 pre-segmented patterns extracted on remotely sensed images of $60cm$ resolution issued from different sensors : very high spatial resolution data, grey scale aerial photographs and panchromatic satellite images. Five classes of land coverage have been distinguished : meadow, bare soil, forest, cereals, and vineyard. Among them, bare soils, meadows and forests are considered as "non-oriented" (or isotropic) textures whereas the cereals and vineyards are "oriented" (or anisotropic).

First, the rate of correct classification between oriented and non-oriented textures is 96.7% with our approach whereas it is of 82.7% with the approach in [Josso 2005]. For some important differences in the estimation of angles, we have plotted in figure 5.3 the re-oriented patterns along the vertical axis with both estimated angles. From these figures, it is clear that the accuracy is more important with the proposed technique since our re-oriented patterns fit better with the vertical axis. We also have applied the framework to estimate the orientation at each location of PTV (Patricle Tracking Velocimetry) images. This technique of visualization enables to observe the motion of particles in a fluid flow using their trace in images, yielding oriented patterns (cf figure FIG. 5.4(a)). The process has been applied on a patch around each position. On the estimated angles of figure 5.4(b), it is very promising to observe that they are consistent with the flow where the different areas are accurately extracted (disturbance just after the obstacle and homogeneous flow outside).

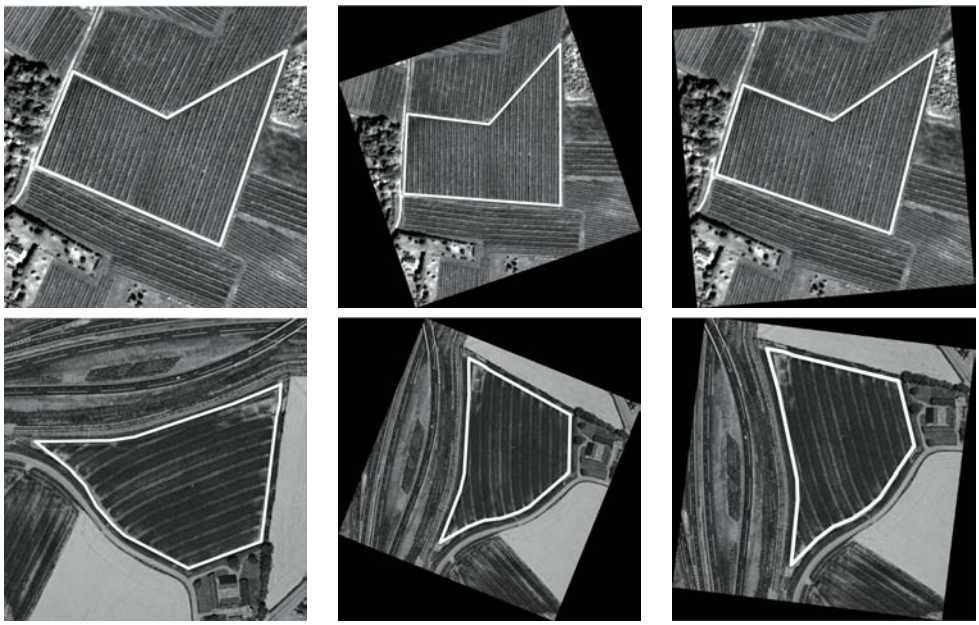

(a) (b) (c)

FIGURE 5.3 – **Reorientation of the patterns** for some agricultural parcels (top and bottom). (a) represents the input textures ; (b) rotation of (a) along the vertical axis according to the proposed method ; and (c) rotation of (a) according to [Josso 2005]

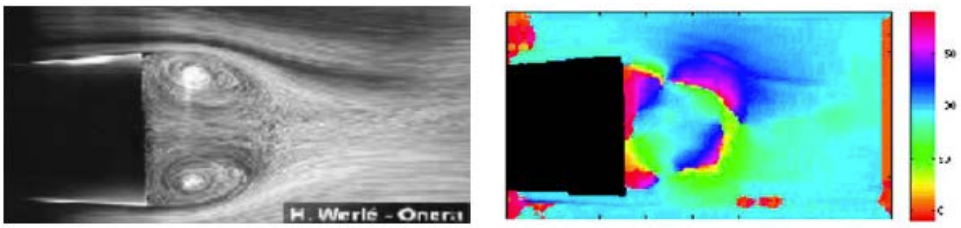

FIGURE 5.4 – **Estimation of the orientation on PTV (Particle Tracking Velocimetry) images.** Left : a PTV image ; right : estimated angles at each location

FIGURE 5.5 – **Supervised segmentation** Two VHSR images from 1978 and 2001, the associated segmentation and the legend.

5.4 Classification and supervised segmentation of agricultural parcels

Classification in remote sensing is a key issue and has been widely studied over the last decades (see for instance [Benediktsson 1990, Bruzzone 2009, Bruzzone 2010, Chanussot 2010, Heermann 1992, Tison 2007] for applications and reviews related to remote sensing).

With the framework of section 5.2, it is possible to design in an easy way an object classification technique (and therefore a supervised segmentation if one classifies the objects issued from the watershed segmentation of section 5.2.1). Based on samples, any class can be characterized using the descriptors of previous chapter (relations (4.5) and (4.6)) and compared with other objects using the proposed criterion in (4.17) of the previous chapter. However for agriculture applications, a recurrent problem when one performs supervised segmentation comes from the digging which in general is different when samples are taken at different locations. As a consequence, two agricultural parcels with the same land cover but different diggings are likely to be labelled in different classes. We then propose to reorient all the pre-segmented objects in a common axis using the approach of the previous section.

Some results are depicted in figure 5.5 for 6 classes related to woodlands, bare soil, vegetation, roads, builded areas and water. The training step was the same for both images. It is interesting to outline that the overall accuracy is good and we observe that such approach is able to efficiently segment and classify objects of various shapes (linear or not), textures and at various scales. More examples with detailed quantitative comparisons are in [Lefebvre 2011a, Lefebvre 2011b]. Let us now turn to the identification of texture fronts.

5.5 Detection of sea breeze fronts

5.5.1 Problem of front detection and tracking

This study was motivated by the necessity to automatically detect the sea breeze fronts (see an example in figure FIG. 4.1(d)) that appears as a textured front in the images. Physically, the sea breeze is a wind issued from the contrast between sea and land surface temperatures. The onset of the sea breeze causes a sudden squall at the inland boundary of the sea breeze circulation, which is called the sea breeze front. The rising air near the sea breeze front often condenses and allows the development of clouds. Therefore, the sea

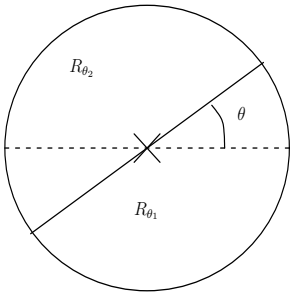

FIGURE 5.6 – **Regions R_{θ_1} and R_{θ_2}** depending on the angle θ for each location $\boldsymbol{x}$.

breeze front can be deduced from the appearance of a line of cumuliform clouds parallel to the coast and pushed inland by the sea breeze circulation. The identification of these cloud patterns in MSG images can be used to determine how far the sea breeze spreads into inland. From a climatic point of view, the sea breeze front moves according to the seasons and its diurnal evolution as well as its consequences on the local climate are not still completely known.

The difficulty to face here is that the sea breeze front does not appear clearly through a limit in terms of luminance but is rather characterized by the limit of two textured areas composed on the one side of a cloud-free region and on the other side of a zone with cumulus clouds. Therefore usual front extraction/characterization techniques, as for instance contrast-invariant image representations [Alvarez 1993, Monasse 2000] or approaches based on Lyapunov coefficients are inefficient here.

5.5.2 Proposed solution

We have proposed to solve this problem of edge detection by the definition of a potential map P related to the presence/absence of fronts on which a segmentation technique (active contour [Kass 1988] in our situation) is applied. At each location $\boldsymbol{x}$ of an image, we have computed the potential P such as :

$$P(\boldsymbol{x}) = \max_{\theta} \left\{ \kappa(R_{\theta_1}, R_f)\overline{\kappa(R_{\theta_2}, R_f)} + \overline{\kappa(R_{\theta_1}, R_f)}\kappa(R_{\theta_2}, R_f) \right\} \tag{5.3}$$

where

- θ is an angle ;
- R_f is a region, pre-selected once by the user, that is representative of the area of cumulus that limits the sea breeze penetration ;
- R_{θ_1} and R_{θ_2} are two adjacent regions around location $\boldsymbol{x}$ delineated with the angle θ (see the illustration in figure 5.6) ;
- $\kappa(R_{\theta_\ell}, R_f)$, $\ell = \{1, 2\}$ is the similarity criterion between regions R_{θ_ℓ} and R_f defined in (4.17) and
- $\overline{\kappa(R_{\theta_\ell}, R_f)} = 1 - \kappa(R_{\theta_\ell}, R_f) - \Delta\kappa(R_{\theta_\ell}, R_f)$ is the belief in the fact that region R_{θ_ℓ} is different than region R_f

This potential extracts the maximum value stating that the region R_{θ_1} (resp. the region R_{θ_2}) belongs (resp. does not belong) to the region R_f or conversely. It is therefore related to the presence/absence of fronts delineated by an area similar to R_f. More details, and in particular the way one can deal with transparency, can be found in [Corpetti 2010]. Once the potential P is estimated, we have embed it in an active contour framework [Kass 1988]

eventually using minimal paths (if the end points are known due to physical limitations) [Cohen 1997] in order to extract the fronts.

5.5.3 Some results

The figure Fig. 5.7 (a) represents an image issued from the visible channel of the Meteosat Second Generation satellite on the Brazilian coast where we have superimposed the initial snake (at the coast line). One can observe the sea breeze front on the north of the image. Figure 5.7 (b) is a detail of fig. 5.7 (a) to accurately observe the texture border and some clouds which create a phenomenon of transparency. To compare with usual techniques, we present in 5.7 (c-d) the final snake obtained with the classic potential term $P(\boldsymbol{x}) = \lambda \|\boldsymbol{\nabla} I(\boldsymbol{x})\|$ based on the norm of the gradient of the luminance to detect edges. The associated potential P is shown in 5.7 (e). The Fig. 5.7 (c) (resp. Fig. 5.7 (d)) is the front extracted when the first and last points are unknown (resp. known). The corresponding final snakes obtained by the proposed method are represented in 5.7(f,g) as well as the associated potential function in a narrow band around the final snake in 5.7(h). On this real example, it appears clearly that our potential map is consistent. As a consequence, the resulting fronts are correctly segregated in both situations (known and unknown limit points). The same consequence does not hold with a classic approach (fig 5.7 (c,d)) where the final contour is attracted by high-gradient areas and it is obvious that they do not correspond to any physical front. This experience shows our method is efficient to identify the sea breeze fronts in meteosat images. We also have tested the approach for general texture data. We aim at detecting the central texture pattern of figure 5.8 (a) which exhibits an object on two different backgrounds. This original synthetic image has been blurred by transparency on three areas at the boundaries. This is represented in Fig. 5.8 (d) in which the initial contour is superimposed. Figure 5.8 (b) shows the final snake obtained with our approach and Fig. 5.8 (e) represents the proposed potential function P computed on the whole image. To compare with usual active contour approaches, we have depicted in figure 5.8 (c) the final snake obtained with a classic potential term based on the norm of the gradients, this latter being represented in figure 5.8 (f). It is interesting to observe that the proposed potential clearly highlights the boundaries of the desired structure and consequently, the final snake has correctly extracted the region of interest. At the opposite, a usual potential term attracted by high gradients fails in identifying the expected border. Quantitative evaluations and other experiments can be found in [Corpetti 2010].

5.6 Summary

In this chapter, we have successfully design techniques based on the descriptors presented in chapter 4 devoted to various tasks : segmentation, classification, estimation of the orientation, front detection. All these experiments prove that such descriptors are sufficiently generic to provide reliable solutions for remote sensing data and texture analysis.

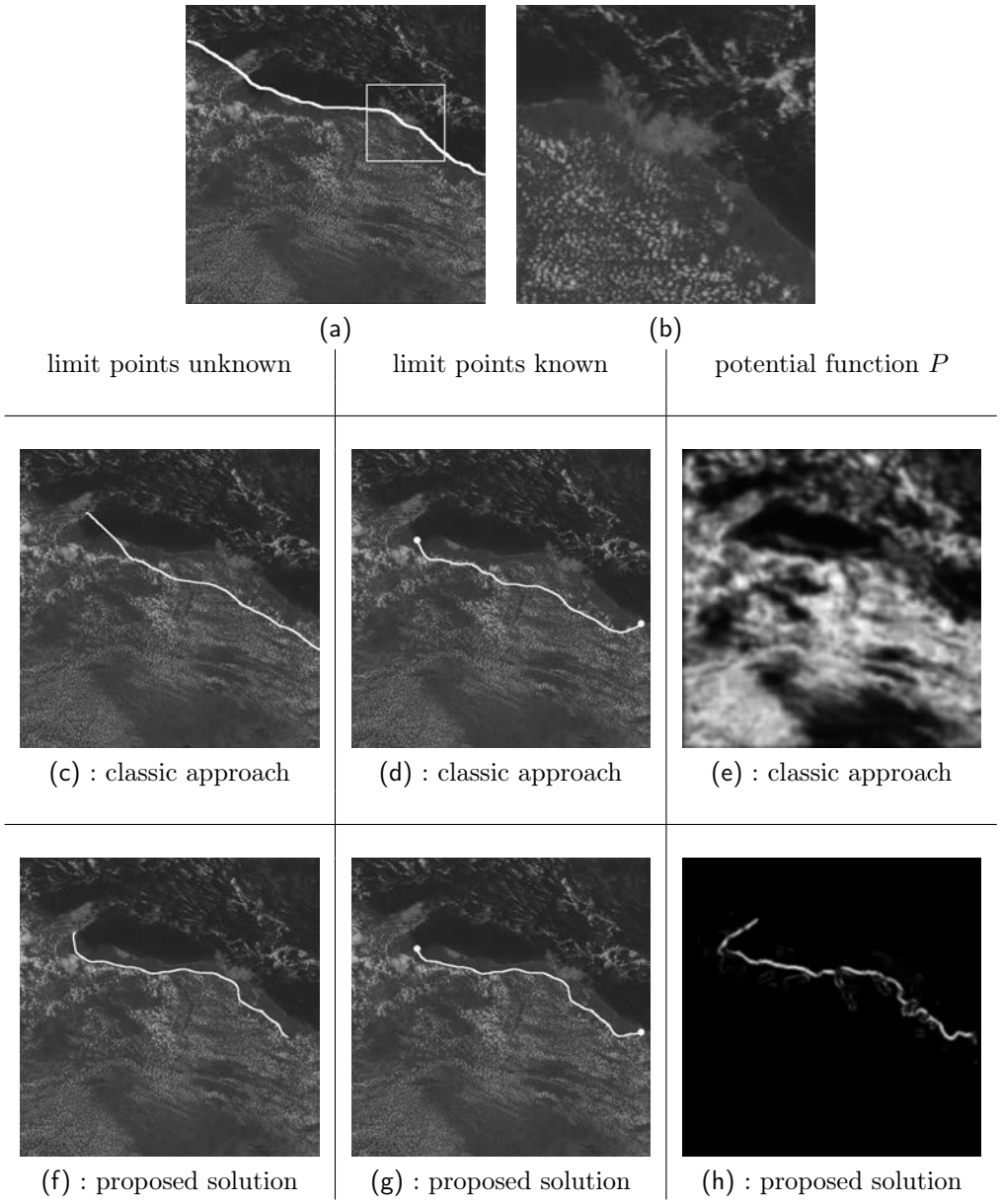

FIGURE 5.7 – **Sea breezee front detection** : (a) : original satellite image with the initial snake ; (b) : detail of the area in the square of (a) where one can observe that a cloud disturbs the visualization of the front ; (c,f) : the final contour obtained respectively with a classic approach (based on the norm of the gradients) and our technique when the limit points are unknown ; (d,g) : same as (c,f) when the limit points are known ; (e,f) : associated potential maps

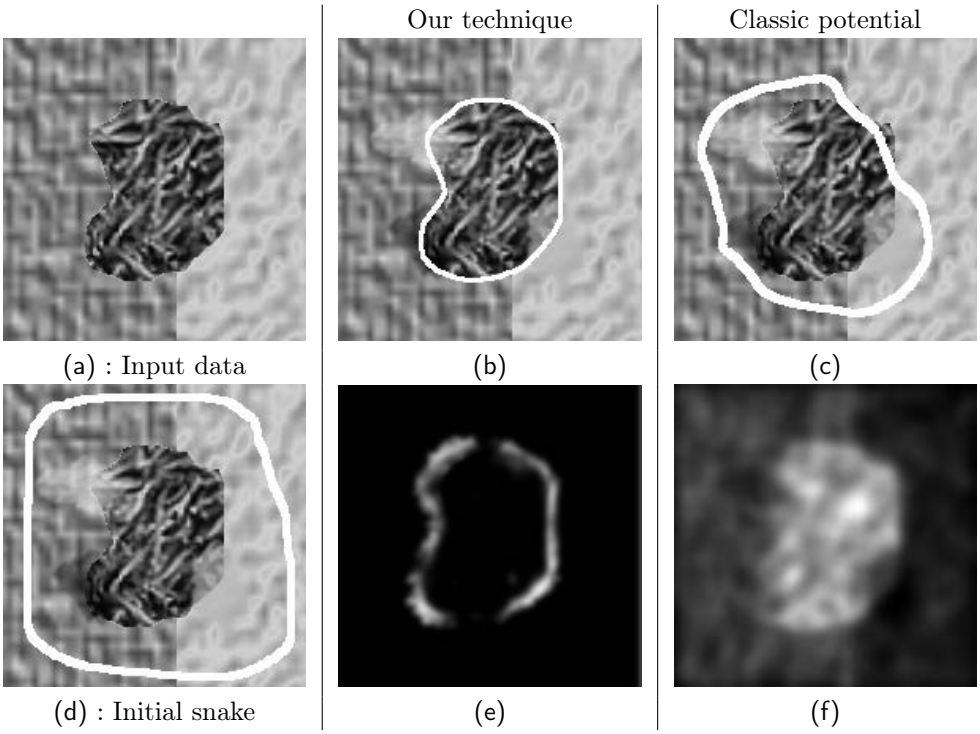

FIGURE 5.8 – **Synthetic texture example** : (a) : original image ; (d) : the initial snake superimposed to the blurred image ; (b) : the final contour obtained with the proposed approach ; (e) : the associated potential scalar ; (c) : the final contour extracted with a usual potential $P(\boldsymbol{x}) = \lambda \|\boldsymbol{\nabla} I(\boldsymbol{x})\|$, this latter being in (f).

Chapitre 6

Change detection

Sommaire

6.1 Overview

This chapter is concerned with "structural" change detection in pair of images. This is a challenging and open problem in computer vision in general and in remote sensing in particular since the difficulties stemming from the confusion between *real changes* (depending on the objects/structures inside the images) and *visual changes* (observed through the difference in terms of image luminance) are numerous. Many applications are concerned with this crucial task including video surveillance, event detection and of course remote sensing [Bosc 2003, Collins 2000, Lu 2004, Radke 2005].

From two images of possibly different nature (different sensors in remote sensing, different lighting conditions or viewpoint for instance), the problem consists in identifying the areas where a *structural* change has appeared. Such changes can be generated with the apparition/disparition of objects, cars, man-made structures (roads, bridges, buildings, houses, industries, ...), different exploitation of the agriculture (fusion/merging of fields, change of type of culture), etc. They are generally caused by changes of rhythms and patterns ranging either from abrupt (on large areas) to subtle (small regular surfaces like agricultural parcels or urban sprawl) differences. They obviously differ from the observed alterations in terms of image luminance in the sense that these latter include differences due to various lighting conditions, view angles, shadows, camera or scene noise which do not correspond to the real semantic changes. Moreover the intrinsic variability inside a specific object introduces some bias that makes the change recognition task extremely difficult.

Applications of change detection techniques are numerous. In video-surveillance, identifying new people, cars, objects, ... in a scene is naturally of prime importance. In biology, the

changes endured by proteins help the understanding of some phenomena [Pecot 2009]. In remote sensing, because of the large time rate between two satellite images, highlighting the urban or agricultural changes from two images acquired several years apart is of prime importance for environment monitoring. Several techniques have already been proposed in that context (see in particular [Radke 2005]) for medium and high resolution data (roughly from $250m$ to $1m$ resolution). However since one decade, the images provided by new VHSR remote sensors have generated a valuable source of data and opened a wide domain of research concerning their analysis. The very precise nature of the embedded information requires indeed new developments for recognition, detection, classification, ... and in particular change detection of sensed objects. At the moment, most of the change detection methods routinely used by experts on remote sensing data (such as [Lu 2004, Radke 2005, Ridd 1998] applied in urban and peri-urban areas) have been developed to highlight abrupt changes of land use from remote sensing images at low or medium resolution using almost exclusively the spectral response of the pixels. This performs efficiently when such spectral response is a reliable descriptor of the different objects. Obviously this is not sufficient with VHSR data or with any kind of images whose embedded objects exhibit heterogeneous luminance values.

Historically the change detection problem was faced using a thresholding on the image luminance differences. Such natural approach is efficient but is nevertheless strongly related to the value of the considered thresholds (see [Otsu 1979, Rosin 2002]) and appears limited for textured objects or structures with high internal variability. More advanced methods have been developed as for example predictive and patch-based models exploiting the spatial (and temporal when more than two images are available) relationships between points [Aach 1993, Kervrann 2009, Pecot 2008], statistical hypothesis tests [Hsu 1984] or texture based similarity criteria [Lefebvre 2009]. Post classifications techniques on pre-segmented objects have also been efficiently designed in [Bruzzone 2002, Deer 2002]. We refer the reader to the very complete reviews of change detection algorithms in [Lu 2004, Radke 2005] for more information.

We have worked on several directions. As we already have proposed, in section 5.4 of the previous chapter, some tools for the classification of objects, it is then obvious that from two classified images, one can easily qualify the changes. This is illustrated in figure Fig. 6.1 from the images of Fig. 5.5 where we have qualify 4 types of changes : no changes (between artificial surfaces or not), surfaces that became artificial and delayering of soils. However such kind of solution is not optimal since errors of the segmentation and the classification steps for both images contribute to the uncertainty of the final result. We then suggest in sections 6.3 and 6.4 more advanced techniques that directly deal with images without pre-segmentation/classification steps.

Before describing these techniques, the next section proposes a change vector based on the descriptors of chapter 4 that enable to qualify the nature of the change between two (non classified) objects.

6.2 Change detection using pre-segmented maps

The goal of this section is to provide measurements able to qualify the different type of changes between two pre-segmented maps. In practice these segmentations can either be provided by specialists (from expert knowledge on soils for instance) or extracted with an image processing tool (as the one proposed in section 5.2 or using a commercial software).

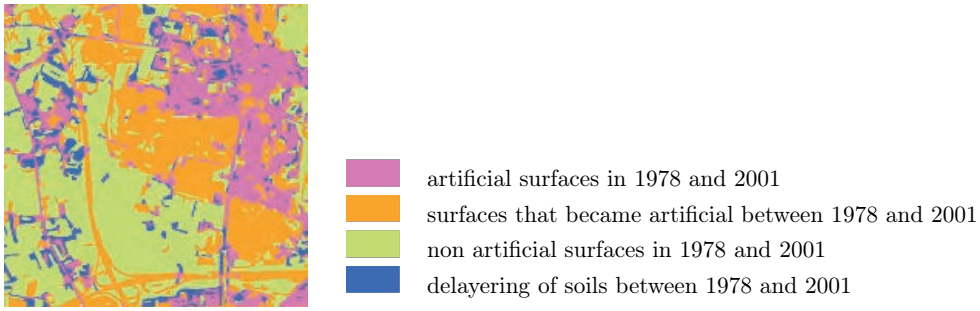

FIGURE 6.1 – **Change detection using pre-classified objects** on the two images of FIG. 5.5 between 1978 and 2001

6.2.1 Measurements to qualify the changes from segmented objects

Here we consider that the luminance information is irrelevant since the images are issued from sensors with different properties. Only the texture is required for characterizing the changes. We perform a wavelet decomposition of each image and each pre-segmented object $\mathcal{O}_a$ is characterized by a vector $\mathcal{T}_a = (\alpha_{a,j,Z}, \beta_{a,j,Z})$ where $(\alpha_\bullet, \beta_\bullet)$ are scale and shape parameters related to the GGD (see relation (4.4)) that characterize the distribution of the wavelet coefficients (the reader can refer to section 4.2 of chapter 4 for more details). From two entities $(\mathcal{O}_a, \mathcal{O}_b)$, characterized with $(\mathcal{T}_a, \mathcal{T}_b)$, the goal is then to identify the nature of the change. To that end we rely on the values of the Kullback-Leibler dissimilarities between each GGD characterized with $(\alpha_{a,j,Z}, \beta_{a,j,Z})$ and $(\alpha_{b,j,Z}, \beta_{b,j,Z})$ and computed using relation (4.12).

In the field of change analysis for remote sensing data, it is assumed that a change is characterized by its scale (*small-scale*, *large-scale* or both), its intensity and can in addition be *subtle* or *abrupt*. To identify the nature of the observed change, we then propose to define a *change vector* $\mathcal{D}$ composed of 5 indicators :

1. the average for the overall KL in all bands of the decomposition : this discriminates an abrupt change to a subtle one ;
2. the ratio between the dissimilarity of one coefficient and the sum of others : this highlights the components that best measure the differences between textures ;
3. the standard deviation of the dissimilarities over the different scale levels (j variable) for a same kind of detail (horizontal, vertical or diagonal, i.e. Z is fixed) : this detects changes occurring only in some scale levels ;
4. the standard deviation of the dissimilarities of a same scale level (j fixed) in the 3 types of detail (Z variable) : this detects changes that occur only in a particular direction ;
5. The degree of isotropy issued from section 5.3 : this discriminates changes from homogeneous to oriented changes.

All the components of $\mathcal{D}$ enable to highlight the different changes. For instance, a large-scale change will exhibit dissimilarities in the detail bands that increase when the scale increases, as illustrated for diagonal details in figure FIG. 6.2. In this particular example, the 3^{rd} component of $\mathcal{D}$ brings out the change.

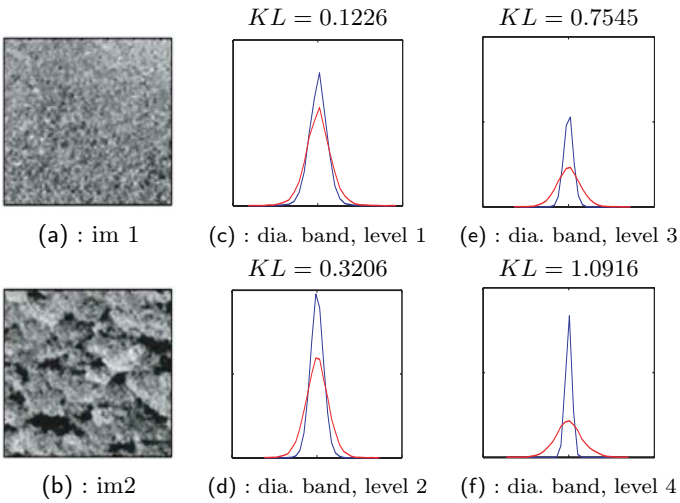

FIGURE 6.2 – **Abrupt change between two homogeneous textures**. The amplitude of the KL dissimilarity grows with the scale analysis of a given detail band (diagonal here)

6.2.2 Some results

To validate such change vector, we have characterized changes on all pairs of images issued from a benchmark of 2400 agricultural parcels extracted on airborne images with a spatial resolution of 50cm. We identified six types of textures that correspond to different land use and five classes of changes are possible :

1. large-scale, abrupt and oriented-change (example : transition from cereals to a – sowed or not – meadow) ;
2. large-scale, subtle and oriented-change (example : transition from a meadow to sowed meadow) ;
3. change between two homogeneous textures with the same scale (example : transition from corn to meadow) ;
4. large-scale and small-scale, abrupt and oriented-change (example : transition from a sprayed corn to meadow) ;
5. large-scale change between two homogeneous textures (example : transition from a meadow to a forest) ;

The classification of changes is performed using decision trees [Breiman 1984, Friedl 1997]. The vector $\mathcal{D}$ was used to compare the textures. For each class, a set of 30% of the samples is chosen for the construction of the tree and 70% is used for the evaluation. The table 6.1 exhibits the rate of good detection for each of the 5 types of changes previously mentioned. As one can observe, the rate of good detection is very high. In addition, we have depicted the most discriminative component of $\mathcal{D}$ corresponding to the change. This experience on a real benchmark proves the ability of the proposed change vector to accurately discriminate the textures and to analyze their changes.

We also have characterized changes on a real situation between the two images of figure FIG. 6.3. The first one is a scanned aerial photograph dating from 1970. Its noise is high and its spatial resolution quite low ($\approx 1m$). The second image is issued from the Quickbird satellite and was acquired in 2003 with $61cm$ resolution. We are interested on three kind of particular changes : 1– "subtle agricultural changes" (changes in terms of type of culture) ;

Type of Change	Rate good det.	Main comp. of $\mathcal{D}$
1	92%	1–5
2	98%	1–2–4–5
3	86%	1–5
4	98%	1–2–5
5	93%	3

TABLE 6.1 – Rate of good detections and main component of $\mathcal{D}$ exploited for the change classification on agricultural benchmarks.

(a) : 1970 (b) : 2003 (c) : change map

FIGURE 6.3 – **Change detection** (a–b) : input images ; (c) : the change detection. Yellow : change of cultures ; Blue : abrupt changes ; Red : new roads.

2– "abrupt changes" (from culture to forest, farms, orchard or inversely) ; 3– new roads. To identify these changes, the 3^{rd} and 4^{th} components of $\mathcal{D}$ (changes only in some scales and oriented changes) were used to isolate the class 1. Class 2 has been detected with the 2^{nd} and 3^{rd} components (scale changes associated or not to subtle changes) and class 3 with the 2^{nd} and 4^{th} components (scale and oriented changes). Results are shown on figure 6.3(c). One can observe that the different changes have correctly been identified, despite the fact that the input images were very different in terms of quality and resolution.

These experiments demonstrate the ability of our vector $\mathcal{D}$ to discriminate the type of changes on pre-segmented objects images. The reader can find quantitative evaluations in [Lefebvre 2009, Lefebvre 2011a]. In the next section we focus on a more general situation where pre-segmentations are not available.

6.3 Change detection without pre-segmented maps using patches of various size

6.3.1 Overview

We have proposed a technique for detecting changes in various kind of imagery. This is formalized as the extraction of a binary map $\boldsymbol{\ell}(\boldsymbol{x}) \in \{0, 1\}$ (also named "change mask") that classifies the changed ($\boldsymbol{\ell}(\boldsymbol{x}) = 1$) and non-changed ($\boldsymbol{\ell}(\boldsymbol{x}) = 0$) regions between two input images $I_t(\boldsymbol{x})$ and $I_{t+1}(\boldsymbol{x})$. This section briefly presents the core of the technique but more details regarding the specific pre-processing step, the construction of change maps and minimization issues can be found in [Gong 2010].

The approach relies on a Bayesian formalism : we aim at maximizing the posterior probability of a label configuration $\boldsymbol{\ell}$ depending on the image data I and some models $\mathcal{M}$ creating a link between the data I an the change label $\boldsymbol{\ell}$:

$$\mathcal{P}(\boldsymbol{\ell}|I, \mathcal{M}) = \frac{\mathcal{P}(I|\boldsymbol{\ell}, \mathcal{M})\mathcal{P}(\boldsymbol{\ell}|\mathcal{M})}{\mathcal{P}(I|\mathcal{M})} = \frac{\text{likelihood} \times \text{prior}}{\text{evidence}}. \tag{6.1}$$

In general the model $\mathcal{M}$ is fixed whatever the data are and the denominator of the previous relation has no influence. It can then be ignored in the optimization process. Using Gibbs distributions to model the involved probabilities, the previous maximization equals to minimize a cost function composed of a data term and a prior smoothing.

In this work, the global-cost function embeds several criteria issued from statistics on local patches. The optimization is performed using an efficient min-cut/max-flow strategy. The energy to minimize consists in N thresholding of value τ_i on N change maps $\mathcal{X}_i$, $i = \{1, ..., N\}$ (related to the change measurements between the two images) and a simple smoothing term :

$$E(\boldsymbol{\ell}(\boldsymbol{x}), I(\boldsymbol{x})) = \sum_{\boldsymbol{x} \in \boldsymbol{X}_t} \sum_{i=1}^{N} k_{\alpha_i} \phi_1(\mathcal{X}_i(\boldsymbol{x}), \tau_i, \boldsymbol{\ell}(\boldsymbol{x})) + k_\beta \sum_{(\boldsymbol{x},\boldsymbol{y}) \in \mathcal{V}} \phi_2(I, \boldsymbol{\ell}(\boldsymbol{x}), \boldsymbol{\ell}(\boldsymbol{y})), \tag{6.2}$$

where $\boldsymbol{X}_t$ is the image grid, $\mathcal{V}$ a neighborhood system, k_{α_i} and k_β are coefficients, ϕ_1 is a function related to the thresholding (i.e. ϕ_1 is minimal if $\mathcal{X}_i(\boldsymbol{x}) > \tau_i$ (resp. $\mathcal{X}_i(\boldsymbol{x}) < \tau_i$) and $\boldsymbol{\ell}(\boldsymbol{x}) = 1$ (resp. $\boldsymbol{\ell}(\boldsymbol{x}) = 0$)) and function ϕ_2 is a compactness prior, eventually equipped with a strategy to alleviate over smoothing effects around edges in the different change maps. The value of the thresholds τ_i can in practice be automatically fixed for instance using cross-validation but we observed quite stable results with natural values fixed by hand. The next section coarsely introduces the change maps $\mathcal{X}_i$ we defined on patches.

6.3.2 Change maps

Before describing the change maps, we indicate a way to represent the images. This point of view enables to define a strategy for the estimation of the size of the patches.

Image representation

As already done, we assume that the grid $\boldsymbol{X}_t$ on which is defined the image I_t follows a so-called Îto process defined as :

$$d\boldsymbol{X}_t = 0 \cdot dt + \boldsymbol{\Sigma}(t, \boldsymbol{X}_t) d\mathbf{B}_t = \boldsymbol{\Sigma}(t, \boldsymbol{X}_t) d\mathbf{B}_t, \tag{6.3}$$

where $d\mathbf{B}_t$ is a standard Brownian motion of $\mathbb{R}^2$, $\boldsymbol{\Sigma}$ a 2×2 covariance matrix and $d\boldsymbol{X}_t = \boldsymbol{X}_{t+1} - \boldsymbol{X}_t$ represents the difference between the grid positions at time t and $t+1$. Roughly, since the deterministic part of relation (6.3) vanishes, we assume that the grid of points $\boldsymbol{X}_t$ and $\boldsymbol{X}_{t+1}$ on which are defined I_t and I_{t+1} are identical up to the "uncertainty" $\boldsymbol{\Sigma}(t, \boldsymbol{X}_t)$. High values (resp. small) of this latter parameter are related to large (resp. small) objects. Each point is free to move anywhere inside this uncertainty area corresponding to the object, as illustrated in figure 6.4.

A possible way to represent the stochastic part of (6.3) is to use an isotropic uncertainty variance map $\sigma(X_t)$:

$$\boldsymbol{\Sigma}(\boldsymbol{X}_t, t) d\mathbf{B}_t = \mathrm{diag}(\sigma(\boldsymbol{X}_t)) \otimes \mathbb{I}_2 d\mathbf{B}_t, \tag{6.4}$$

where $\mathbb{I}_2$ is the (2×2) identity matrix and $\otimes$ denotes the Kronecker product. The differential of any continuous function f defined on such a diffusion process has already been introduced in chapter 1 (section 1.5) and is reached with the Îto formula. Applied on the model grid described in (6.3) we get :

$$df(\boldsymbol{X}_t, t) = \left(\frac{\partial f}{\partial t} + \frac{1}{2} \sigma^2 \Delta f \right) dt + \sigma \nabla f \cdot d\boldsymbol{B}_t. \tag{6.5}$$

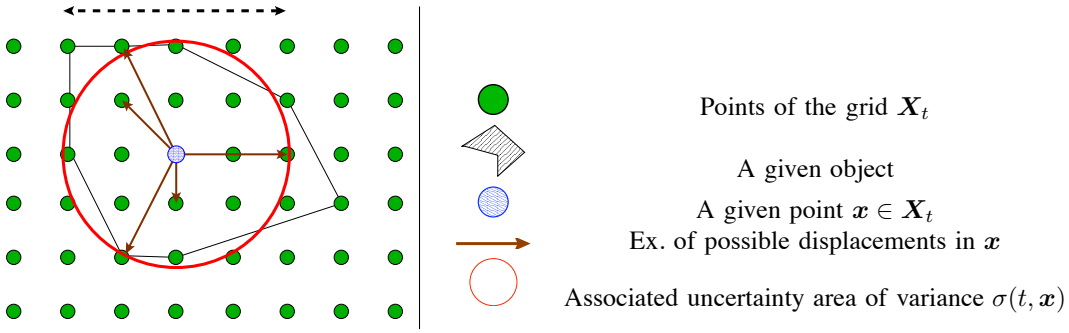

FIGURE 6.4 – **Uncertainty related to the grid points** of the images I_t and I_{t+1}. Any point $\boldsymbol{x} \in \boldsymbol{X}_t$ is free to move in its "uncertainty area" related to its underlying object without modifying the content of any change criteria defined from the images

If one assumes the image luminance I as a continuous function, this latter relation holds for $f = I$ and we get

$$dI(\boldsymbol{X}_t, t) = \left(\frac{\partial I}{\partial t} + \frac{1}{2}\sigma^2 \Delta I \right) dt + \sigma \nabla I \cdot d\boldsymbol{B}_t. \tag{6.6}$$

In this relation, the deterministic part would in practice correspond to the difference of the two images (term $\partial I/\partial t$) up to some uncertainties (term $(\sigma^2 \Delta I)/2$). Its value is small when no changes appear and is large in presence of changes. This is a quite natural criteria enabling to highlight the changes. However in this work, instead of using criteria only based on the difference of images, we rather prefer to highlight the change areas using a set of N stochastic criteria $\boldsymbol{Z}_i$, $i = \{1, ..., N\}$ related to subtle and abrupt changes. Therefore, instead of using the relation (6.6) based on $dI(\boldsymbol{X}_t, t)$, we rather prefer to start from a relation of the type $\boldsymbol{Z}_i(dI(\boldsymbol{X}_t, t))$ where $\boldsymbol{Z}_i$ are functions allowing to measure the importance of specific changes from I. Assuming functions $\boldsymbol{Z}_i$ are linear (this assumption is discussed later in the document and in [Gong 2010]), we then have

$$\boldsymbol{Z}_i(dI(\boldsymbol{X}_t, t)) = \underbrace{\boldsymbol{Z}_i(I(\boldsymbol{X}_t, t), \sigma(\boldsymbol{X}_t))}_{\text{Deterministic part}} dt + \underbrace{\sigma \nabla \boldsymbol{Z}_i(I(\boldsymbol{X}_t, t))}_{\text{Stochastic part}} \cdot d\boldsymbol{B}_t. \tag{6.7}$$

Finally, the deterministic criteria $\mathcal{X}_i$ used in (6.2) to highlight the changes between images I_t and I_{t+1} are chosen as the expectation of $\boldsymbol{Z}_i$, yielding

$$\begin{aligned} \mathcal{X}_i &= E\left(\boldsymbol{Z}_i(dI(\boldsymbol{X}_t, t))\right) \\ &= \boldsymbol{Z}_i(I(\boldsymbol{X}_t, t), \sigma(\boldsymbol{X}_t)). \end{aligned} \tag{6.8}$$

In practice, for each $\boldsymbol{x} \in \boldsymbol{X}_t$, we decide to compute the value of $\mathcal{X}_i(\boldsymbol{x})$ on patches whose size is defined according to the uncertainty $\sigma(\boldsymbol{X}_t)$. Before describing the procedure to estimate $\sigma(\boldsymbol{X}_t)$, we briefly talk about the change maps.

Change maps

As for the content of the change maps $\mathcal{X}_i$, a large number is possible, depending of the nature of the changes one desires to extract. For instance each $\mathcal{X}_i$ can be issued from one component of the change vector $\mathcal{D}$ defined in section 6.2. However here in order to evaluate the principle of the technique, we only used three subtle change criteria (based on the

Kullback-Leibler distances between the detail coefficients in the 3 directions $Z = \{H, V, D\}$ of one level of a wavelet decomposition) and one abrupt change criteria based on a L_2-norm with information matrices, as in [Boulanger 2007].

Size of the patches

Statistics on patches are generally known to be reliable descriptors in many image processing problems. However a sensible point remains on the definition of the size of the patches which has a dramatic influence on the final result. We have proposed an original way to fix this key parameter. We assume that a consistent patch of half-size q should be related to $\sigma(\boldsymbol{x})$ in relation (6.7). Computing the quadratic variation of the relation (6.7) between t and $t+1$ and after several manipulations, one can estimate the size of the patch as :

$$\sigma(\boldsymbol{X}_t, t) = \sqrt{\frac{A^T b}{A^T A}} \quad \text{with} \quad \begin{cases} A = \left[|\nabla \mathcal{X}_1(\boldsymbol{X}_t))|^2, ..., |\nabla \mathcal{X}_N(\boldsymbol{X}_t))|^2\right]^T & \text{is a } N \times 1 \text{ vector and} \\ b = \left[\mathcal{X}_1^2(\boldsymbol{X}_t), ..., \mathcal{X}_N^2(\boldsymbol{X}_t)\right]^T & \text{is a } N \times 1 \text{ vector.} \end{cases} \tag{6.9}$$

Intuitively, such relation makes sense : when the position $\boldsymbol{x}$ is inside a large object, the change maps $\mathcal{X}_i$ should be more or less spatially consistent and therefore exhibit small gradients, which will enlarge the size of the patch. On the drawback, the gradient $\|\nabla \mathcal{X}_i(\boldsymbol{X}_t, t))\|$ at a position near a frontier will increase and generate a smaller patch size with relation (6.9). In the above relation both the numerator and denominator have to be defined using maps $\mathcal{X}_i$ (that require the values of $\sigma(\boldsymbol{X}_t)$). In addition as we have assumed that functions $\boldsymbol{Z}_i$ were linear which is not necessarily verified, we suggest a recursive process to fix $\sigma(\boldsymbol{X}_t)$ and thus estimate the maps $\mathcal{X}_i$ as follows :

Incremental technique for fixing $\sigma(\boldsymbol{X}_t)$ and $\mathcal{X}_i(\boldsymbol{X}_t)$
- Initializations :
  - $k = 1$;
  - Fix an uncertainty σ^1
  1. Compute all maps $\mathcal{X}_i^k$ for each i, $i = \{1, ..., N\}$ with a patch of size σ^k
  2. Estimate σ^{k+1} using $\mathcal{X}_i^k$ and relation (6.9)
  3. $k := k + 1$
  4. **Loop** to step 1 until convergence ($|\mathcal{X}_i^{k+1} - \mathcal{X}_i^n| < \varepsilon$) ;
- Final maps $\mathcal{X}_i = \mathcal{X}_i^k, \forall i = \{1, ..., N\}$

Let us now turn to some experiments.

6.3.3 Some results

In [Gong 2010] we have tested and compared our technique with state-of-the art ones on various kind of imagery. Here we first illustrate the benefit of the automatic selection of the patch size. We have processed a synthetic pair of images artificially created from a VHSR image visualizing the city of Beijing (China) by including small patterns onto real images. This pair is visible in figure 6.5(a-b) and the ground truth is depicted in 6.5(c,f). A gaussian noise of variance 25 has also been added in order to analyze the stability with respect to noise. The results of the change detection technique using fixed and adaptive patch-size are respectively represented in fig. 6.5(d) and 6.5(e). Concerning the fixed size, several possibilities ranging from low (half-size $q = 3$) to high ($q = 15$) values have been

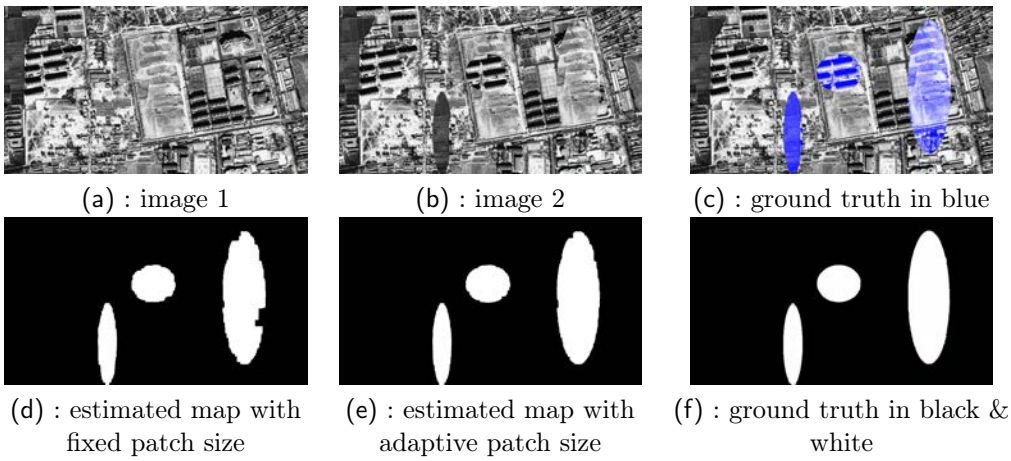

(a) : image 1 (b) : image 2 (c) : ground truth in blue

(d) : estimated map with fixed patch size (e) : estimated map with adaptive patch size (f) : ground truth in black & white

FIGURE 6.5 – **Change detection results on synthetic data** with adaptive and fixed patch size.

tested and the best result is depicted in fig. 6.5(d). From these images, one can observe that the change areas are better preserved within the adaptive selection process. This observation is verified on the quantitative measurements of table 6.2. In this latter are represented the average values of true/false positive/negative and their global accuracy (ratio TRUE(positive-negative)/FALSE(positive-negative)) for the tested images. Apart from the true positive situation (where the fixed size $q = 7$ performs better), all other criteria, including the overall accuracy for positive and negative detection, exhibit their best results with the adaptive patch size process. We then conclude that the proposed technique is efficient and prevents from the delicate task of fixing a patch size.

We also have tested our approach on various pair of images : agricultural data (FIG. 6.6(a,b)), urban data (FIG. 6.6(d,e)) and video data (FIG. 6.6(g,h)). Change detection results are respectively in FIG. 6.6(c,f,i).

Concerning **agricultural images**, these latter are often affluent in anisotropic texture due to the different type of crops, the digging, ... In addition, because of the lack of meta-information in the first image, it is impossible to ensure a proper registration of the data. On such situations, it is hence very difficult to extract spatially consistent change areas without performing a pre-segmentation step. It is firstly promising to observe that the extracted areas are quite compact despite the difficulties mentioned above. In addition, our approach exhibits changed regions in accordance with the visual inspection one can perform on this scene. For instance on the forest area (right part of the images), three different kind of changes have appeared and correctly been detected :

1. the apparition of a new agricultural parcel (white band in the bottom part) ;
2. the change of land cover of the top-left part of the forest ;
3. the reforestation in the top right part.

The same conclusions hold when observing other changes. We then conclude that our technique is able to highlight correctly the changes in these difficult situations.

On the **urban** pair, many changes from different nature have occurred (apparition of various kind of buildings, different land cover for instance). In addition, several effects due to shadows (more important in the second image) or different shooting angles are likely to disturb the estimation. One can observe that the estimated masks seem to correctly segregate the various changes that have appeared. In addition, the strong shadows of the

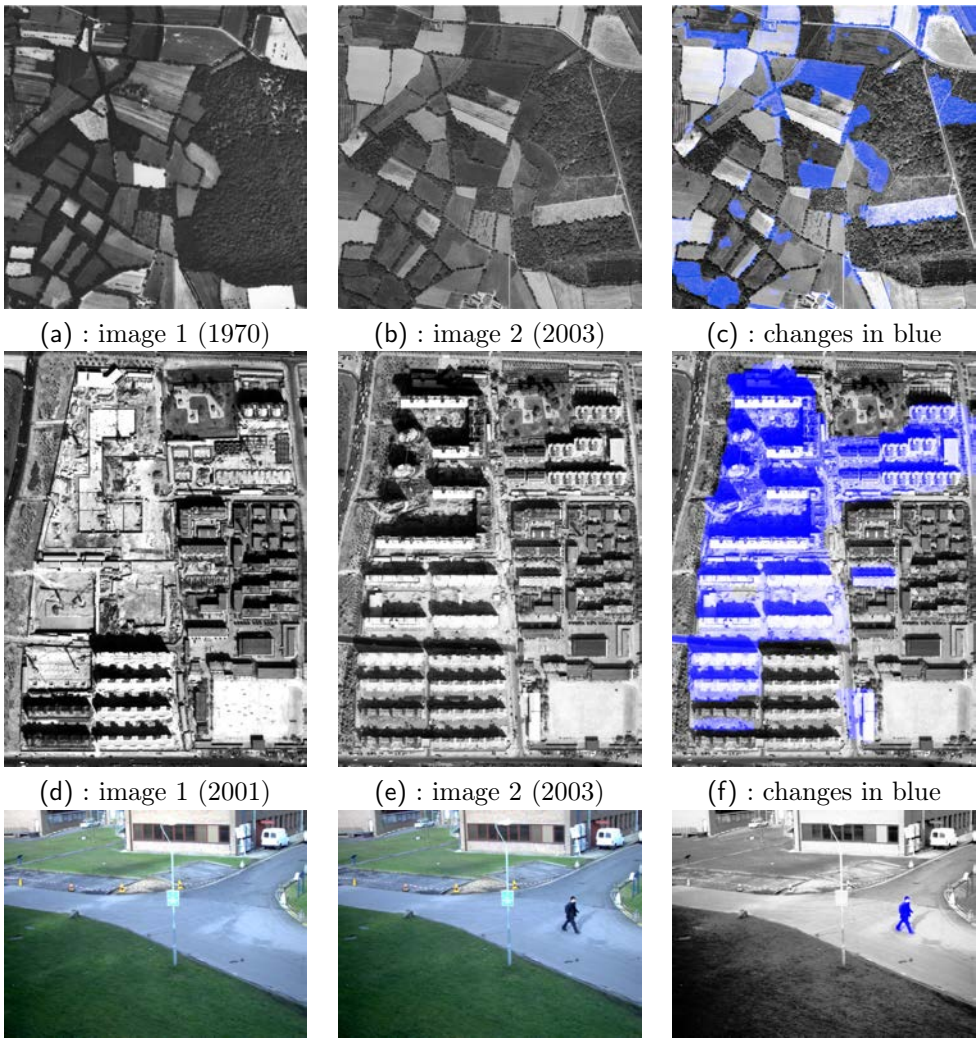

(a) : image 1 (1970) (b) : image 2 (2003) (c) : changes in blue

(d) : image 1 (2001) (e) : image 2 (2003) (f) : changes in blue

(g) : image 1 (h) : image 2 (i) : changes in blue

FIGURE 6.6 – **Change detection results on various real data** corresponding to agriculture, urban and usual video. Left column : image 1 ; Middle column : image 2 ; Right column : estimated change areas

TABLE 6.2 – **Quantitative detection indexes for fixed and variable size of the patches.** First column (resp. Fourth column) : True positive (resp. True negative) index ; Second column (resp. Fifth column) : False positive (resp. False negative) index ; Third column (resp. Sixth column) : Accuracy of positive dection : ratio True positive over False positive (resp. Accuracy of negative dection : ratio True negative over False negative)

Patch Size	True Pos.	False Pos.	Acc. Pos.	True Neg.	False Neg.	Acc. Neg.
$q = 3$	92.9%	2.2%	42.0	99.6%	1.1%	90.6
$q = 5$	93.6%	2.5%	37.4	99.6%	1.0%	99.6
$q = 7$	**93.6%**	2.8%	33.9	99.5%	1.0%	99.5
$q = 9$	93.5%	3.0%	31.2	99.5%	1.0%	99.5
$q = 11$	92.7%	3.0%	30.9	99.5%	1.1%	90.5
$q = 13$	92.3%	3.1%	29.8	99.5%	1.2%	82.9
$q = 15$	91.9%	3.1%	29.4	99.5%	1.3%	76.5
adaptive	92.2%	**1.9%**	**48.9**	**99.7%**	**0.9%**	**110.7**

2003 image have not influenced the estimation. From these observations one can conclude that the proposed technique performs efficiently on these tricky images.

It is remarkable to outline the reliable accuracy of the experiment in **usual video** sequences, despite the fact that the couple of images exhibits different lighting conditions (shadows not properly aligned, different global luminance, ...). For instance, let us point out that the pedestrian has correctly been extracted while its shadows is not assigned to a change area, which is to our opinion a very interesting behavior.

These experiments on various data demonstrate the ability of such approach to correctly estimate changes in various situations. Others experiments can be seen in our web-page [1].

6.4 Multilabel change detection using model selection

6.4.1 Overview

This work, in progress, extends the methodology of the previous section to perform a multi-label change detection. As :

- the changes come from different sources (change of scale, orientation, land cover, ...) and ;
- several possibilities are available to sense these various changes (in particular using criteria of the section 6.2),

the objective is now, for each location $\boldsymbol{x}$ of an image, to select the best change map $\mathcal{X}_i$ depending on the data. The possible labels are then $\boldsymbol{\ell}(\boldsymbol{x}) = 0$ if no change appear or $\boldsymbol{\ell}(\boldsymbol{x}) = i$ if a change associated to the map $\mathcal{X}_i$ (subtle, abrupt, scale, ...) was involved. This problem of multi-label change detection reduces then to a problem of model selection : how to find the best model $\mathcal{M}_i$ (corresponding to a threshold on map $\mathcal{X}_i$) depending on the data I. As a consequence, it is now impossible to ignore the denominator of relation (6.1) as we did in the previous section. We then need to rewrite the maximization process.

1. http://liama.ia.ac.cn/tipe/site/demos.html

6.4.2 Model selection

Each model $\mathcal{M}_i$ is related to a particular change and corresponds in practice to a thresholding on the change map $\mathcal{X}_i$. The associated probability reads :

$$\mathcal{P}(I|\boldsymbol{\ell},\mathcal{M}_i) = \frac{1}{C_{\mathcal{M}_i}} \exp - \sum_{\boldsymbol{x}} \phi_1(\mathcal{X}_i(\boldsymbol{x}),\tau_i,\boldsymbol{\ell}(\boldsymbol{x})) \tag{6.10}$$

where $C_{\mathcal{M}_i}$ is a normalization constant. Noting that the prior term $\mathcal{P}(\boldsymbol{\ell}|\mathcal{M}_i)$ reads :

$$\mathcal{P}(\boldsymbol{\ell}|\mathcal{M}_i) = \frac{1}{C_p} \exp -k_\beta \sum_{(\boldsymbol{x},\boldsymbol{y})\in\mathcal{V}} \phi_2(I,\boldsymbol{\ell}(\boldsymbol{x}),\boldsymbol{\ell}(\boldsymbol{y})) \tag{6.11}$$

where C_p is the associated normalization constant, from relation (6.1) we now need to find $i,\boldsymbol{\ell}^*$ such that $\mathcal{M}_i$ and $\boldsymbol{\ell}^*$ maximize the relation :

$$\begin{aligned}\max_{i,\boldsymbol{\ell}^*} \mathcal{P}(I|\boldsymbol{\ell},\mathcal{M}_i) = \frac{1}{C_{\mathcal{M}_i} C_{\mathrm{p}} \mathcal{P}(I|,\mathcal{M}_i)} \exp - \Bigg(& \sum_{\boldsymbol{x}} \phi_1(\mathcal{X}_i(\boldsymbol{x}),\tau_i,\boldsymbol{\ell}(\boldsymbol{x})) \\ & + k_\beta \sum_{(\boldsymbol{x},\boldsymbol{y})\in\mathcal{V}} \phi_2(I,\boldsymbol{\ell}(\boldsymbol{x}),\boldsymbol{\ell}(\boldsymbol{y})) \Bigg),\end{aligned} \tag{6.12}$$

In is shown in [MacKay 1992] that solving this 2-level of inference problem yields to :

1. a model fitting step. This is the first level of inference. All labels $\boldsymbol{\ell}_i(\boldsymbol{x})$ are computed for all models $\mathcal{M}_i$ independently ;
2. a model comparison step. This is the second level of inference. We wish to infer which model is most plausible given the data. The posterior probability of each model is such that :

$$\mathcal{P}(\mathcal{M}_i|I) \propto \mathcal{P}(I|\mathcal{M}_i)\mathcal{P}(\mathcal{M}_i). \tag{6.13}$$

Assuming we have no reason to assign strongly differing priors $\mathcal{P}(\mathcal{M}_i)$ to the alternative models $\mathcal{M}_i$, they are ranked by evaluating the evidence $\mathcal{P}(I|\mathcal{M}_i)$.

The first step has no difficulties and is performed following the technique of the previous section where the data term reduces to a single model $\mathcal{M}_i$. The second step requires to evaluate the evidence $\mathcal{P}(I|\mathcal{M}_i)$ which is obtained by marginalization of $\mathcal{P}(I|\mathcal{M}_i)$:

$$\mathcal{P}(I|\mathcal{M}_i) = \int \mathcal{P}(I|\boldsymbol{\ell},\mathcal{M}_i)\mathcal{P}(\boldsymbol{\ell}|\mathcal{M}_i) d\boldsymbol{\ell}. \tag{6.14}$$

Obviously its direct numerical evaluation is impossible since it would require too many computations as the set of possible configurations of $\boldsymbol{\ell}$ is huge. Moreover, the normalization constants involved in relations (6.11-6.12) are unknown. In order to alleviate this problem, let us note that the normalization constant C_p associated to the prior term in (6.11) does not depend on the model $\mathcal{M}_i$ since it is a simple regularizer. Therefore we have :

$$\mathcal{P}(I|\mathcal{M}_i) \propto \int \mathcal{P}(I|\boldsymbol{\ell},\mathcal{M}_i) \exp - \left(k_\beta \sum_{(\boldsymbol{x},\boldsymbol{y})\in\mathcal{V}} \phi_2(I,\boldsymbol{\ell}(\boldsymbol{x}),\boldsymbol{\ell}(\boldsymbol{y})) \right). \tag{6.15}$$

The evaluation of this term can be performed using the Metropolis-Hasting algorithm [Hastings 1970, Metropolis 1953]. This generates in an efficient way and without the knowledge of $\mathcal{C}_{\mathcal{M}_i}$ a set of M samples $\boldsymbol{\ell}_\imath$, $\imath = \{1,...,M\}$ following the distribution $\mathcal{P}(I|\boldsymbol{\ell},\mathcal{M}_i)$.

From these M samples we get an approximation of the previous relation through :

$$\mathcal{P}(I|\mathcal{M}_i) \approx \frac{1}{M}\sum_{\imath=1}^{M} \exp - \left(k_\beta \sum_{(\boldsymbol{x},\boldsymbol{y})\in\mathcal{V}} \phi_2(I, \boldsymbol{\ell}_\imath(\boldsymbol{x}), \boldsymbol{\ell}_\imath(\boldsymbol{y})) \right). \tag{6.16}$$

The evidence of each model can then be evaluated and we keep the one with the highest value. The final technique for multi-label change detection reads then :

Multi-label change detection
- N maps $\mathcal{X}_i$, $i = \{1, ..., N\}$ associated to the confidence on the label i are available.
- For all locations $\boldsymbol{x} \in \boldsymbol{X}_t$ do :
  - $1^{\mathbf{st}}$ **level of inference**. For $i = \{1, ..., N\}$
    - Computed the value $\boldsymbol{\ell}_i(\boldsymbol{x})$ on a patch around $\boldsymbol{x}$ by minimizing the cost-function in (6.2) where only the map $\mathcal{X}_i$ is involved.
  - if $\forall i, \boldsymbol{\ell}_i(\boldsymbol{x}) = 0$, we have no change and $\boldsymbol{\ell}(\boldsymbol{x}) = 0$, else
    - $2^{\mathbf{nd}}$ **level of inference**. For $i = \{1, ..., N\}$
      - Creation of M samples $\boldsymbol{\ell}_\imath$, $\imath = \{1, ..., M\}$ of $\mathcal{P}(I|\boldsymbol{\ell}, \mathcal{M}_i)$ using a Metropolis algorithm ;
      - Evaluate the evidence $\mathcal{P}(I|\mathcal{M}_i)$ using relation (6.16) ;
    - Final result :
      - Select the model i with the highest value of the evidence $\mathcal{P}(I|\mathcal{M}_i)$;
      - If $\boldsymbol{\ell}_i(\boldsymbol{x}) = 0$, no change appear and $\boldsymbol{\ell}(\boldsymbol{x}) = 0$ otherwise $\boldsymbol{\ell}(\boldsymbol{x}) = i$

It should be pointed out that most of the existing techniques for multi-label change detection use some training samples and machine learning. This requires a fastidious task of manually label the training set and yield some data-dependant techniques. The proposed approach does not need any learning step which is to our opinion a key point. The process is at the moment under development and we present preliminary results in the next section.

6.4.3 Preliminary results

We have tested the process on the synthetic pair of images depicted in figures Fig. 6.7(a,b). The image Fig. 6.7(b) has been generated from the image in Fig. 6.7(a) by blurring two parts : the top-left one with an abrupt change (the global luminance is modified) and the bottom-right one with a subtle change (the global luminance is kept but the internal texture is modified). The multi-label change detection strategy was used with two change maps : an abrupt change one based on the difference in terms of luminance and a subtle change one based on the Kullback-Leibler difference of the distribution of the gradients of the luminance inside a given patch. Multi-label results are shown in figure Fig. 6.7(c). It is very encouraging to observe that the two areas have been correctly labeled. This synthetic example is a first validation of the methodology.

Using the same technique on real data requires to use more advanced change maps. Indeed, the simple measurements based on the luminance and the gradients defined to segregate abrupt and subtle changes are obviously too simple regarding the complexity of the real structures encountered in remote sensing data. On such images, it is preferable to use more advanced change maps as the components of the change vector $\mathcal{D}$ proposed in section 6.2. This is under development.

Nevertheless to our opinion, the promising results on the synthetic pair of image already validates this multi-label strategy which is of great importance since no training samples are required.

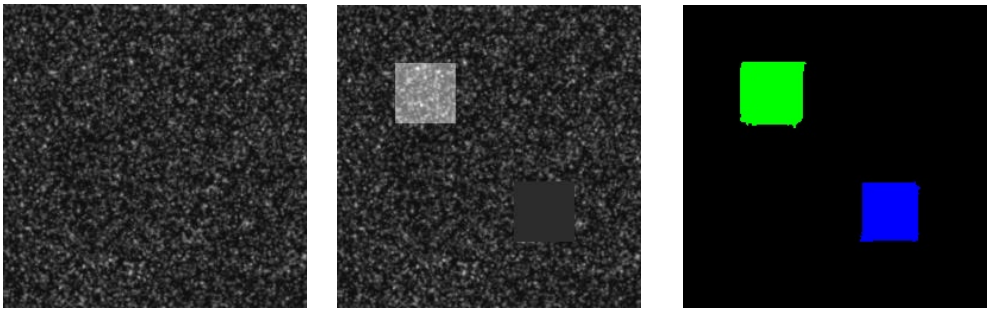

(a) : image 1 (b) : image 2 (c) : subtle changes in blue ; abrupt changes in green

FIGURE 6.7 – **Multi-label change detection results on a synthetic pair of images.** (a,b) : two input images with abrupt and subtle changes : (c) estimated labels of change areas

6.5 Summary

In this chapter we have proposed some solutions for the change detection problem. This issue is very crucial in computer vision and in particular in remote sensing. Depending on the input data and in particular on the availability of some pre-segmented maps or not, we have proposed several tools for sensing the changes.

The first one is rather related to the measurements and aims at qualifying the nature of the changes between two objects. It relies on some combinations at different scales/orientations of similarity criteria between the distributions of coefficients issued from a wavelet decomposition.

The second one does not rely on pre-segmented objects and labels the changes by minimizing a cost function on patches where we have proposed an original way to fix its size.

These two techniques have been successfully validated on synthetic and real data.

We also have proposed the theoretical aspects of a multi-label change detection technique that formalize the problem through a model selection one. We then need to calculate the change for each model (related to a label) and then to evaluate the evidence, this latter being approximated using Metropolis sampling techniques. This process is under development and preliminary results on synthetic pair of images are encouraging.

Conclusion of the second part

In this second part, we were focused on the analysis of time series of Very High Spatial Resolution (VHSR) remote sensing data.

To that end, we first have worked on the definition of descriptors. VHSR data indeed embed very complex objets for which there is no general tools to describe them. We have proposed an efficient and simple way to represent the different structures based on the distributions of the coefficients issued from a wavelet decomposition of the images. We in addition have introduced a technique that relies on evidence theory able to compare two entities characterized with such descriptors. They have been successfully used for various remote sensing problems including segmentation, classification, front detection, texture orientation estimation and change detection.

Concerning this last application, we in addition have presented some techniques for binary and multi label change detection based on patches, stochastic representation of the data and model selection.

Troisième partie

Conclusion & Perspectives

General Conclusion & Prespectives

Conclusion

In the presented works, we have proposed solutions for dealing with time series of Low Spatial Resolution and Very High Spatial Resolution remote sensing images. The manipulation of such data require indeed specific processing since the involved structures (clouds, urban or agricultural parcels, ...) exhibit complex properties in terms of luminance (texture, deformations, transparency, ...) that can hardly be managed using conventional tools.

The challenges related to LSR data that we have faced were concerned with motion estimation, curve tracking and oceanic data reconstruction. We have mainly been based on the variational data assimilation framework for which we have proposed adapted observation operators, dynamical models and error covariance matrices that include recipes of image processing.

As for VHSR images, we have proposed some descriptors of the textured entities that appear (crops, urban, clouds, ...). They rely on wavelet coefficients. From two objects, we have been based on the evidence theory to derive a unique similarity criterion between them. These descriptors have been used for segmentation, classification and estimation of the orientation of agricultural parcels. In addition, we have addressed the problem of binary and multi-label change detection between two images. To that end we have computed statistics on patches where an original technique for defining their size based on a stochastic representation of the data has been proposed. As regards the multi-label issue, this has been formalized as a model selection problem.

Although remote sensing was the privilege application, most of our tools have been successfully used in other contexts as for instance usual video sequences (motion estimation, change detection, texture description) or crowd analysis.

Let us now turn to the perspectives for the next years.

Perspectives

As for the future works, one can note that :

1. it has been observed in some applications that the dynamically consistent techniques proposed for LSR images exhibit errors mainly concentrated at the fine scale structures. These latter are however crucial for the flow analysis. In addition, due to inverse-cascade effects, a poor-estimation of fine scales (unresolved subgrid-scales) disturbs the accuracy of the estimation on the larger structures of the flow. It is now of prime importance to directly deal with models on the different scales of the flow ;
2. A very large number of VHSR satellites are launched. For instance, Quickbird, Geoeye or Ikonos are at the moment available. In addition, very important missions such as the Venus (CNES [2]-ISA [3]) and the Sentinel-2 (ESA [4]) ones are expected in 2012 and

2. Acronym for : National Center of Spatial Studies
3. Acronym for : International Spatial Agency
4. Acronym for : European Spatial Agency

2013. Therefore, this provides a more or less temporal consistency in VHSR observations of the land use of some relevant sites (intense agricultural areas in particular). The analysis of such time series is of prime importance for all topics related to environmental applications. However at the moment, no computer vision system is able to deal with such specific time series, where the observations are issued from different sensors.

As a consequence my future researches will continue to design some image processing methods for time series of LSR and VHSR data in order to overcome the mentioned difficulties. The following two paragraphs propose some directions that will be explored.

LSR data

Concerning the LSR data, we plan now to rely on advanced spatial models for subgrid-scale modeling. The problem of turbulence, in particular the small scale turbulence (i.e., under pixel), is generally ignored in the flow equation of existing methods. However, in the reality most of the fluid flows are highly turbulent : atmospheric motions, ocean currents, vascular flows, ... The level of turbulence of the flow is controlled by the Reynolds number $Re = UL/\nu$ where U, L are the velocity and length scales of the flow and ν the kinetic viscosity of the fluid. For high Re, the flow is turbulent. The ratio between scale of large eddy and smallest wave length of movement that can appear in the fluid (Kolmogorov scale) is proportional to $Re^{3/4}$. This implies that to get all scales which appear in the turbulent flow, time and space resolution have to be equivalent to $Re^{3/4}$ (for example, for atmospheric flows $Re \approx 10^{10}$). Generally, time and space image resolution are much sparser than the smallest scales. Depending on the rate of turbulence, missing information in the image sequence may not be neglected. The influence of these small scales cannot be computed but should be modeled. To this end, subgrid modeling developed in Large Eddy Simulation of turbulent flows should be benefit. In particular, since last five years, L. Shao and his collaborators develop in a physical and rational way a set of subgrid models, the so-called ReDLES. The main point in this approach is to use statistical 2-point approach such as the structure function and the multi-scale energy budget which are well adapted for taking into account the interaction between different turbulent scales. This approach has been proved to be more suitable for the physical modeling of the influence of the subgrid scale [Cui 2007, Lévêque 2007]. We plan then to explore these kind of models to improve the actual data assimilation techniques.

VHSR data

As for the VHSR images, biophysical variables derived from satellite observations like the LAI (Leaf Area Index), fCOVER (fraction of vegetation cover) or fAPAR (fraction of Absorbed Photosynthetically Active Radiation) are now widely used to monitor the dynamics in canopy vegetation over large areas at global and regional scales. Biophysical products derived from current coarse and medium sensors allow estimating changes in landscapes made of large patches. However in fragmented landscapes characterizing intensive agricultural areas, the medium spatial resolution is not suited to identify changes in vegetation cover due to mixing effects. Higher spatial resolution is thus required to analyze the vegetation. However, the models that extract bio-physical parameters have been built for data with lower spatial resolutions. Thus, they have to be adapted, or other models that fit with high spatial resolution data have to be conceived.

The COSTEL group (presented in the introduction), with the OSUR [5] (Observatory for

5. http://osur.univ-rennes1.fr/

Universe Sciences at Rennes, France) and their collaborators, are working on the design of original approaches to estimate biophysical variables for VHSR sensors. More precisely, we have worked together on the estimation of fAPAR, LAI and fCOVER based on a radiative transfer model (PROSPECT-SAIL) [Lecerf 2005]. This results in time series of biophysical data that however suffer from a lack of temporal consistency due to the temporal and content heterogeneity of the data used.

Future researches will then consist in retrieving time consistent series of such biophysical parameters. To that end, we plan to use tracking and filtering techniques in which we will explore some agricultural models for vegetation evolution. We will first focus on BONSAI and STICS (Simulateur mulTIdisciplinaire pour les Cultures Standard) models, developed by INRA, that simulate the usual bio-physical variables (LAI in particular) and others relevant variables like the total biomass [Brisson 2002]. We will also collaborate with the ECO-INFO team of LIAMA which is working on the definition of plant growing models [Cournède 2006, Fourcaud 2008]. We already have started to use the GreenLab model for the assimilation of LAI [Kang 2011].

Context

We have created a new LIAMA team entitled TIPE [6] for "Turbulence, Images, Physics and Environment". I am the principal investigator of this group. This is a CNRS & Tsinghua University joined project focused on the analysis of time series of remote sensing data, both on low and very high spatial resolution images.

Involved CNRS partners are Ecole Centrale Lyon (especially with LMFA : Lab of Fluid Mechanics & Acoustics [7]) and OSUR (especially with COSTEL Lab). As for Tsinghua University, the Turbulence Lab [8] of the Department of Engineering Mechanics is involved in this team.

I then plan to develop these researches in the context on the TIPE group. An additional important goal is to consolidate collaborations between french and chinese groups on these topics.

6. http://liama.ia.ac.cn/tipe/
7. http://lmfa.ec-lyon.fr/
8. http://me.tsinghua.edu.cn/english/index.php3

Bibliographie

[Aach 1993] T. Aach, A. Kaup et R. Mester. *Statistical model-based change detection in moving video.* Signal Processing, vol. 31, no. 2, pages 165–180, Mars 1993. 86

[Adrian 1991] R.J. Adrian. *Particle-Imaging Techniques for Experimental Fluid Mechanics.* Annual Review of Fluid Mechanics, vol. 23, pages 261–304, 1991. 15

[Adrian 2005] R.J. Adrian. *Twenty years of particle image velocimetry.* Experiments in Fluids, vol. 39, no. 2, pages 159–169, 2005. 15

[Allain 2009] P. Allain, N. Courty et T. Corpetti. *Crowd Flow Characterization with Optimal Control Theory.* In LNCS, editeur, Proc. of 9th Asian Conference on Computer Vision, ACCV'09, pages 279–290, Xi'an, China, 2009. 55, 56

[Alvarez 1993] L. Alvarez, F. Guichard, P.-L. Lions et J.-M. Morel. *Axioms and fundamental equations of image processing.* Archive for Rational Mechanics and Analysis, vol. 123, no. 3, pages 199–257, 1993. 81

[Alvarez 2009] L. Alvarez, C.A. Castano, M. GarcÌa, K. Krissian, L. Mazorra, A. Salgado et J. Sanchez. *A new energy-based method for 3D motion estimation of incompressible PIV flows.* Computer Vision and Image Understanding, vol. 113, no. 7, pages 802–810, 2009. 16

[Amodei 1991] L. Amodei et M.N. Benbourhim. *A vector spline approximation.* J. Approx. Theory, vol. 67, no. 1, pages 51–79, 1991. 16

[Arnaud 2006] E. Arnaud, E. Mémin, R. Sosa et G. Artana. *A fluid motion estimator for Schlieren imaging velocymetry.* In Proc. European Conf. Comp. Vision (ECCV'06), volume 3951 (LNCS, pages 198–210, Graz, Austria, 2006. 15

[Baker 2004] S. Baker et I. Matthews. *Lucas-Kanade 20 Years On : A Unifying Framework.* International Journal of Computer Vision, vol. 56, no. 3, pages 221–255, 2004. 14

[Baker 2007] S. Baker, D. Scharstein, J.P. Lewis, S. Roth, M. Black et R. Szeliski. *A Database and Evaluation Methodology for Optical Flow.* In Int. Conf. on Comp. Vis., ICCV 2007, 2007. 11, 14

[Barron 1994] J.L. Barron, D.J. Fleet, S.S. Beauchemin et T.A. Burkitt. *Performance Of Optical Flow Techniques.* International Journal of Computer Vision, vol. 12, no. 1, pages 43–77, 1994. 11, 14, 25

[Becker 2008] F. Becker, B. Wieneke, J. Yuan et C. Schnoerr. *A Variational Approach to Adaptive Correlation for Motion Estimation in Particle Image Velocimetry.* Pattern Recognition, vol. 5096, pages 335–344, 2008. 15

[Belfiore 2005] S. Belfiore, M. Grangetto, E. Magli et G. Olmo. *Concealment of whole-frame losses for wireless low bit-rate video based on multiframe optical flow estimation.* IEEE Transactions on Multimedia, vol. 7, no. 2, pages 316–329, Avril 2005. 11

[Belyaev 2001] K.P. Belyaev, C.A.S. Tanajura et J.J. O Brien. *A data assimilation method used with an ocean circulation model and its application to the tropical atlantic.* Applied Mathematical Modelling, pages 655–670, 2001. 49

[Benediktsson 1990] J.A. Benediktsson, P.H. Swain et O.K. Ersoy. *Neural Network Approaches Versus Statistical Methods In Classification Of Multisource Remote Sensing Data.* Geoscience and Remote Sensing, IEEE Transactions on, vol. 28, no. 4, pages 540 – 552, Juillet 1990. 80

[Bennett 1992] A.F. Bennett. Inverse Methods in Physical Oceanography. Cambridge University Press, 1992. 30, 31

[Bergen 1992] J.R. Bergen, P. Anandan, K.J. Hanna et R. Hingorani. *Hierarchical Model-Based Motion Estimation*. In G Sandini, editeur, ECCV, volume 2 of *Lecture Notes in Computer Science*, pages 237–252. Springer, 1992. 15

[Black 1991] M.J. Black et P. Anandan. *Robust dynamic motion estimation over time*. In IEEE Conf. on Comp. Vis. and Patt. Rec., pages 292–302, Maui, HI, USA, 1991. 29

[Black 1992] M.J. Black. *Robust incremental optical flow*. PhD thesis, Yale University, Department of Computer Science, 1992. 14

[Bosc 2003] M. Bosc, F. Heitz, J.-P. Armspach, I. Namer, D. Gounot et L. Rumbach. *Automatic change detection in multimodal serial MRI : application to multiple sclerosis lesion evolution*. NeuroImage, vol. 20, no. 2, pages 643–656, Octobre 2003. 85

[Boulanger 2007] J. Boulanger, C. Kervrann et P. Bouthemy. *Space-time adaptation for patch-based image sequence restoration*. Pattern Analysis and, vol. 29, no. 6, pages 1096–102, Juin 2007. 92

[Bowman 1997] A.W. Bowman et A. Azzalini. Applied Smoothing Techniques for Data Analysis. Oxford Univ. Press, 1997. 69

[Breiman 1984] L. Breiman, J. Friedman, R. Olshen et C. Stone. Classification and Regression Trees. Wadsworth and Brooks, Monterey, CA, 1984. 88

[Brisson 2002] N. Brisson, F. Ruget, P. Gate, J. Lorgeou, B. Nicoullaud, X. Tayot, D. Plenet, .M-H. Jeuffroy, A. Bouthier, D. Ripoche, B. Mary et E. Justes. *STICS : a generic model for simulating crops and their water and nitrogen balances. II. Model validation for wheat and maize*. Agronomie, vol. 22, no. 1, pages 69–92, 2002. 105

[Brox 2004] T. Brox, A. Bruhn, N. Papenberg et J. Weickert. *High accuracy optical flow estimation based on a theory for warping*. In European Conference on Comput. Vis. (ECCV'04). Springer–Verlag, 2004. 14, 29

[Bruhn 2005] A. Bruhn, J. Weickert et C. Schnörr. *Lucas/Kanade Meets Horn/Schunck : Combining Local and Global Optic Flow Methods*. Int. J. Comput. Vis., vol. 61, no. 3, pages 211–231, 2005. 16

[Bruzzone 2002] L. Bruzzone et S.B. Serpico. *An iterative technique for the detection of land-cover transitions in multitemporal remote-sensing images*. IEEE Transactions on Geosciences and Remote Sensing, vol. 35, no. 4, pages 858–867, Juillet 2002. 86

[Bruzzone 2009] L. Bruzzone et C. Persello. *A Novel Approach to the Selection of Spatially Invariant Features for the Classification of Hyperspectral Images With Improved Generalization Capability*. Geoscience and Remote Sensing, IEEE Transactions on, vol. 47, no. 9, pages 3180 –3191, 2009. 80

[Bruzzone 2010] L. Bruzzone et M. Marconcini. *Domain Adaptation Problems : A DASVM Classification Technique and a Circular Validation Strategy*. Pattern Analysis and Machine Intelligence, IEEE Transactions on, vol. 32, no. 5, pages 770 –787, Mai 2010. 80

[Carleer 2005] A.P. Carleer, O. Debeir et E. Wolff. *Assessment of very high spatial resolution satellite image segmentations*. Photogrammetric Engineering and Remote Sensing, vol. 71, pages 1285–1294, 2005. 75

[Caselles 1997] V. Caselles, R. Kimmel et G. Sapiro. *Geodesic Active Contours*. Int. J. Comput. Vision, vol. 22, no. 1, 1997. 46

[Cassisa 2010] C. Cassisa, S. Simoens, V. Prinet et L. Shao. *Sub-grid physical optical flow for remote sensing of sandstorm.* In Proceedings of the International Geoscience and Remote Sensing Symposium (IGARSS'10), Hawai, US, 2010. 15, 25, 26

[Chan 2001] T. Chan et L. Vese. *Active contours whitout edges.* IEEE Trans. Image Processing, vol. 10, no. 2, pages 266–277, 2001. 46

[Chanussot 2010] J. Chanussot, M. M. Crawford et B.-C. Kuo. *Foreword to the Special Issue on Hyperspectral Image and Signal Processing.* Geoscience and Remote Sensing, IEEE Transactions on, vol. 48, no. 11, pages 3871 –3876, 2010. 80

[Chorin 1973] A.J. Chorin. *Numerical Study of Slightly Viscous Flow.* Journal of Fluid Mechanics, vol. 57, no. 4, pages 785–796, 1973. 16

[Cohen 1997] L.D. Cohen et R. Kimmel. *Global Minimum for Active Contour Models : A Minimal Path Approach.* International Journal of Computer Vision, vol. 24, no. 1, pages 57–78, 1997. 82

[Cohen 1998] I. Cohen et I. Herlin. *Tracking meteorological structures through curve(s) matching using geodesic paths.* In Proc of 6th IEEE Int. Conf on Computer Vision, pages 396–401, Bombay, 1998. 46

[Cohen 1999] I. Cohen et G. Medioni. *Detecting and Tracking Moving Objects in Video Surveillance.* In Proceedings of IEEE Computer Vision and Pattern Recognition, 1999. 11

[Collins 2000] R. Collins, A. Lipton et T. Kanade. *Introduction to the special section on video surveillance.* IEEE Trans. on Patt. Anal. and Mach. Intell., vol. 22, no. 8, pages 745–746, 2000. 85

[Corpetti 2002] T. Corpetti, E. Mémin et P. Pérez. *Dense Estimation of Fluid Flows.* IEEE Transactions on Pattern Analysis and Machine Intelligence, vol. 24, no. 3, pages 365–380, 2002. 11, 15, 16, 17, 19, 25, 26, 27, 35, 54

[Corpetti 2003] T. Corpetti, E. Mémin et P. Pérez. *Extraction of Singular Points from Dense Motion Fields : an Analytic Approach.* Journal of Mathematical Imaging and Vision, vol. 19, no. 3, pages 175–198, 2003. 32

[Corpetti 2006] T. Corpetti, D. Heitz, G. Arroyo, E. Mémin et A. Santa-Cruz. *Fluid experimental flow estimation based on an optical-flow scheme.* Experiments in fluids, vol. 40, no. 1, pages 80–97, 2006. 15, 16, 19

[Corpetti 2008a] T. Corpetti, P. Héas, E. Mémin et N. Papadakis. *Pressure image assimilation for atmospheric motion estimation.* Research Report 6507, INRIA, 2008. 37, 38, 39, 40

[Corpetti 2008b] T. Corpetti, P. Héas, E. Mémin et N. Papadakis. *Variational pressure image assimilation for atmospheric motion estimation.* In IEEE Int. Geoscience and Remote Sensing Symp., IGARSS '08, volume 2, pages 505–508, Boston, USA, 2008. 37

[Corpetti 2009] T. Corpetti, P. Héas, E. Mémin et N. Papadakis. *Pressure image assimilation for atmospheric motion estimation.* Tellus Series A : Dynamic Meteorology and Oceanography, vol. 61, no. 1, pages 160–178, 2009. 35, 37, 38, 39

[Corpetti 2010] T. Corpetti et O. Planchon. *Front detection on satellite images based on wavelet and evidence theory : application to the sea breeze fronts.* Remote Sensing of Environment, to appear, 2010. 81, 82

[Corpetti 2011] T. Corpetti et E. Mémin. *Stochastic uncertainty models for the luminance consistency assumption.* IEEE Trans. on Image Processing, 2011. 23, 24, 25, 26, 28, 51

[Cournède 2006] P.-H. Cournède, M.-Z. Kang, A. Mathieu, J.-F. Barczi, H.-P. Yan, B.-G. Hu et P. De Reffye. *Structural Factorization of Plants to Compute Their Functional and Architectural Growth.* Simulation, vol. 82, no. 7, pages 427–438, 2006. 105

[Courty 2007a] N. Courty et T. Corpetti. *Crowd Motion Capture.* Journal of Visualization and Computer Animation, vol. 18, no. 4, pages 361–370, 2007. 54

[Courty 2007b] N. Courty et T. Corpetti. *Data-Driven Animation of Crowds.* In LNCS, editeur, Proceedings of Mirage 2007 – Computer Vision / Computer Graphics Collaboration Techniques and Applications, volume 4418, pages 377–388, Paris, France, 2007. 54

[Cui 2007] G.X. Cui, C.X. Xu, L. Fang, Z.S. Zhang et L. Shao. *A New subgrid eddy-viscosity model for large-eddy simulation of anisotropic turbulence.* Journal of Fluid Mechanics, vol. 582, pages 377–397, 2007. 104

[Cuzol 2005] A. Cuzol et E. Memin. *A Stochastic Filter for Fluid Motion Tracking.* Tenth IEEE International Conference on Computer Vision ICCV05 Volume 1, pages 396–402, 2005. 16

[Cuzol 2007] A. Cuzol, P. Hellier et E. Mémin. *A low dimensional fluid motion estimator.* International Journal of Computer Vision, vol. 75, no. 3, pages 329–349, 2007. 11

[Cuzol 2008] A. Cuzol et E. Mémin. *A stochastic filter technique for fluid flows velocity fields tracking.* IEEE Trans. Pattern Anal. Machine Intell., 2008. 16

[Deer 2002] P. Deer et P. Eklund. *VALUES FOR THE FUZZY -MEANS CLASSIFIER IN CHANGE DETECTION FOR REMOTE SENSING.* In 9th Int. Conf. on Information Processing and Management of Uncertainty (IPMU 2002), pages 187–194, 2002. 86

[Delanay 1998] A. Delanay et Y. Bresler. *Globally convergent edge-preserving regularized reconstruction : an application to limited-angle tomography.* IEEE Trans. Image Processing, vol. 7, no. 2, pages 204–221, 1998. 18, 26, 35, 42

[Denoeux 2008] T. Denoeux. *Conjunctive and disjunctive combination of belief functions induced by nondistinct bodies of evidence.* Artificial Intelligence, vol. 172, no. 2-3, pages 234–264, 2008. 72

[Dey 2010] V. Dey, Y. Zhang et M. Zhong. *A review on image segmentation techniques with remote sensing perspectives.* In ISPRS TC VII Symposium, volume XXXVIII, pages 31–42, 2010. 75

[Do 2002] M.N Do et M. Vetterli. *Wavelet-based texture retrieval using generalized Gaussian density and Kullback-Leibler distance.* IEEE Transactions on Image Processing, vol. 11, no. 2, pages 146–158, 2002. 71

[Fitzpatrick 1988] J.M. Fitzpatrick. *The Existence of Geometrical Density-Image Transformations Corresponding to Object Motion.* Comput. Vision, Graphics, Image Proc., vol. 44, no. 2, pages 155–174, 1988. 14, 15, 17

[Foroosh 2002] H. Foroosh, J. Zerubia et M. Berthod. *Extension of phase correlation to subpixel registration.* IEEE Trans. Image Processing, vol. 11, no. 3, pages 188–200, 2002. 13

[Fourcaud 2008] T. Fourcaud, X. Zhang, A. Stokes, H. Lambers et C. Korner. *Plant Growth Modelling and Applications : The Increasing Importance of Plant Architecture in Growth Models.* Annals of Botany, vol. 101, no. 8, pages 1053–1063, 2008. 105

[Freeman 1991] W.T. Freeman et E.H. Adelson. *The design and use of steerable filters.* IEEE Trans. on Patt. Anal. and Mach. Intell., vol. 13, no. 9, pages 891–906, 1991. 77

[Friedl 1997] M.A. Friedl et C.E. Brodley. *Decision tree classification of land cover from remotely sensed data.* Rem. Sens. of Env., vol. 61, pages 399–409, 1997. 88

[Frisch 1995] U. Frisch. Turbulence : the legacy of A.N. Kolmogorov. Cambridge university press, 1995. 37

[Fujita 1968] T. Fujita, D.L. Bradbury, Ð¡. Murino et L. Mull. *A Study of Mesoscale Cloud Motions Computed from ATS-1 and Terrestrial Photographs from Satellite.* Mesometeorological Research Project Research Paper No 71, vol. Dept. of G, page 25, 1968. 15

[Galvin 1998] B. Galvin, B. McCane, K. Novins, D. Mason et S. Mills. *Recovering motion fields : an analysis of eight optical flow algorithms.* In Proc. British Mach. Vis. Conf., Southampton, 1998. 11, 14

[Geman 1992] D. Geman et G. Reynolds. *Constrained Restoration and The Recovery Of Discontinuities.* IEEE Trans. Pattern Anal. Machine Intell., vol. 14, no. 3, pages 367–383, 1992. 18, 26, 35, 42

[Germain 2003] C. Germain, J.P. Da Costa, O. Lavialle et P. Baylou. *Multiscale estimation of vector field anisotropy. {A}pplication to texture characterization.* Signal Processing, vol. 83, pages 1487–1503, 2003. 77

[Giles 2000] M. Giles. *On the use of Runge-Kutta time-marching and multigrid for the solution of steady adjoint equations.* Rapport technique 00/10, Oxford University Computing Laboratory, 2000. 34

[Girod 2005] B. Girod, A.M. Aaron, S. Rane et D. Rebollo-Monedero. *Distributed Video Coding.* Proceedings of the IEEE, vol. 93, no. 1, pages 71–83, 2005. 14

[Gong 2010] X. Gong et T. Corpetti. *Change detection using patches of various size.* IEEE Transactions on Image Processing, submitted, 2010. 89, 91, 92

[Hastings 1970] W.K. Hastings. *Monte Carlo sampling methods using Markov chains and their applications.* Biometrika, vol. 57, no. 1, pages 97–109, 1970. 96

[Haussecker 2001] H.W. Haussecker et D.J. Fleet. *Computing optical flow with physical models of brightness variation.* IEEE Transactions on Pattern Analysis and Machine Intelligence, vol. 23, no. 6, pages 661–673, 2001. 15, 17

[Héas 2007] P. Héas, E. Mémin, N. Papadakis et A. Szantai. *Layered estimation of atmospheric mesoscale dynamics from satellite imagery.* IEEE trans. on Geoscience and Remote sensing, vol. 45, no. 12, pages 4087–4104, 2007. 15, 16, 39, 40, 41

[Héas 2008] P. Héas et E. Mémin. *3D motion estimation of atmospheric layers from image sequences.* IEEE Trans. Geoscience and Remote Sensing, 2008. 16

[Héas 2009] P. Héas, E. Mémin, D. Heitz et P.D. Mininni. *Bayesian selection of scaling laws for motion modeling in images.* In International Conference on Computer Vision (ICCV'09), 2009. 16

[Heermann 1992] P.D. Heermann et N. Khazenie. *Classification of multispectral remote sensing data using a back-propagation neural network.* Geoscience and Remote Sensing, IEEE Transactions on, vol. 30, no. 1, pages 81 –88, Janvier 1992. 80

[Heitz 2008] D. Heitz, P. Héas, E. Mémin et J. Carlier. *Dynamic consistent correlation-variational approach for robust optical flow estimation.* Exp. Fluids, vol. 45, no. 4, pages 595–608, 2008. 16

[Heitz 2009] D. Heitz, E. Mémin et C. Schnoerr. *Variational fluid flow measurements from image sequences : synopsis and perspectives.* Experiments in Fluids, vol. 48, no. 3, pages 369–393, Novembre 2009. 11, 16

[Helbing 2007] D. Helbing, A. Johansson et H. Al-Abideen. *Dynamics of crowd disasters : An empirical study.* Physical Review E (Statistical, Nonlinear, and Soft Matter Physics), vol. 75, no. 4, page 46109, 2007. 54

[Holland 1977] P. Holland et R. Welsch. *Robust Regression Using Iteratively Reweighted Least-Squares.* Commun. Statis.-Theor. Meth., vol. A6, no. 9, pages 813–827, 1977. 42

[Horn 1981] B.K.P. Horn et B.G. Schunck. *Determining optical flow.* Artificial Intelligence, vol. 17, no. 1-3, pages 185–203, 1981. 11, 14, 19, 25, 26, 27, 54

[Hsu 1984] Y. Z. Hsu, H.-H. Nagel et G. Rekers. *New likelihood test methods for change detection in image sequences.* Computer vision, graphics, and image processing, vol. 26, pages 73—-106, 1984. 86

[Huber 1981] P. Huber. Robust Statistics. John Wiley & Sons, 1981. 18, 26, 35, 42

[Hughes 2002] R.L. Hughes. *A continuum theory for the flow of pedestrians.* Transportation Research Part B : Methodological, vol. 36, no. 6, pages 507–535, 2002. 54

[Hughes 2003] R.L. Hughes. *The Flow of Human Crowds.* Annual Review of Fluid Mechanics, vol. 35, no. 1, pages 169–182, 2003. 54

[Isambert 2008] T. Isambert, J.-P. Berroir et I. Herlin. *A Multi-scale Vector Spline Method for Estimating the Fluids Motion on Satellite Images.* In David Forsyth, Philip Torr et Andrew Zisserman, editeurs, European Conference on Computer Vision, ECCV 2008, volume 5305 of *Lecture Notes in Computer Science*, pages 665–676. Springer Berlin / Heidelberg, 2008. 16

[Jafari-Khouzani 2005] K. Jafari-Khouzani et H. Soltanian-Zadeh. *Radon Transform Orientation Estimation for Rotation Invariant Texture Analysis.* IEEE Trans. on Patt. Anal. and Mach. Intell., vol. 27, no. 6, pages 1004–1008, 2005. 77

[Jahne 1998] B. Jahne, H.W. Haussecker, H. Spies, D. Schmundt et U. Schurr. *Study of dynamical processes with tensor-based spatiotemporal image processing techniques.* In Proc. Europ. Conf. Comput. Vis., Freiburg, Germany, 1998. 13

[Josso 2005] B. Josso, D.R. Burton et M.K. Lalor. *Texture orientation and anisotropy calculation by {F}ourier transform and {P}rincipal {C}omponent {A}nalysis.* Mechanical Systems and Signal Processing, vol. 19, pages 1152–1161, 2005. 77, 78, 79

[Jung 2007] C.R. Jung. *Combining wavelets and watersheds for robust multiscale image segmentation.* Image and Vision Computing, vol. 25, page 24ï¿½33, 2007. 76

[Kang 2011] M.-Z. Kang, T. Corpetti et P. De Reffye. *Estimating biomass dynamics from remote sensing through a plant model.* In Remote Sensing of Biomass : Principles and Applications / Book 1, ISBN 978-953-307-177-0., to appear. Intech, 2011. 105

[Kass 1988] M. Kass, A. Witkin et D. Terzopoulos. *Snakes : Active Contour Models.* Int. J. Comput. Vis., vol. 1, no. 4, pages 321–331, 1988. 46, 81

[Kervrann 2009] C. Kervrann, J. Boulanger et T. Pécot. *DISCRIMINANT RANDOM FIELD AND PATCH-BASED REDUNDANCY ANALYSIS FOR IMAGE CHANGE DETECTION.* In Machine Learning for Signal Processing, 2009. MLSP 2009. IEEE International Workshop on, numéro 3, pages 1 – 6, 2009. 86

[Kim 2003] J.B. Kim et H.J. Kim. *Multiresolution-based watersheds for efficient image segmentation.* Pattern Recognition Letters, vol. 24, pages 473–488, 2003. 76

[Kimmel 2001] R. Kimmel et J. Sethian. *Optimal Algorithm for Shape from Shading and Path Planning.* J. of Math. Ima. and Vis., vol. 14, no. 3, pages 237–244, 2001. 55

[Kurganov 2000a] A. Kurganov et D. Levy. *A Third-Order Semidiscrete Central Scheme for Conservation Laws and Convection-Diffusion Equations.* SIAM J. Sci. Comput., vol. 22, no. 4, pages 1461–1488, 2000. 34

[Kurganov 2000b] A. Kurganov et E. Tadmor. *New high-resolution central schemes for nonlinear conservation laws and convetion-diffusion equations.* J. Comput. Phys., vol. 160, no. 1, pages 241–282, 2000. 34

[Lapeyre 2006] G. Lapeyre et P. Klein. *Dynamics of the Upper Oceanic Layers in Terms of Surface Quasigeostrophy Theory.* Journal of Physical Oceanography, vol. 36, no. 2, page 165, 2006. 51

[Le Dimet 1986] F.-X. Le Dimet et O. Talagrand. *Variational algorithms for analysis and assimilation of meteorological observations : theoretical aspects.* Tellus, pages 97–110, 1986. 30

[Le Pouliquen 2005] F. Le Pouliquen, J.-P. Da Costa, C. Germain et P. Baylou. *A new adaptive framework for unbiased orientation estimation in textured images.* Pattern Recognition, vol. 38, no. 11, pages 2032–2046, 2005. 77

[Lecerf 2005] R. Lecerf, T. Corpetti, L. Hubert-Moy et V. Dubreuil. *Monitoring land use and land cover changes in oceanic and fragmented landscapes with reconstructed MODIS time series.* In Third International Workshop on the Analysis of Multi-temporal Remote Sensing Images, Multitemp, pages 195–199, Biloxi, Mississippi USA, May 2005. 105

[Lee 2007] K. Lee, M. Choi, Q. Hong et J. Lee. *Group behavior from video : a data-driven approach to crowd simulation.* In ACM SIGGRAPH/Eurographics Symp. on Computer Animation, SCA'07, pages 109–118, San Diego, California, 2007. 54

[Leese 1971] J.A. Leese, C.S. Novak et B.B Clark. *An Automated Technique for Obtaining Cloud Motion from Geosynchronous Satellite Data Using Cross Correlation.* American Meteorological Society, vol. 10, no. 1, pages 118–132, 1971. 15

[Lefebvre 2009] A. Lefebvre, T. Corpetti et L. Hubert-Moy. *A measure for change detection in very high resolution remote sensing images based on texture analysis.* In IEEE International Conference on Image Processing, ICIP '09, pages 1697–1700, Cairo, Egypt, 2009. 71, 86, 89

[Lefebvre 2010a] A. Lefebvre, T. Corpetti, V. Bonnardot, H. Quénol et L. Hubert-Moy. *Vineyard identification and characterization based on texture analysis in the Helderberg basin (South-Africa).* In IEEE Int. Geoscience and Remote Sensing Symp., IGARSS '10, Honolulu, Hawaii, USA, 2010. 78

[Lefebvre 2010b] A. Lefebvre, T. Corpetti et L. Hubert-Moy. *Estimation of the orientation of textured patterns via wavelet analysis.* Pattern Recognition Letters, to appear, 2010. 78

[Lefebvre 2010c] A. Lefebvre, T. Corpetti et L. Hubert-Moy. *Segmentation of very high spatial resolution panchromatic images based on wavelets and evidence theory.* In SPIE International Conference on Image and Signal Processing for Remote Sensing, Toulouse, France, 2010. 77

[Lefebvre 2011a] A. Lefebvre. *Agriculture et périurbanisation : Détection et suivi de changements d'occupation et d'usage des sols par télédétection.* PhD thesis, University Rennes 2, 2011. 76, 77, 78, 80, 89

[Lefebvre 2011b] A. Lefebvre, T. Corpetti et L. Hubert-Moy. *Application d'une méthode orientée objet basée sur une transformée en ondelettes et la théorie de Dempster-Shafer pour la caractérisation et le suivi des changements d'occupation des sols.* Revue Internationale de Geomatique, soumis, 2011. 80

[Lempitsky 2008] V. Lempitsky, S. Roth et C. Rother. *FusionFlow : Discrete-Continuous Optimization for Optical Flow Estimation.* In Proc. IEEE Comp. Vis. Patt. Rec. (CVPR), 2008. 14

[Lévêque 2007] E. Lévêque, F. Toschi, L. Shao et J.P. Bertoglio. *Shear-improved Smagorinsky model for large-eddy simulation of wall-bounded turbulent flows.* Journal of Fluid Mechanics, vol. 570, pages 491–502, 2007. 104

[Levy 1997] D. Levy et E. Tadmor. *Non-oscillatory Central Schemes for the Incompressible 2-D Euler Equations.* Math. Res. Let, vol. 4, pages 321–340, 1997. 34

[Lions 1971] J.-L. Lions. Optimal control of systems governed by PDEs. Springer-Verlag, 1971. 30

[Liu 2008] T. Liu et L. Shen. *Fluid flow and optical flow.* Journal of Fluid Mechanics, vol. 614, page 253, 2008. 15

[Lu 2004] D. Lu, P. Mausel, E. Brondízio et E. Moran. *Change detection techniques.* International Journal of Remote Sensing, vol. 25, no. 12, pages 2365–2401, 2004. 85, 86

[Lucas 1981] B.D. Lucas et T. Kanade. *An iterative image registration technique with an application to stereo vision.* International joint conference on artificial, vol. 130, pages 121–130, 1981. 11, 13, 25, 26, 27, 54

[MacKay 1992] D.J.C. MacKay. *Bayesian Interpolation.* Neural Computation, vol. 4, no. 3, pages 415–447, 1992. 96

[Mallat 1989] S. Mallat. *Multiresolution Approximations and Wavelet Orthonormal Bases of L2(R).* Transactions of the American Mathematical Society, vol. 315, no. 1, pages 69–87, 1989. 68

[Mansour 1978] N.N. Mansour, J.H. Ferziger et W.C. Reynolds. *Large-eddy simulation of a turbulent mixing layer.* Rapport technique, Report TF-11, Thermosciences Div., Dept. of Mech. Eng., Standford University, 1978. 32

[Mehran 2009] R. Mehran, A. Oyama et M. Shah. *Abnormal crowd behavior detection using social force model.* In IEEE Conference on Computer Vision and Pattern Recognition, volume 0, pages 935–942, Los Alamitos, CA, USA, 2009. 54

[Mémin 1998] E. Mémin et P. Pérez. *Dense estimation and object-based segmentation of the optical flow with robust techniques.* IEEE transactions on image processing : a publication of the IEEE Signal Processing Society, vol. 7, no. 5, pages 703–19, Janvier 1998. 11, 14, 42

[Menzel 2001] W.P. Menzel. *Cloud Tracking with Satellite Imagery : From the Pioneering Work of Ted Fujita to the Present.* Bulletin of the American Meteorological Society, vol. 82, no. 1, pages 33–48, 2001. 15

[Metropolis 1953] N. Metropolis, A.W. Rosenbluth, M.N. Rosenbluth, A.H. Teller et E. Teller. *Equation of State Calculations by Fast Computing Machines.* The Journal of Chemical Physics, vol. 21, no. 6, pages 1087–1092, 1953. 96

[Michelet 2007] F. Michelet, J.-P. Da Costa, O. Lavialle, Y. Berthoumieu, P. Baylou et C. Germain. *Estimating Local Multiple Orientations.* Signal Processing, vol. 87, pages 1655–1669, 2007. 77

[Mikic 1998] I. Mikic, S. Krucinski et J.D. Thomas. *Segmentation and tracking in echocardiographic sequences : active contours guided by optical flow estimates.* IEEE transactions on medical imaging, vol. 17, no. 2, pages 274–84, Avril 1998. 11

[Mitiche 1996] A. Mitiche et P. Bouthemy. *Computation of image motion : a synopsis of current problems and methods.* Int. Journ. of Comp. Vis., vol. 19, no. 1, pages 29–55, 1996. 11

[Monasse 2000] P. Monasse et F. Guichard. *Fast computation of a contrast-invariant image representation.* IEEE Transactions on Image Processing, vol. 9, no. 5, pages 860–872, 2000. 81

[Nagel 1990] H.H. Nagel. *Extending The Oriented Smoothness Constraint Into The Temporal Domain and The Estimation Of Derivatives Of Optical Flow.* In Proc. First European Conference On Comput. Vis., pages 139–148, Antibes, France, 1990. Springer. 14, 29

[Nesi 1993] P. Nesi. *Variational Approach To Optical Flow Estimation Managing Discontinuities.* Image and Vision Computing, vol. 11, no. 7, pages 419–439, 1993. 14

[Oksendal 1998] B. Oksendal. Stochastic differential equations. Spinger-Verlag, 1998. 21, 33, 47

[Osher 1988] S. Osher et J.A. Sethian. *Fronts propagating with curvature-dependent speed : algorithms based on Hamilton–Jacobi formulations.* J. Comput. Phys., vol. 79, no. 1, pages 12–49, 1988. 46

[Otsu 1979] N. Otsu. *A threshold selection method from gray-level histograms.* IEEE Transactions on Systems, Man and Cybernetics, vol. 9, no. 1, pages 62—-66, 1979. 86

[Pal 1993] N.R. Pal et S.K. Pal. *A review on image segmentation techniques.* Pattern Recognition, vol. 26, no. 9, pages 1277–1294, 1993. 75

[Papadakis 2007a] N. Papadakis. *Assimilation de données images : application au suivi de courbes et de champs de vecteurs.* PhD thesis, University Rennes 1, 2007. 30

[Papadakis 2007b] N. Papadakis, T. Corpetti et E. Mémin. *Dynamically consistent optical flow estimation.* In IEEE International Conference on Computer Vision, ICCV'07, pages 1–7. Ieee, Octobre 2007. 35, 42

[Papadakis 2008] N. Papadakis et E. Memin. *Variational Assimilation of Fluid Motion from Image Sequence.* SIAM Journal on Imaging Sciences, vol. 1, no. 4, page 343, 2008. 11, 34

[Papenberg 2006] N. Papenberg, A. Bruhn, T. Brox, S. Didas et J. Weickert. *Highly Accurate Optic Flow Computation with Theoretically Justified Warping.* Int. J. Comput. Vision, vol. 67, no. 2, pages 141–158, 2006. 14

[Papin 2000] C. Papin, P. Bouthemy, E. Mémin et G. Rochard. *Tracking and Characterization of Highly Deformable Cloud Structures.* In D Vernon, editeur, Proc. Europ. Conf. Comput. Vis., volume II, pages 428–442, Dublin, Irland, 2000. Springer notes in computer science 1843. 46

[Pecot 2008] T. Pecot et C. Kervrann. *Patch-based markov models for change detection in image sequence analysis.* In Workshop on Local and Non-local Approximation in Image Processing, pages 1–6, Lausanne,Switzerland, 2008. 86

[Pecot 2009] T. Pecot, A. Chessel, S. Bardin, J. Salamero, P. Bouthemy et C. Kervrann. *Conditional Random Fields for object and background estimation in fluorescence video-microscopy.* In Proc. IEEE Int. Symp. on Biomedical Imaging : from nano to macro (ISBI'09), volume 2, pages 734—-737, 2009. 86

[Radke 2005] R.J. Radke, S. Andra, O. Al-Kofahi et B. Roysam. *Image change detection algorithms : a systematic survey.* Image Processing,, vol. 14, no. 3, pages 294–307, Mars 2005. 85, 86

[Raffel 2007] M. Raffel, C.E. Willert et S. Wereley. Particle image velocimetry : a practical guide, volume 36. Springer Verlag, 2007. 15

[Ridd 1998] M.K. Ridd et J. Liu. *A comparison of four algorithms for change detection in an urban environment.* Remote Sensing of Environment, vol. 63, pages 95–100, 1998. 86

[Rosin 2002] P.L. Rosin. *Thresholding for Change Detection.* Computer Vision and Image Understanding, vol. 86, no. 2, pages 79–95, 2002. 86

[Ruhnau 2004] P. Ruhnau, T. Kohlberger, C. Schnoerr et H. Nobach. *Variational optical flow estimation for particle image velocimetry.* Experiments in Fluids, vol. 38, no. 1, pages 21–32, 2004. 11

[Ruhnau 2007] P. Ruhnau et C. Schnoerr. *Optical Stokes Flow Estimation : An Imaging-Based Control Approach.* Exp.in Fluids, vol. 42, no. 1, pages 61–78, 2007. 16, 29

[Saint-Venant (De) 1871] A.J.C. Saint-Venant (De). *Théorie du mouvement non-permanent des eaux, avec application aux crues des rivières et à l'introduction des marées dans leur lit.* C. R. Acad. Sc. Paris, vol. 73, pages 147–154, 1871. 37

[Sakaino 2008] H. Sakaino. *Fluid Motion Estimation Method based on Physical Properties of Waves.* In Proceedings of the 21st IEEE Conference on Computer Vision and Pattern Recognition CVPR 08, 2008. 11

[Schiewe 2001] J. Schiewe, L. Tufte et M. Ehlers. *Potential and problems of multi-scale segmentation methods in remote sensing.* GeoBIT/GIS, vol. 6, pages 34–39, 2001. 76

[Schmetz 1987] J. Schmetz et M. Nuret. *Automatic tracking of high-level clouds in Meteosat IR images with a radiance windowing technique.* ESA J, vol. 11, pages 275–286, 1987. 15

[Schunck 1986] B.G. Schunck. *The Image Flow Constraint Equation.* Comput. Vision, Graphics, Image Proc., vol. 35, pages 20–46, 1986. 14

[Sethian 1999] J.A. Sethian. Level Set Methods and Fast Marching Methods : Evolving Interfaces in Computational Geometry, Fluid Mechanics, Computer Vision and Materials Science. Cambridge University Press, 1999. 46

[Shafer 1976] G.A. Shafer. Mathematical Theory of Evidence. Princeton University Press, 1976. 72

[Smith 1971] E.A. Smith et D.R. Phillips. *Automated cloud tracking using precisely aligned digital ATS pictures.* IEEE Transactions on Computers, vol. C-21, pages 715–729, 1971. 15

[Sonka 1993] M. Sonka, V. Hlavac et R. Boyle. Image Processing, Analysis, and Machine Vision. CL-Engineering, 1993. 76

[Sugii 2000] Y. Sugii, S. Nishio, T. Okuno et K. Okamoto. *A highly accurate iterative PIV technique using a gradient method.* Measurement Science and Technology, vol. 11, no. 12, page 1666, 2000. 16

[Sun 2010a] D. Sun, S. Roth et M.J. Black. *Secrets of optical flow estimation and their principles.* In Proc. 2010 IEEE Computer Vision and Pattern Recognition, pages 2432 – 2439, 2010. 14

[Sun 2010b] D. Sun, E.B. Sudderth et M.J. Black. *Layered Image Motion with Explicit Occlusions , Temporal Consistency , and Depth Ordering.* ReCALL, pages 1–9, 2010. 14

[Suter 1994] D. Suter. *Motion Estimation and Vector Splines*. In Proc. Conf. Comp. Vision Pattern Rec., pages 939–942, Seattle, USA, 1994. 16, 18

[Talagrand 1987] O. Talagrand et P. Courtier. *Variational assimilation of meteorological observations with the adjoint vorticity equation. {I} : Theory*. J. of Roy. Meteo. soc., vol. 113, pages 1311–1328, 1987. 30, 34

[Talagrand 1997] O. Talagrand. *Assimilation of observations, an introduction*. J. Meteor. Soc. Jap., vol. 75, pages 191–209, 1997. 30

[Taylor 1932] G.I. Taylor. *The transport of vorticity and heat through fluids in turbulent motion*. In Proc London Math Soc. Ser A, pages 151–421, 1932. 32

[Tetriak 1984] O. Tetriak et L. Pastor. *Velocity estimation from image sequences with second order differential operators*. In Int. Conf. on Pattern Recogition, Montreal, 1984. 14

[Thomas 2009] C. Thomas, T. Corpetti et E. Mémin. *Data Assimilation for Convective Cells Tracking in {MSG} images*. In IEEE Int. Geoscience and Remote Sensing Symp., IGARSS '09, complete references to appear, volume 2, pages 813–816, Cape Town, South Africa, 2009. 47, 48

[Thomas 2010] C. Thomas, T. Corpetti et E. Mémin. *Data Assimilation for Convective Cells Tracking on Meteorological Image Sequences*. IEEE Transactions on Geosciences and Remote Sensing, vol. 48, no. 8, pages 3162–3177, 2010. 47, 48

[Tison 2007] C. Tison, F. Tupin et H. Maitre. *A Fusion Scheme for Joint Retrieval of Urban Height Map and Classification From High-Resolution Interferometric SAR Images*. Geoscience and Remote Sensing, IEEE Transactions on, vol. 45, no. 2, pages 496 –505, 2007. 80

[Tropea 2007] C. Tropea, A.L. Yarin et J.F. Foss. Springer Handbook of Experimental Fluid Mechanics, volume 46. Springer Verlag, 2007. 15

[Varanasi 1989] M.K. Varanasi et B. Aazhang. *Parametric generalized Gaussian density estimation*. Journal of the Acoustical Society of America, vol. 86, pages 1404–1415, 1989. 69

[Vidard 2000] P.A. Vidard, E. Blayo, F.-X. Le Dimet et A. Piacentini. *4D Variational Data Analysis with Imperfect Model*. Flow, Turbulence and Combustion, vol. 65, no. 3-4, pages 489–504, 2000. 30

[Weber 1995] J. Weber et J. Malik. *Robust Computation of Optical Flow in a Multi-Scale Differential Framework*. Int. J. Comput. Vis., vol. 14, no. 1, 1995. 14

[Wedel 2008] A. Wedel, T. Pock, J. Braun, U. Franke et D. Cremers. *Duality TV-L1 Flow with Fundamental Matrix Prior*. In Image Vision and Computing, Auckland, New Zealand, 2008. 14

[Weickert 2001a] J. Weickert et C. Schnoerr. *A Theoretical Framework for Convex Regularizers in PDE-Based Computation of Image Motion*. International Journal of Computer Vision, vol. 45, no. 3, pages 245 – 264, 2001. 14

[Weickert 2001b] J. Weickert et C. Schnörr. *Variational optic-flow computation with a spatio-temporal smoothness constraint*. J. Math. Imaging and Vision, vol. 14, no. 3, pages 245–255, 2001. 29

[Wiegand 2003] T. Wiegand, G.J. Sullivan, G. Bjontegaard et A. Luthra. *Overview of the H.264/AVC video coding standard*. IEEE Transactions on Circuits and Systems for Video Technology, vol. 13, no. 7, pages 560–576, 2003. 14

[Wu 1995] Q.X. Wu. *A Correlation-Relaxation-Labeling Framework for Computing Optical Flow - Template Matching from a New Perspective.* IEEE Transactions on Pattern Analysis and Machine Intelligence, vol. 17, no. 8, pages 843–853, 1995. 15

[Wu 1997] Q.X. Wu, S.J. McNeill et D. Pairman. *Correlation and relaxation labelling : an experimental investigation on fast algorithms.* International Journal of Remote Sensing, vol. 18, no. 3, pages 651–662, 1997. 15

[Xu 2008] L. Xu, J.N. Chen et J.Y. Jia. *A Segmentation Based Variational Model for Accurate Optical Flow Estimation.* In Eur. Conf. Comp. Vis., pages I : 671–684, 2008. 14

[Yacoob 1996] Y. Yacoob et L.S. David. *Recognizing human facial expressions from long image sequences using optical flow.* Pattern Analysis and Machine Intelligence, IEEE Transactions on, vol. 18, no. 6, pages 636–642, 1996. 11

[Yahia 1998] H. Yahia et J.P. Berroir. *Segmentation of deformable templates with level sets characterized by particle systems.* In Proc. Int. Conf. Pattern Recognition, pages 1421–1423, Brisbane, 1998. 46

[Yuan 2007] J. Yuan, C. Schnoerr et E. Mémin. *Discrete orthogonal decomposition and variational fluid flow estimation.* Journ. of Mathematical Imaging and Vision, vol. 28, no. 1, pages 67–80, 2007. 16, 25, 26, 27, 54

Abstract

This PhD Habilitation is devoted to the analysis of time series of Low Spatial Resolution (LSR) and Very High Spatial Resolution (VHSR) remote sensing images. Events of interest are related to meteorology and oceanography (for LSR data) and to agriculture and urban applications (for VHSR data).

The rate of acquisition of satellite data is inversely proportional to their spatial resolution. Therefore with LSR images, the cadence is very high (for instance one image every $15min$ with MSG –Meteosat Second Generation) and enables an analysis of the turbulent atmospheric flows observed through the motion of the clouds, the oceanic circulation, ... Related computer vision problems concern motion estimation, curve tracking and missing data interpolation. On the other hand, with VHSR images, the time between two data can be from several weeks to several months. The related studies are rather concerned with the definition of advanced change detection techniques to highlight the main structural changes between images.

From a methodological point of view, we are based on the introduction of physical knowledge in computer vision tools in order to define specific techniques for the analysis of structures in LSR data. A large part is devoted to variational assimilation approaches. As for VHSR images, we propose original descriptors to characterize the textured areas and applied them for numerous problems (segmentation, classification, orientation estimation, textured front detection). Finally, a chapter is especially devoted to the change detection issue where we introduce techniques for binary and multi-label change detection.

Resumé

Ce document d'habilitation est consacré à l'étude de séries temporelles d'images de télédétection à basse (LSR) et à très haute résolution spatiale (VHSR). Les phénomènes étudiés concernent la météorologie et l'océanographie (données LSR) et l'agriculture et le milieu urbain (données VHSR).

La fréquence d'acquisition des données satellites est inversement proportionnelle à la résolution spatiale. Ainsi, pour des données LSR, la cadence d'acquisition est élevée (une images pour $15min$ avec le satellite MSG –Météosat Seconde Génération) et cela autorise l'étude des mouvement atmosphériques turbulents observés à travers le mouvement des nuages, la circulation océanique, ... Les problèmes d'analyse d'images associés concernent l'estimation du mouvement, le suivi de courbe ou encore l'interpolation de données manquantes. En ce qui concerne les données VHSR, la période séparant deux images peut varier de quelques semaines à quelques mois. Les études associées sont alors dédiées à la détection de changements structurels entre deux images.

Du point de vue méthodologique, l'analyse de données LSR est principalement réalisée en introduisant des connaissances physiques a priori dans les outils classiques d'analyse d'images. Une part importante est dédiée à l'utilisation de techniques d'assimilation variationnelle de données. Pour l'analyse de données VHSR, nous proposons des descripteurs spécifiques permettant de caractériser les motifs texturés que l'on a à manipuler. Ces descripteurs sont ensuite utilisés pour résoudre différents problèmes d'analyse de données VHSR tels que la segmentation, la classification, la détection de fronts texturés ou encore l'estimation de l'orientation. Enfin, un chapitre est consacré à la détection de changements où nous proposons des techniques pour le détection binaire et multi-labels.